

Anionic substitution in perovskite-type oxides

Dissertation
zur Erlangung des Doktorgrades
der mathematisch-naturwissenschaftlichen Fakultät
der Universität Augsburg

vorgelegt von

Dmitry Logvinovich

Augsburg, Juli 2008



Solid State Chemistry and Catalysis,
Empa, CH-8600 Dübendorf



Materials Science & Technology

Dedicated to my parents, my sister and Nadja.

Erstgutachter: Prof. Dr. Armin Reller

Zweitgutachter: Priv. Doz. Dr. Anke Weidenkaff

Prof. Dr. Jochen Mannhart

Priv. Doz. Dr. Karl-Heinz Höck

Tag der mündlichen Prüfung: 21.11.2008

Index

Index	1
Abstract	4
Zusammenfassung	6
1. Introduction	8
1.1. Perovskite structure	8
1.2. Electronic structure and optical properties of perovskite-type oxides.	11
1.3. Photocatalytic properties of oxides.....	14
1.4. Anionic substitution.....	15
1.5. Synthesis of oxynitrides	17
1.6. Thermal stability of perovskite-type oxynitrides.	23
1.7. Optical properties of perovskite-type oxynitrides. Pigments.	25
1.8. Photocatalytic properties of oxynitrides.....	27
1.9. Anionic ordering.....	29
1.10. Mixed-valent oxynitride-perovskites.....	32
1.11. Scope of the present work	33
2. Experimental techniques	36
2.1. Synthesis of oxide precursors.....	36
2.1.1. Ceramic method.....	36
2.1.2. Soft chemistry synthesis.....	36
2.1.3. Precipitation from aqueous solution.....	39
2.1.4. Reduction of $AMoO_4$ to $AMoO_3$	39
2.2. Thermal ammonolysis	40
2.3. Structural and microstructural characterization by diffraction techniques.....	42
2.3.1. X-ray diffraction	42
2.3.2. Neutron diffraction	43

2.3.3. Structural and microstructural analysis from powder diffraction data by using the Rietveld method.....	43
2.3.4. Transmission electron microscopy	49
2.4. Composition and microstructure studies	49
2.4.1. Hotgas-extraction	49
2.4.2. Thermogravimetric (TGA) and Differential Thermal (DTA) analysis	50
2.4.3. Neutron diffraction	52
2.4.4. Scanning electron microscopy and energy dispersive analysis.....	53
2.4.5. Measurements of the specific surface area	53
2.5. Photocatalytic activity	55
2.5.1. Platinum impregnation	55
2.5.2. Photocatalytic water decomposition.....	55
2.6. Spectroscopic characterization	56
2.6.1. UV-Vis diffuse reflectance spectroscopy.....	56
2.6.2. Raman and infrared spectroscopy.....	57
2.6.3. Extended X-ray absorption spectroscopy	58
2.7. Physical properties.....	59
2.7.1. Magnetic susceptibility.....	59
2.7.2. Electronic transport measurements.....	59
3. $\text{Ca}_{1-x}\text{La}_x\text{TiO}_{3-x}\text{N}_x$ ($x = 0 - 0.7$) oxynitrides	61
3.1. Synthesis and thermal stability	61
3.2. Structure	67
3.3. Influence of cooling on the bulk anionic and surface composition of LaTiO_2N	73
3.4. Optical properties	78
3.5. Conclusions	80
4. LaNbON_2	83
4.1. Synthesis and stability	83
4.2. Room and low T crystal structure	87
4.3. Optical properties and photocatalytic activity	92
4.4. Conclusions	95

5. Mo-containing oxynitrides	96
5.1. SrMoO _{3-x} N _x (x > 1)	96
5.1.1. Synthesis and stability	96
5.1.2. Structure and microstructure	98
5.1.3. High temperature physical properties.....	104
5.1.4. Low temperature physical properties	107
5.1.5. Conclusions	113
5.2. CaMo(O,N) ₃ and BaMo(O,N) ₃ . Phase formation, structural and microstructural characterization of novel oxynitride-perovskites.	115
5.2.1. Synthesis of starting oxides	115
5.2.2. General procedure for the ammonolysis of molybdates.....	117
5.2.3. Thermal ammonolysis study of AMoO ₄ (A = Ca ²⁺ , Ba ²⁺)	117
5.2.4. Thermal ammonolysis study of AMoO ₃ (A = Ca ²⁺ , Ba ²⁺)	120
5.2.5. Discussion of the thermal ammonolysis results	123
5.2.6. Crystal structures of CaMoO ₃ , CaMo(O,N) ₃ and BaMo(O,N) ₃	126
5.2.7. Conclusions	135
Summary	137
List of publications.....	139
References	142
Acknowledgements	148
Curriculum vitae.....	150

Abstract

In this thesis a number of novel perovskite-type oxynitrides ($\text{La}_x\text{Ca}_{1-x}\text{TiO}_{3-x}\text{N}_x$ ($x = 0 - 0.7$), LaNbON_2 , $\text{SrMo}(\text{O},\text{N})_3$, $\text{CaMo}(\text{O},\text{N})_3$, $\text{BaMo}(\text{O},\text{N})_3$) were synthesized and their structure, microstructure, physical properties and thermal stability were investigated. Simultaneous substitution of Ca^{2+} with La^{3+} and O^{2-} with N^{3-} in CaTiO_3 leads to the oxynitride solid solutions of general formula $\text{La}_x\text{Ca}_{1-x}\text{TiO}_{3-x}\text{N}_x$. All these materials crystallize in a distorted perovskite unit cell. Their optical band gap varies linearly with Ca/N-content.

The crystal structure, thermal stability, optical and photocatalytic properties of perovskite type oxynitride LaNbON_2 were investigated. The material crystallizes in the distorted GdFeO_3 structure type (space group: *Pnma*). It shows the smallest optical band gap among the early transition metal oxynitride-perovskites and high photocatalytic activity for hydrogen reforming from methanol among the reported oxynitride-perovskites.

A number of novel conductive oxynitrides were synthesized. Oxynitrides of the general composition $\text{SrMoO}_{3-x}\text{N}_x$ ($x > 1$) were synthesized by thermal ammonolysis of crystalline SrMoO_4 . According to the neutron and x-ray diffraction experiments the materials crystallize in the cubic perovskite structure (space group $\overline{\text{Pm } 3m}$). X-ray absorption spectroscopy shows evidence of local distortions of the $\text{Mo}(\text{O},\text{N})_6$ octahedra. The oxidation states of Mo determined by x-ray absorption near edge structure spectroscopy are lower than calculated from the oxygen/nitrogen (O/N) content. The disagreement arises from the higher covalence of the Mo-N bonding when compared to the Mo-O bonding (“chemical shift”). The electrical transport properties of $\text{SrMoO}_{3-x}\text{N}_x$ ($x > 1$) are different from SrMoO_3 . It was found that the conductivity of the samples decreases with the increase of nitrogen content. The Seebeck coefficient values are up to 3 times higher than those of SrMoO_3 .

Reactions of AMoO_4 and AMoO_3 ($A = \text{Ca}^{2+}$, Ba^{2+}) with ammonia were investigated at $T = 873 \text{ K} - 1123 \text{ K}$ with the particular intention to synthesize novel oxynitride-perovskites

of the composition $AMo(O,N)_3$ and to study their crystal structure. $CaMo(O,N)_3$ and $BaMo(O,N)_3$ were prepared by thermal ammonolysis of the corresponding $CaMoO_3$ and $BaMoO_3$ precursors at $T = 898$ K and $T = 998$ K, respectively. The structural parameters of the oxynitrides were obtained from Rietveld refinements of x-ray and neutron powder diffraction data. $CaMo(O,N)_3$ crystallizes in the distorted $GdFeO_3$ structure type with orthorhombic space group $Pbnm$ and $a = 5.5029(1)$ Å, $b = 5.5546(1)$ Å, $c = 7.8248(1)$ Å as determined by x-ray powder diffraction. Its O/N content refined from the neutron diffraction data corresponds to the composition $CaMoO_{1.7(1)}N_{1.3(1)}$. $BaMo(O,N)_3$ crystallizes in the cubic perovskite structure with space group $Pm\bar{3}m$ and $a = 4.0657(1)$ Å as determined by x-ray powder diffraction. Transmission electron microscopy reveals a complex microstructure for both $CaMoO_3$ and $CaMoO_{1.7(1)}N_{1.3(1)}$ represented by twin-domains of different orientation.

Zusammenfassung

In der vorliegenden Arbeit wurden eine Reihe neuer, perowskit-artiger Oxidnitride ($\text{La}_x\text{Ca}_{1-x}\text{TiO}_{3-x}\text{N}_x$ ($x = 0 - 0.7$), LaNbON_2 , $\text{SrMo}(\text{O},\text{N})_3$, $\text{CaMo}(\text{O},\text{N})_3$ und $\text{BaMo}(\text{O},\text{N})_3$) hergestellt und diese auf ihre Struktur, Mikrostruktur, physikalischen Eigenschaften und ihre thermische Stabilität hin untersucht.

Die gleichzeitige Substitution von Ca^{2+} mit La^{3+} und O^{2-} mit N^{3-} in CaTiO_3 führt zu Oxidnitriden der allgemeinen Form $\text{La}_x\text{Ca}_{1-x}\text{TiO}_{3-x}\text{N}_x$. Diese Materialien kristallisieren in einer verzerrten Perowskit Elementarzelle wobei sich ihre optische Bandlücke linear mit dem Ca/N-Gehalt ändert.

Es wurde weiterhin die Kristallstruktur, thermische Stabilität sowie die optischen und photokatalytischen Eigenschaften der perowskit-artigen Oxidnitride vom Typ LaNbON_2 untersucht. Diese Proben kristallisieren in einem verzerrten GdFeO_3 Strukturtyp (Raumgruppe *Pnma*) und zeigten von den genannten Oxidnitrid-Perowskiten die kleinste optische Bandlücke bei gleichzeitig beachtlicher photokatalytischer Aktivität, während der Wasserstoff Reformierung aus Methanol.

Des Weiteren wurde eine Reihe neuer leitfähiger Oxidnitride der allgemeinen Form $\text{SrMoO}_{3-x}\text{N}_x$ ($x > 1$) durch thermische Ammonolyse von kristallinem SrMoO_4 hergestellt. Neutronen- und röntgendiffraktometrische Untersuchungen belegen eine kubische Perowskitstruktur (Raumgruppe *Pm* $\bar{3}m$). Mittels Röntgenabsorption-Spektroskopie (XAS) konnten Hinweise auf lokale Verzerrung des $\text{Mo}(\text{O},\text{N})_6$ -Okteaders gefunden werden. Die durch XANES ermittelte Oxidationszustände von Mo waren niedriger als die aus dem Sauerstoff/Stickstoff (O/N)-Gehalt berechneten Werte. Dieser Unterschied kann durch die höhere Kovalenz der Mo-N Bindung im Vergleich zur Mo-O Bindung ("chemische Verschiebung") beschrieben werden. Die elektrischen Transporteigenschaften von $\text{SrMoO}_{3-x}\text{N}_x$ ($x > 1$) unterscheiden sich stark von SrMoO_3 . Es konnte gezeigt werden, dass die Leitfähigkeit der Proben mit dem Anstieg des Stickstoff-Gehaltes abnahm. Die Werte für den Seebeck-Koeffizienten waren bis zu dreimal höher als die von SrMoO_3 .

Es wurden Reaktionen von $AMoO_4$ und $AMoO_3$ ($A = Ca^{2+}, Ba^{2+}$) mit Ammoniak im Temperaturbereich $T = 873\text{ K} - 1123\text{ K}$ untersucht, mit der Absicht, neue Oxidnitrid-Perowskite der Zusammensetzung $AMo(O,N)_3$ zu synthetisieren und deren Kristallstruktur zu untersuchen. Weiterhin wurde $CaMo(O,N)_3$ und $BaMo(O,N)_3$ durch thermische Ammonolyse aus $CaMoO_3$ und $BaMoO_3$ bei Temperaturen von $T = 898\text{ K}$ und $T = 998\text{ K}$ hergestellt.

Die Kristallstrukturen der Oxidnitride wurden durch Rietveld-Verfeinerungen der Röntgen- und Neutronen-Pulverdiffraktometrie Datensätze erhalten. $CaMo(O,N)_3$ kristallisiert in verzerrter $GdFeO_3$ -Struktur mit orthorhombischer Raumgruppe $Pbnm$ und $a = 5.5029(1)\text{ \AA}$, $b = 5.5546(1)\text{ \AA}$, $c = 7.8248(1)\text{ \AA}$, wie bereits durch Röntgen-Pulverdiffraktometrie gezeigt werden konnte. Der durch neutronendiffraktometrische Messungen bestimmte O/N-Gehalt entspricht der Zusammensetzung $CaMoO_{1.7(1)}N_{1.3(1)}$. $BaMo(O,N)_3$ kristallisiert in kubischer Perowskitstruktur mit der Raumgruppe $Pm\bar{3}m$ und $a = 4.0657(1)\text{ \AA}$ (bestimmt mittels Röntgenpulverdiffraktometrie). TEM-Untersuchungen zeigten sowohl für $CaMoO_3$ und $CaMoO_{1.7(1)}N_{1.3(1)}$ eine komplexe Mikrostruktur die sich durch Zwillingsdomänen verschiedener Orientierung auszeichnete.

1. Introduction

1.1. Perovskite structure

The original mineral perovskite (CaTiO_3) was discovered in the Ural mountains of Russia by the German mineralogist Gustav Rose in 1834. Its structure is represented by the cage of corner-shared TiO_6 -octahedra with Ca^{2+} -ions filling the formed interstitials. Although, the crystal structure of the mineral is orthorhombic (space group, S.G. $Pnma$), there are plenty of other materials (ABX_3), belonging to the same structure type but showing different symmetry, which (as it will be discussed below) arises mainly from the octahedral tilting and B-site cation displacement.

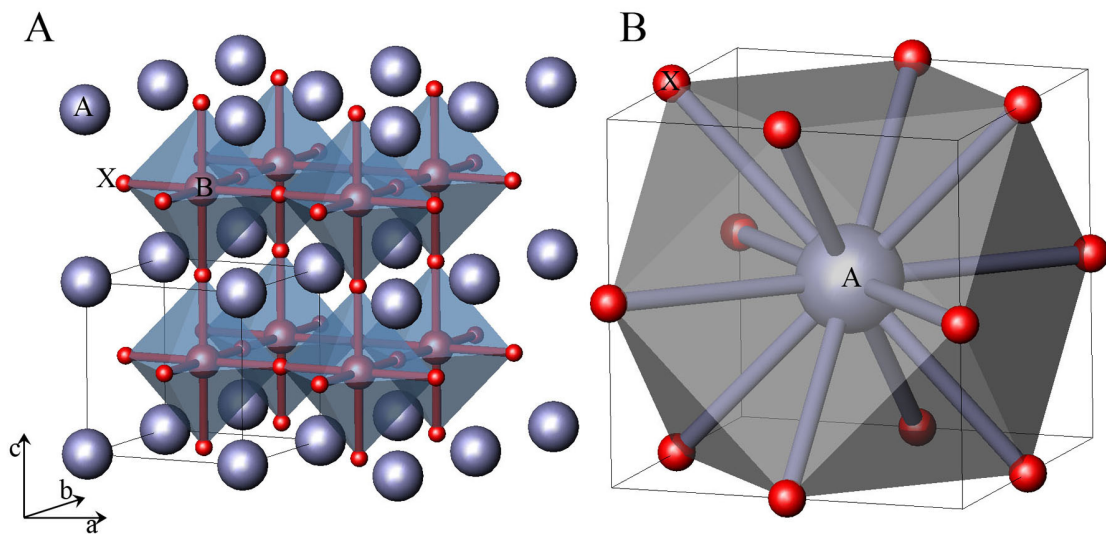


Figure 1.1. A. Crystal structure of cubic perovskite of general formula ABX_3 B. Twelve-fold coordination of the A -site cation.

The ideal perovskite is formed by a cubic ABCABC stacking of close-packed AX_3 planes with B -cations occupying the octahedral interstices coordinated by six X -anions. The A - and the X -site ions are correspondingly 12- and 6- fold coordinated (Fig. 1.1) [1]. For

perovskites the measure of the mismatch between the average equilibrium $A-X$ and $B-X$ bond lengths is expressed by the so-called tolerance factor (t) [2]:

$$t = \frac{\langle A-X \rangle}{\sqrt{2}\langle B-X \rangle} \quad (1.1)$$

where

$\langle A-X \rangle$ is the average equilibrium $A-X$ bond,

$\langle B-X \rangle$ is the average equilibrium $B-X$ bond.

The value of t is equal to 1 for the ideal cubic perovskite structure and it is simply derived from the equation relating length of the cube's face diagonal with that of the edge of the cube shown in Figure 1.1. For most perovskites t deviates from one.

When $t < 1$ (the B -site cation is large) the $B-X$ bonds are under compression, whereas the $A-X$ bonds are under tension. The resulting stress is partly revealed by a cooperative rotation of the BX_6 – octahedra (angle $B-X-B < 180^\circ$). Hence, the crystallographic symmetry is lowered. The most common types of the octahedra rotations are [3]:

1. Around a cubic [001] axis (S.G., $I4/mcm$ if rotations of successive (001) planes are out of phase (Fig. 1.2A); S.G. $P4/mbm$ if rotations of successive (001) planes are in-phase);
2. Around a cubic [111] diagonal (S.G. $R\bar{3}c$ if rotations of successive (111) planes are out of phase; S.G. $Im\bar{3}$ if rotations of successive (001) planes are in-phase);
3. Around a cubic [110] axis (S.G. $Pnma$ or its nonstandard setting $Pbnm$).

The most recent study of Howard and Stokes based on group-theoretical analysis yields in 15 possible space groups, which describe different types of octahedra rotations in simple perovskites [4].

When $t > 1$ (the B -site cation is small) the $B-X$ bonds are under tension, whereas the $A-X$ bonds are under compression. The resulting stress is partly revealed either by the displacement of the B -site cation within the BX_6 – octahedra or the formation of the hexagonal ABABAB stacking sequence of AX_6 planes, where the BX_6 octahedra share

faces, forming columns, and *A*-site cations occupy the place between the columns (Fig. 1.2B) [1-3].

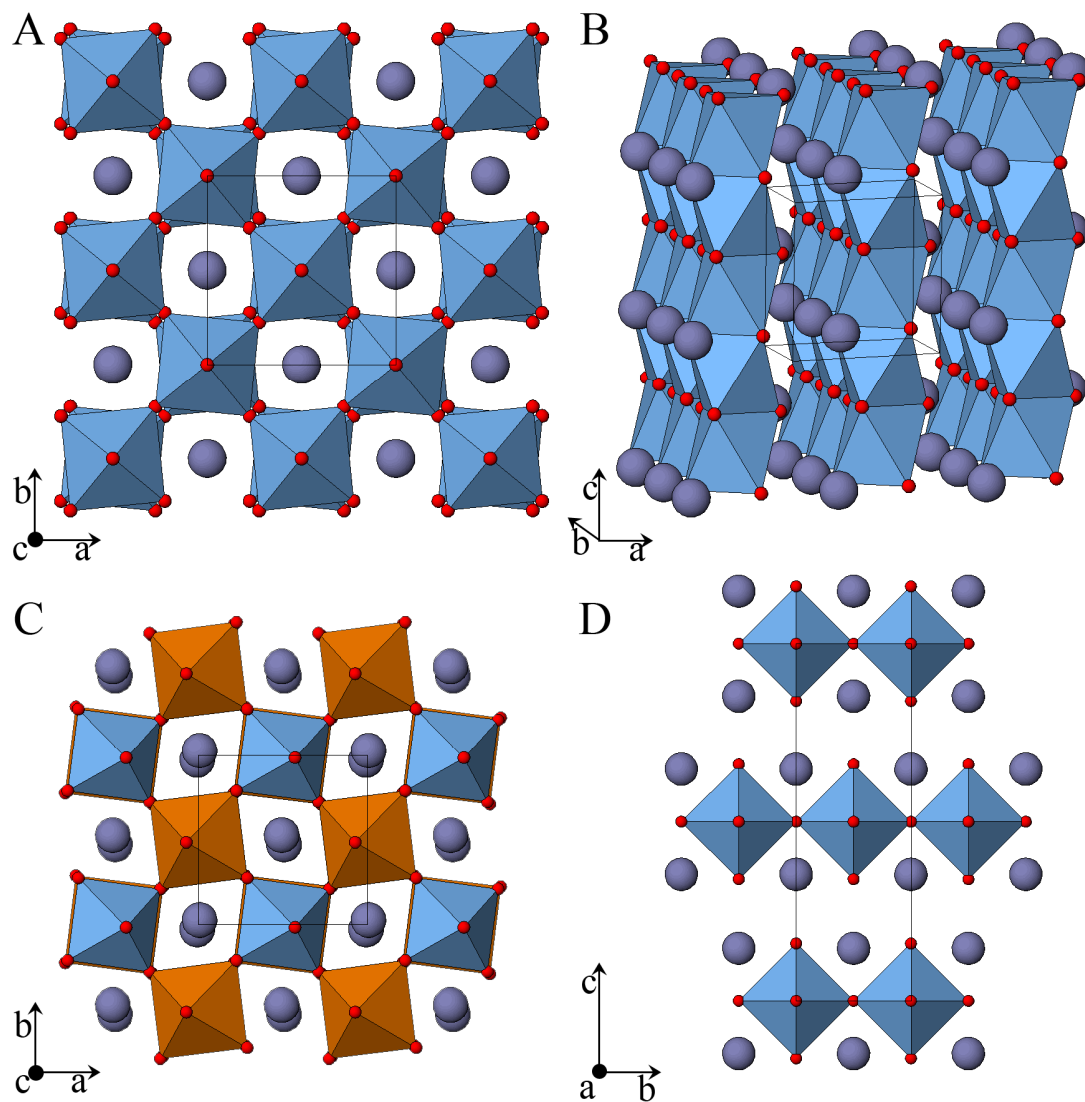


Figure 1.2. A. An example of the tetragonally distorted simple perovskite structure (low temperature modification of SrTiO_3 , S.G. $I4/mcm$). B. An example of the hexagonal perovskite structure (2H-BaCoO_3 , S.G. $P6_3/mmc$). C. An example of double perovskite ($\text{La}_2\text{TiMgO}_6$, S.G. $P2_1/n$). D. An example of the intergrowth perovskite-related structure (La_2CoO_4 , S.G. $I4/mmm$)

Moreover, cation ordering leading to double perovskites (Fig. 1.2C) can occur on the *A*- or the *B*-site. Conditions for the cationic ordering are charge difference (typically, more than $2e$) and/or size and electronegativity difference between two ions located in the same sublattice [1].

Beside simple and double perovskites a number of intergrowth perovskite-related structures can be formed. One of the most common intergrowth is formed by the insertion of the additional *AX* (001) plane structure, which leads to the formation of a rock-salt layer A_2X_2 . The members of the formed Ruddlesden-Popper family ($AX(ABX_3)_n$ with $t < 1$) contain an ordered arrangement of rock-salt and perovskite layers (Fig. 1.2D).

1.2. Electronic structure and optical properties of perovskite-type oxides.

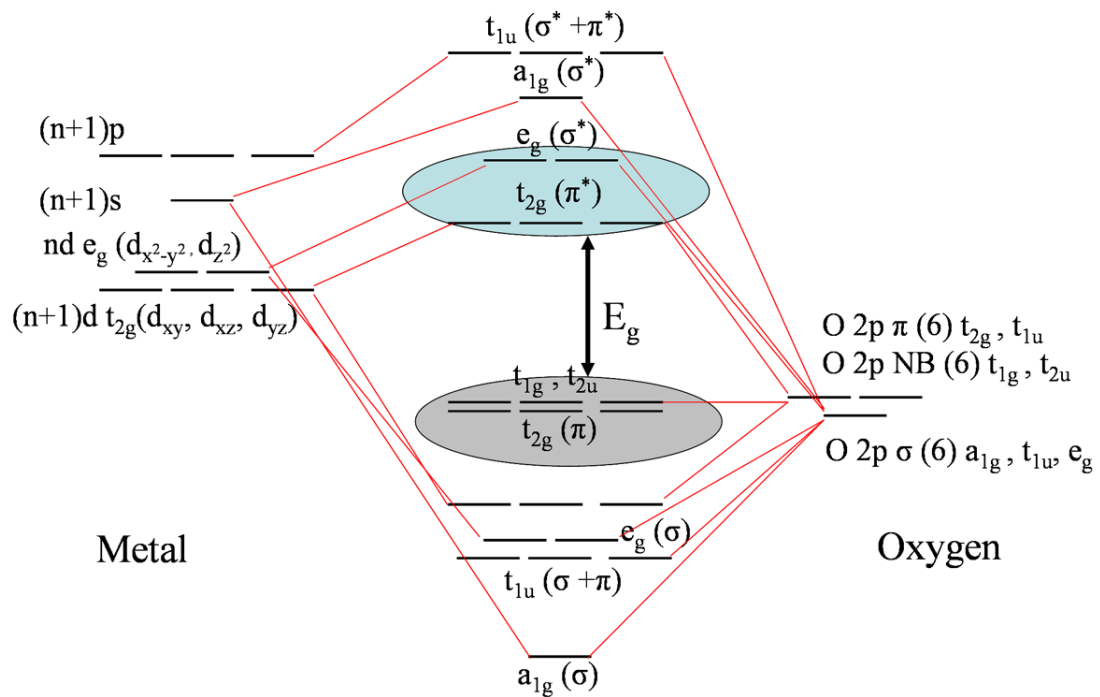


Figure 1.3. Schematic band structure of the perovskite-oxide.

The electronic structure of simple perovskite-type oxides near the Fermi level is formed mainly by mixing of frontier *d*-orbitals of the transition metal and *2p*-orbitals of oxygen.

The top of the valence band is represented mainly by oxygen non-bonding $2p$ -orbitals, whereas the bottom of the conduction band is formed by the anti-bonding $2p$ - nd orbitals (Fig. 1.3).

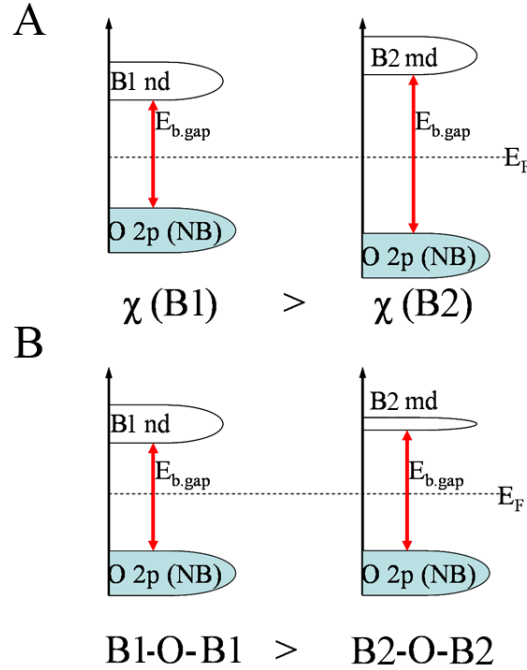


Figure 1.4. Schematic band diagrams showing the influence of A. the electronegativity and B. the B - O - B angle on the band gap of oxides.

Computational and experimental studies using linear muffin tin orbital (LMTO) methods and UV-diffuse reflectance spectroscopy were done to establish the relationships between composition, crystal structure and the electronic structure of oxides containing octahedrally coordinated d^0 transition metal ions (Mo^{6+} , W^{6+} , Nb^{5+} , Ti^{4+} , Ta^{5+}) [5]. It was discovered that for isostructural compounds the band gap increases with the increase of the effective electronegativity of the transition metal ion (Fig. 1.4A). The effective electronegativity of the investigated transition metal ions were found to decrease in the following order: $Mo^{6+} > W^{6+} > Nb^{5+} \sim Ti^{4+} > Ta^{5+}$. Moreover, the band gap is sensitive to changes in the conduction band width, which is maximized for the structures possessing linear B - O - B bonds, such as the cubic perovskite structure. As this bond angle decreases (*e.g.*, *via*

octahedral tilting distortions, e.g. when $t < 1$) the conduction band narrows and the band gap increases (Fig. 1.4B). Decrease in the dimensionality from 3-D (simple perovskite) to 2-D (K_2NiF_4) doesn't alter the band gap significantly, whereas complete isolation of the BO_6 octahedra (double perovskite structure) narrows the conduction band dramatically and leads to a significant increase in the band gap. The inductive effect [6] has a minor influence on the band gap width.

Table 1.1. Crystal structures and optical band gaps of selected oxides

Compound	Structure	Band gap, eV	Reference
TiO_2	Rutile ($P4_2/mnm$)	3.0	[7]
CaTiO_3	Perovskite ($Pnma$)	3.3	[5, 8]
SrTiO_3	Perovskite ($Pm3m$)	3.1	[5]
BaTiO_3	Perovskite ($P4/mmm$)	3.3	[9, 10]
$\text{La}_2\text{Ti}_2\text{O}_7$	(110) layered perovskite	3.9	[11]
Ta_2O_5	-	3.8	[12]
LiTaO_3	Perovskite ($R3c$)	4.7	[13, 14]
NaTaO_3	Perovskite ($Pbnm$)	4	[13, 15]
KTaO_3	Perovskite ($Pm3m$)	3.7	[13]
LaTaO_4	$P2_1/c$	3.9	[16, 17]
$\text{h-Nb}_2\text{O}_5$	$P2/m$	3.13	[18, 19]
LiNbO_3	Perovskite ($R3c$)	3.6	[14, 20]
NaNbO_3	Perovskite ($Pbma$)	3.08	[21, 22]
KNbO_3	Perovskite ($Amm2$)	3.14	[21, 23]
WO_3	$P2_1/n$	2.4	[5, 24]
ZrO_2	Baddeleyite ($P2_1/a$)	5.0-5.7	[25, 26]

The established relations between the electronegativity, crystal structure and electronic structure of d^0 -perovskite-oxides allow a qualitative prediction of optical properties for new perovskite-type oxides, which is very useful for designing materials for photochemical applications. Band gaps of selected d^0 -oxides are collected in Table 1.1. As it can be seen the most of oxides absorb light of the UV- or near-Vis-regions and hence, are colorless.

Normally, the band gap of d^0 -oxides is tuned by the cationic substitution. Typically, to reduce the optical band gap, cations of an oxide are substituted by cations with lower electronegativity. This method allows to obtain materials with the optical band gap as small as 2.4 eV [5]. Since nitrogen has lower electronegativity than oxygen, a partial substitution of oxygen with nitrogen can be used as an alternative approach to tune the optical band gap [27]. As it will be discussed below, such an anionic substitution allows to reduce the optical band gap of d^0 -oxides down to 1.8 eV.

1.3. Photocatalytic properties of oxides.

Photocatalytically active materials should satisfy the following criteria:

1. Stability under operating conditions;
2. Good electron-hole pair capacitance [5];
3. Suitable positions of the conduction and the valence bands to facilitate electron-hole transfer on the adsorbed molecules;
4. Suitable band gap value.

First water oxidation has been carried out over n -type TiO_2 (rutile) irradiated with UV-light ($\lambda < 415$ nm) [7]. The quantum efficiency (QE) of that process (~ 10 %) was further increased (up to ~ 29 %) by using the concept of “photochemical diodes” (n -type TiO_2 which surface is impregnated with a noble metal, like Pt, Au, Pd) for more effective electron-hole separation [28].

Today over 130 different materials, mainly oxides, are known either to catalyze water splitting into H_2 and O_2 , oxidation (to produce O_2) or reduction (to produce H_2) [29].

Perovskite- and perovskite-related oxides containing Ti, Ta, and Nb in d^0 -electronic configuration are among the most effective photocatalysts known nowadays, due to the suitable position of their conduction and/or valence bands and good chemical and photochemical stability.

It has been shown that NiO-modified SrTiO_3 is able to split water vapor stoichiometrically under UV irradiation, while SrTiO_3 alone didn't show any photocatalytic activity [30]. For a large band gap $\text{La}_2\text{Ti}_2\text{O}_7$ (3.8-3.9 eV), which is a member of (110) layered perovskites ($A_mB_mX_{3m+x}$ with $m = 2$), QE of 12 % was reported. Doping this catalyst with BaO and

adding NaOH into the catalyst suspension led to QE = 50 % [31]. Doping of $\text{La}_4\text{CaTi}_5\text{O}_{17}$ (3.8 eV) with NiO led to QE = 20 % under UV light [32].

Tantalates $A\text{TaO}_3$ ($A = \text{Li}^+, \text{Na}^+, \text{K}^+$) with band gaps 3.7-4.7 eV have shown remarkable photocatalytic activity [13]. NaTaO_3 with NiO as a co-catalyst was able to decompose pure water on H_2 and O_2 with QE up to 28 %. Doping it additionally with 2 at % of La led to the highest QE (56 %) over water splitting photocatalysts [33].

Among the niobates NiO co-loaded $\text{Sr}_2\text{Nb}_2\text{O}_7$ (3.9 eV) showed remarkable QE during the overall water splitting (23 %) [32]. Another isostructural niobate $\text{Ca}_2\text{Nb}_2\text{O}_7$ achieves QE of 7 % for the H_2 –production, when co-loaded with NiO [32].

However, the main serious disadvantage of oxide catalysts is their relatively large band gaps activated only by UV-radiation. The sunlight which reaches the earth surface contains only 5 % of UV-radiation. Thus, oxide catalysts are rather ineffective to convert solar energy.

1.4. Anionic substitution.

Nowadays cationic substitution is the most common way to change physical properties of perovskite-oxides. Due to its flexibility, the perovskite structure can adopt a large number of cationic substitutions, which allows fine tuning of the electronic structure, charge carrier concentration and consequently electronic and optical properties of the materials [3, 34]. That is why perovskite and perovskite-related oxides can be found in a number of diverse applications such as superconductors ($\text{Bi}_2\text{Sr}_2\text{Ca}_x\text{Cu}_{x+1}\text{O}_{2x+6}$), capacitors (BaTiO_3), catalysts (LaCoO_3 , LaMnO_3), ionic conductors ($\text{La}(\text{Sr})\text{Ga}(\text{Ni})\text{O}_{3-x}$), sensors ($\text{Zr}_{1-x}\text{Y}_x\text{O}_{2-x/2}$), *etc.* Currently, anionic substitution is considered as a prospective alternative to the cationic substitution to change physical properties of perovskites.

To maintain the perovskite-type structure the suitable candidate for the oxygen substitution should possess similar ionic radius, electronic configuration and electronegativity. Among the elements, which are situated around oxygen in the Periodic Table fluorine and nitrogen have ionic radii, electronegativities and electronic configurations similar to those of oxygen. Currently, most of the known anion-substituted perovskite-type oxides are either oxynitrides or oxyfluorides. Perovskite-related oxychlorides and oxysulfides are rare

mainly due to the significant difference in the ionic radii of O^{2-} (1.40 Å) and those of S^{2-} (1.84 Å) and Cl^{-} (1.81 Å).

Perspectives of the O^{2-} substitution with N^{3-} can be better understood if the differences between these ions are emphasized. They are as follows:

1. Different Pauling's electronegativity (3.50 for O and 3.07 for N)
2. Different formal oxidation state (O^{2-} , N^{3-})
3. Different ionic radii ($r(O^{2-}) = 1.40 \text{ Å}$, $r(N^{3-}) = 1.50 \text{ Å}$ for the coordination number equal to 6) [35, 36].

From the difference in electronegativity follows that bonding in oxynitrides should be more covalent than in oxides. Consequently, smaller band gaps for oxynitrides can be expected [37]. Indeed, band gap values published for oxynitrides fall into the interval 1.8-3.3 eV. The band gap overlap with the solar spectrum makes this class of materials interesting for applications as pigments and visible-light driven photocatalysts.

Due to the similarity in electronic structure of d^0 -oxides and oxynitrides, the relation between the electronegativity, crystal structure and electronic structure, established for oxides [5], is valid also for d^0 -perovskite-type oxynitrides. This allows a qualitative prediction of optical properties for new perovskite-type oxynitrides and allows to design new visible-light activated materials for various applications.

Additionally, due to its larger ionic radii and lower formal oxidation state, the N^{3-} -ion is more polarizable than the O^{2-} -ion. Hence, oxynitrides may possess polarization properties different to those of oxides [38].

From the difference in the oxidation states it follows that partial substitution of oxygen with nitrogen can be used to change the oxidation state of the cations according to the charge compensating mechanism (as it will be discussed below). This can be used to change charge carriers concentration and consequently electronic and magnetic properties of materials [39-41]. If oxygen is substituted for nitrogen in ternary oxides three possible mechanisms can compensate the additional negative charge caused by the N^{3-} - ion to keep the total electroneutrality:

1. Change of the oxidation state of the *B*-site cation $\text{LaV}^{3+}\text{O}_3 \Rightarrow \text{LaV}^{4+}\text{O}_2\text{N}$ or *B*- sites substitution with cations of higher valence (cross-substitution): $\text{K}^+\text{Ta}^{5+}\text{O}_3 \Rightarrow \text{Sr}^{2+}\text{Ta}^{5+}\text{O}_2\text{N}$
2. Replacement of 3 O^{2-} -ions by 2 N^{3-} -ions: $\text{La}_2\text{Ti}_2\text{O}_7 \Rightarrow \text{LaTiO}_2\text{N}$
3. Oxygen vacancy formation: $\text{BaTi}^{4+}\text{O}_3 \Rightarrow \text{BaTi}^{4+}\text{O}_{3-3x/2}\text{N}_x$

These charge compensating mechanisms can be used to control the amount of nitrogen in the oxide sublattice and, consequently, physical chemical properties of oxynitrides.

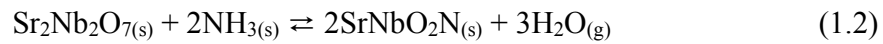
The electronegativity of fluorine (4.10), is higher than that of oxygen. Therefore, bigger optical band gaps can be predicted for oxyfluorides. Besides, due to the lower formal charge of F^- compared to that of O^{2-} , a partial substitution of oxygen with fluorine can lead to the decrease in the formal oxidation state of the *B*-site cation.

1.5. Synthesis of oxynitrides

To synthesize oxynitrides from oxides a suitable nitriding agent is required. Molecular nitrogen (N_2) would be an ideal candidate. However, its triple bond ($\text{N}\equiv\text{N}$) is one of the strongest in nature ($\Delta H_{diss}^0 = 946 \text{ kJ mole}^{-1}$). Therefore, in most of cases the direct reaction between N_2 and oxides requires high activation energy. It was also proven experimentally that the H_2/N_2 -mixtures do not promote effective nitridation either [40].

Currently ammonia NH_3 is a widely used nitriding source. The corresponding reaction between a suitable solid precursor and gaseous ammonia is often referred to as “thermal ammonolysis”. Oxides ($A_2B_2O_7$, ABO_4 with a *B*-site cation being in its stable oxidation state) and oxides-carbonates mixtures ($ACO_3-B_xO_y$) are among the most often used precursors for the perovskite-type oxynitrides synthesis [40, 41]. The reaction between a precursor and ammonia is normally carried out at atmospheric pressure in the temperature region of $T = 900\text{--}1273 \text{ K}$.

Ammonia decomposition reactions on oxides surfaces are not well studied. However, it is suggested that ammonia dissociates at the surface, forming active nitriding species (N , NH , NH_2) and molecular hydrogen [42, 43]. The latter reacts with the lattice oxygen to form water, while nitrogen is introduced into the lattice, *e.g.*:



The formation of thermodynamically stable molecules such as water ($\Delta G_f^o(\mathbf{1000}) = 192.603 \text{ kJ mole}^{-1}$) and carbon dioxide ($\Delta G_f^o(\mathbf{1000}) = -395.865 \text{ kJ mole}^{-1}$) as well as the overall entropy increase are the main driving forces of the ammonolysis. Molecules of H_2O and CO_2 are removed from the system by means of the ammonia flow, thus preventing the possible back reactions. At ambient pressure and if the components of the $\text{H}_2/\text{N}_2/\text{NH}_3$ mixture have reached their equilibrium partial pressures before contacting the sample (equilibrium case), the composition of the reacted sample depends upon temperature and water partial pressure in the system ($p(\text{H}_2\text{O})$). A lower limit to $p(\text{H}_2\text{O})$ is determined by the water in the ammonia source (if not using moisture absorbers) [44].

Ammonia dissociation proceeds according to the equation:



The temperature dependence of the ammonia formation equilibrium constant K_f^o is shown on Figure 1.5.

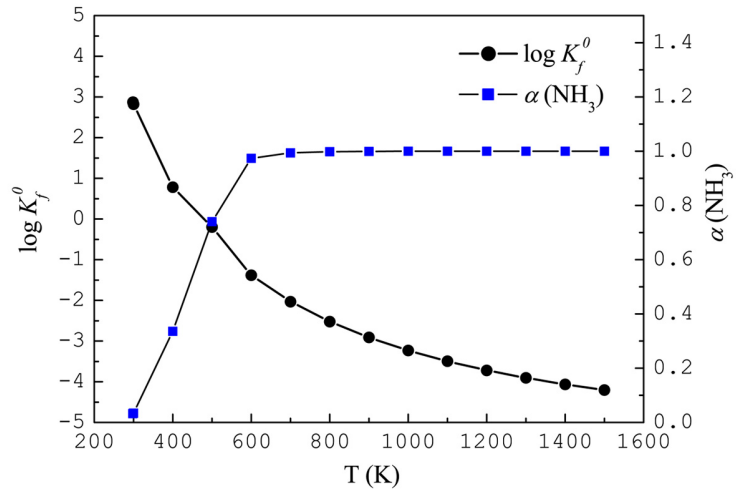


Figure 1.5. Temperature dependence of the ammonia formation equilibrium constant (K_f^0) and dissociation rate (α).

At equilibrium conditions, K_f^0 can be expressed by partial pressures (p) or mole fractions of N_2 , H_2 and NH_3 :

$$K_f^0(T) = \frac{p(NH_3)}{p^{3/2}(H_2)p^{1/2}(N_2)} = \frac{16}{\sqrt{27}} \frac{x}{(1-x)^2} \quad (1.5)$$

where

x – mole fraction of dissociated NH_3 .

The solution of this equation allows obtaining a temperature dependence of partial pressures of N_2 , H_2 and NH_3 as well as a temperature dependence of the NH_3 dissociation constant (α):

$$\alpha = \frac{1-x}{1+x} \quad (1.6)$$

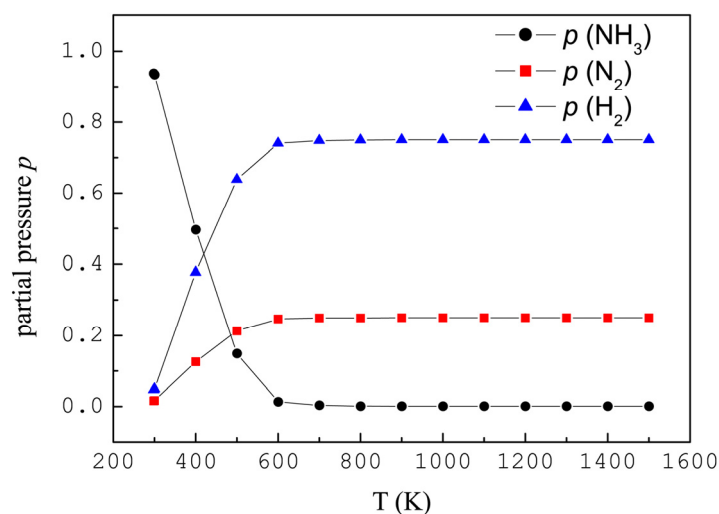


Figure 1. 6. Temperature dependence of equilibrium partial pressure of gaseous NH_3 , H_2 and N_2 .

At $T > 573$ K (the temperature region, where the most of the oxynitrides have been synthesized) ammonia is mostly dissociated into N_2 and H_2 (Figure 1.6), which are not an effective nitriding sources. That is why it is important to increase ammonia flow with temperature [40]. Additionally, increasing ammonia flow promotes faster water removal [44, 45] and the renewal of active nitriding species over the sample.

So far, the formation of the perovskite type oxynitrides of the general formula $AB(\text{O},\text{N})_3$ have been reported for A = rare-earth (RE), alkaline-earth (AE) and B = Zr, Ti, Ta, Nb, Mo, V, W (Table 1.2). The effective electronegativity of the transition-element ions in their air stable oxidation states decreases in the following order: $\text{Mo}^{6+} > \text{W}^{6+} > \text{Nb}^{5+} \sim \text{Ti}^{4+} > \text{Ta}^{5+} > \text{Zr}^{4+}$. Hence, the reducibility of these ions decreases in the same order and the formation of mixed-valent oxynitrides becomes less favorable. Indeed, thermal ammonolysis of oxide precursors containing Ta^{5+} and Zr^{4+} does not affect the oxidation state of these ions [45, 46], whereas thermal ammonolysis of Mo^{6+} and W^{6+} containing oxide precursors always yields in mixed-valent oxynitrides [47-49].

Binary nitrides formation is a problem when oxide/carbonate mixtures are used as starting precursors [50]. In that case a mineralizer (typically KCl , NaCl , CaCl_2 , which melts at the

temperature of the oxynitride phase formation) can be added into the starting mixture. Mineralizers help to overcome the diffusion barrier between the ions. This allows to achieve single-phase oxynitrides. The mineralizer can be afterwards leached with water.

The electronegativity of the *A*-site cation can also influence the reducibility of the *B*-site cation. This influence is normally discussed in terms of the so-called *positive inductive effect* [6]. Within one group of the Periodic Table the strength of the positive inductive effect decreases with the decrease of the ionic radius of the element. Thus, for *e.g.* Ca^{2+} , Sr^{2+} and Ba^{2+} the strength of the positive inductive effect decreases in the following order $\text{Ba}^{2+} > \text{Sr}^{2+} > \text{Ca}^{2+}$. The reducibility of the *B*-ions decreases in the same order [6]. The influence of the *A*-site cation electronegativity on the phase purity of the formed oxynitrides was observed during the synthesis of Nb^{5+} -based oxynitride perovskites. Whereas single-phase BaNbO_2N and SrNbO_2N are easily formed during the thermal ammonolysis of the corresponding oxide-carbonate mixtures [38, 51, 52] and oxide precursors at $T = 1173\text{-}1373$ K, it was very difficult to prepare a single phase CaNbO_2N [38, 50]. To synthesize this material phase-pure the temperature should be significantly lowered (down to $T = 1003$ K) and preferably soft chemistry produced oxide precursor has to be used (see below). The weak positive inductive effect of Ca^{2+} can be also be the reason why mixed-valent Mo-, V-, W- based oxynitride-perovskites with Ca^{2+} on the *A*-site are still not known.

The N^{3-} diffusion rate is lower at lower *T*. In that case to decrease the time of the oxynitride phase formation, soft chemistry produced precursors (Chapter 3) with small particle size and high surface area can be used. Thus, the synthesis of a single phase LaZrO_2N was only possible with the citrate method produced oxide precursor of low crystallinity. Using the precursor, produced by the standard ceramic method led to a noncomplete transformation of $\text{La}_2\text{Zr}_2\text{O}_7$ to LaZrO_2N [46].

Table 1.2. Perovskite and perovskite related oxynitrides, their structures and synthesis methods reported in the ICSD and Scopus databases

Compound	Space group	Synthesis method	Ref.
LaZrO ₂ N	<i>Pnma</i>	La ₂ Zr ₂ O ₇ (citrate);NH ₃ ; 1273 K	[46]
<i>Ln</i> TiO ₂ N (<i>Ln</i> = La ³⁺ , Nd ³⁺)	<i>I</i> $\bar{1}$ (La ³⁺), <i>Pnma</i> (Nd ³⁺)	<i>Ln</i> ₂ Ti ₂ O ₇ , NH ₃ , 1223 K	[46, 53]
Sr _{1-x} La _x TiO _{3-x} N _x	<i>Pm</i> $\bar{3}m - I$ $\bar{1}$	Sr _{1-x} La _x TiO _y , NH ₃ , 1223 K	[54]
Ba _{1-x} La _x TiO _{3-x} N _x	-	Ba _{1-x} La _x TiO _y , NH ₃ , 1223 K	[54]
LaVO _{3-x} N _x (x = 0-0.9)	-	LaVO ₄ , NH ₃ , 1973-1073 K	[39]
LaNbON ₂	-	La ₂ Nb ₂ O ₈ , NH ₃ , 1223 K	[53]
CaNbO ₂ N	<i>Pnma</i>	Ca ₂ Nb ₂ O ₇ (citrate), NH ₃ , 1003 K	[50]
SrNbO ₂ N	<i>I4/mcm</i>	SrCO ₃ -Nb ₂ O ₅ -flux, NH ₃ , 1223 K	[52]
Sr ₂ NbO ₃ N	<i>I4/mmm</i>	SrCO ₃ -Nb ₂ O ₅ , NH ₃ , 1173-1323 K	[55]
Sr ₃ Nb ₂ O ₅ N ₂	-	SrCO ₃ -Nb ₂ O ₅ , 1173-1323 K	[55]
BaNbO ₂ N	<i>Pm</i> $\bar{3}m$	BaCO ₃ + Nb ₂ O ₅ , NH ₃ , 1273 K	[56]
Ba _{1-x} Sr _x TaO ₂ N	<i>Pm</i> $\bar{3}m$	BaTaO ₂ N-SrTaO ₂ N, NH ₃ , 1123 K	[51]
<i>Ln</i> TaON ₂ (<i>Ln</i> = La ³⁺ → Dy ³⁺)	-	<i>Ln</i> ₂ Ta ₂ O ₈ , NH ₃ , 1223 K	[53, 57]
LaTaON ₂	<i>C2/m</i>	La ₂ Ta ₂ O ₈ -flux, NH ₃ , 1173-1273 K	[58]
Ca _{1-x} La _x TaO _{2-x} N _{1+x}	<i>Pnma - C2/m</i>	CaCO ₃ -La ₂ O ₃ -Ta ₂ O ₅ -flux, NH ₃ , 1123K	[27]
CaTaO ₂ N	<i>Pnma</i>	CaCO ₃ -Ta ₂ O ₅ -flux, NH ₃ , 1173- 1273 K	[58]
SrTaO ₂ N	<i>I4/mcm</i>	SrCO ₃ -Ta ₂ O ₅ -flux, NH ₃ , 1173-1273 K / SrO-TaON, N ₂ , 1773 K	[38, 45]
Sr ₂ TaO ₃ N	<i>I4/mmm</i>	SrCO ₃ -Ta ₂ O ₅ , NH ₃ , 1173-1223 K / SrO-TaON, N ₂ , 1773 K	[45, 59]
BaTaO ₂ N	<i>Pm</i> $\bar{3}m$	BaCO ₃ -Ta ₂ O ₅ , NH ₃ , 1173-1223 / TaON+BaO, N ₂ , 1773 K	[45, 56]
Ba ₂ TaO ₃ N	<i>I4/mmm</i>	BaCO ₃ -Ta ₂ O ₅ , NH ₃ , 1173-1223 K /	[45]

		BaO-TaON, N ₂ , 1773 K	
LaWO _{0.4} N _{2.6}	$I\bar{4}$	La ₂ W ₂ O ₉ , NH ₃ , 973-1173	[60]
EuWO _{1.58} N _{1.42}	$Pm\bar{3}m$	Eu ₂ W ₂ O ₉ , NH ₃ , 1073-1173	[61]
SrWO _{1.7} N _{1.3}	$Pm\bar{3}m$	SrWO ₄ , NH ₃ , 1223 K	[62]
SrWO ₂ N	$Pm\bar{3}m$	SrWO ₄ , NH ₃ , 1173 K	[49]
SrMoO _{2.6} N _{0.4}	$Pm\bar{3}m$	SrMoO ₄ , NH ₃ , 1073 K	[48]
SrMoO _{2.5} N _{0.5}	$Pm\bar{3}m$	SrMoO ₄ , NH ₃ , 1123 K	[49]
AZr _x Ta _{1-x} O _{2+x} N _{1-x} (A = Ba ²⁺ , Sr ²⁺ , Ca ²⁺)	$Pm\bar{3}m, Pcmn$	A-Ta-Zr sol, NH ₃ , 1273 K	[63]
A _{0.5} La _{0.5} TaO _{1.5} N _{1.5} (A = Ca ²⁺ , Sr ²⁺ , Ba ²⁺)	<i>Pnma</i>	La ₂ O ₃ -ACO ₃ , Ta ₂ O ₅ , NH ₃ , 1273 K	[64]
BaSc _{1/3} Ta _{2/3} O _{8/3} N _{1/3}	<i>P2₁/n</i>	BaCO ₃ -Sc ₂ O ₃ -Ta ₂ O ₅ , NH ₃ , 1273 K	[65]
LaMg _{1/3} Ta _{2/3} O ₂ N,	<i>P2₁/n</i>	La ₂ O ₃ -MgO-Ta ₂ O ₃ , NH ₃ , 1143 K	[65]
LaMg _{1/2} Ta _{1/2} O _{5/2} N _{1/2}			
Ln ₂ AlO ₃ N (Ln = La ³⁺ , Nd ³⁺ , Sm ³⁺)	<i>I4mm</i> (La ³⁺)	Ln ₂ O ₃ -AlN, N ₂ , 1623 K	[66, 67]

1.6. Thermal stability of perovskite-type oxynitrides.

Perovskite-type oxynitrides undergo thermal reoxidation when heated in the synthetic air. The reaction often proceeds *via* the formation of a *reoxidation intermediate phase* (Figure 1.7). Thermal reoxidation intermediates were discovered for oxynitrides of various structural types (Table 1.3) [68, 69]. The main features of these phases are:

1. Higher weight than the oxide phase;
2. Amorphous or partly amorphous;
3. High thermal stability, up to T = 1200 K (Chapter 3);
4. Presence of N₂- entities bonded to the transition metal.

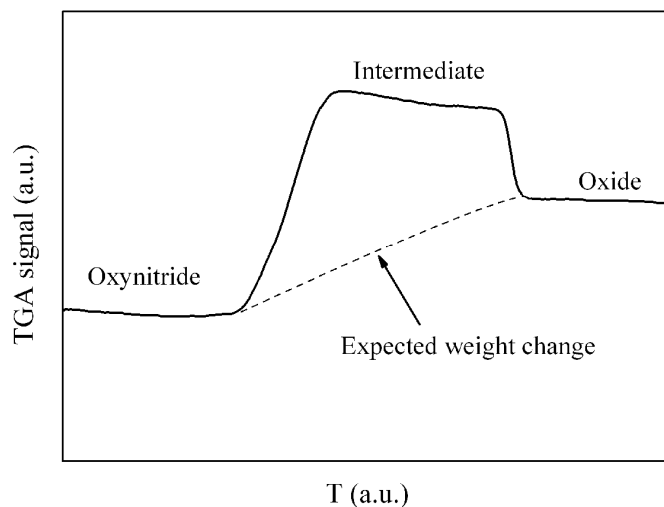


Figure 1.7. A typical thermal reoxidation curve of the perovskite-type oxynitride. The solid line represents the weight difference measured during the thermal reoxidation experiment. The dashed line represents the expected weight difference.

Table 1.3. Thermal reoxidation intermediates of selected oxynitrides

Starting oxide	Structural type	Reoxidation intermediate	Reference
LaTiO ₂ N	Perovskite	LaTiO _{3.5} (N ₂) _{0.32}	[68]
La _{0.91} W _{0.91} O _{1.37} N _{1.63}	Perovskite	LaWO _{4.5} (N ₂) _{0.23}	[68]
TaON	Baddeleyite	TaO ₂ (N ₂) _{0.10}	[70]
Zr ₂ N ₂ O	Bixbyite	ZrO ₂ (N ₂) _{0.028}	[71]
Sr ₂ NbO _{2.8} N	Huddleston-Popper	Sr ₂ NbO _{4.5} (N ₂) _{0.20}	[72]
La _{0.9} Ba _{0.1} TiO _{2.1} N _{0.9}	Perovskite	La _{0.9} Ba _{0.1} TiO _{3.45} (N ₂) _{0.31}	[73]
La _{0.7} Ba _{0.3} TiO _{2.3} N _{0.7}	Perovskite	La _{0.7} Ba _{0.3} TiO _{3.35} (N ₂) _{0.26}	[73]
La _{0.5} Ba _{0.5} TiO _{2.5} N _{0.5}	Perovskite	La _{0.5} Ba _{0.5} TiO _{3.25} (N ₂) _{0.23}	[73]
Y ₄ Si ₂ O ₇ N ₂	Cuspidine	Y ₄ Si ₂ O ₁₀ (N ₂) _{0.75}	[74]
Y ₅ (SiO ₄) ₃ N	Apatite	Y ₁₀ Si ₇ O ₂₉ (N ₂) _{0.335}	[75]
Y _{2.67} W _{1.33} O _{3.79} N _{2.80}	Fluorite	Y ₂ WO ₆ (N ₂) _{0.20}	[68]
Ti _{0.67} O _{0.42} N _{0.58}	rock-salt	TiO ₂ (N ₂) _{0.06}	[68]
Nb _{0.56} O _{0.40} N _{0.60}	rock-salt	Nb ₂ O ₅ (N ₂) _{0.43}	[68]

Early studies reveal that formation and decomposition of the intermediate phase are accompanied by molecular nitrogen evolution. Initially it was believed that nitrogen in the intermediate phase is represented only by N₂-species, which are weakly bonded to the oxide matrix, forming binuclear complexes, which contain the fragment Me···N≡N···Me. This weak bonding would not seriously affect the electron density distribution of the dinitrogen molecule. Hence, it stays symmetric and IR-inactive. Therefore the methods applied to prove the presence of dinitrogen species in the intermediates are XPS and Raman spectroscopy [68, 69]. However, the formation of the weakly bonded binuclear complexes of dinitrogen can not explain a high thermal stability of intermediates. Raman studies of Rachel *et al.* [50] reveal Me≡N type of bonding for the Ta- containing intermediates. Although previously only N₂ molecules were claimed to be evolved during the intermediates formation stage, a recent study of Aguiar *et. al* reveals an additional NO and NO₂ retention during the intermediate formation step [76].

1.7. Optical properties of perovskite-type oxynitrides. Pigments.

As it was already mentioned in Chapter 1.4, optical band gaps of *d*⁰-perovskite-type oxynitrides overlap with the solar spectrum, which makes these materials attractive for pigments and visible light driven photocatalysts applications. Therefore, understanding the relation between the composition and the band gap values of perovskite-type oxynitrides and designing new oxynitrides with small optical band gaps are of great interest.

Optical band gap values of a number of *d*⁰-perovskite-type oxynitrides, containing *e.g.* Zr⁴⁺, Ti⁴⁺, Ta⁵⁺ and Nb⁵⁺ are given in Table 1.4.

For oxynitrides of the general formula *ABO*₂N (*A* = Ca²⁺, Sr²⁺, Ba²⁺, *B* = Ta⁵⁺, Nb⁵⁺) the band gap decreases with the increasing *A*-cationic radius. The average band gap value of the Nb⁵⁺-containing oxynitrides was found to be lower than that of Ta⁵⁺-containing oxynitrides (Table 1.4). This finding is in accordance with the established relation between the electronegativity of the *B*-site cation and the optical band gap for *d*⁰-perovskite-type oxides, which was discussed above (Chapter 1.2).

Table 1.4. Optical band gaps and colors of ternary perovskite-type oxynitrides (selected from the database Scopus)

Compound	Band gap, eV	Color	Ref.
LaZrO ₂ N	-	White	[46]
LaTiO ₂ N	2.0–2.1	Brown	[54, 77, 78]
CaTaO ₂ N	2.4, 2.75	Yellow	[27, 38]
SrTaO ₂ N	2.1	Orange	[38]
BaTaO ₂ N	1.8	Red	[38]
LaTaO ₂ N	2.0–2.1	Red	[27, 79]
CaNbO ₂ N	2.1	Ochre	[38, 50]
SrNbO ₂ N	1.9	Brown	[38]
BaNbO ₂ N	1.8	Dark-brown	[38]

The cross-substitution was employed to vary the nitrogen content and consequently the band gap of oxynitrides.

Cross-substitution of Ca²⁺ in CaTaO₂N with La³⁺ and O²⁻ with N³⁻ yield in series of solid solutions of the general formula Ca_{1-x}La_xTaO_{2-x}N_x (x = 0.05–1.00). The nitrogen content and consequently the band gap was tuned by varying the Ca²⁺-content. The band gap decreases linearly from 2.75 eV (CaTaO₂N) to 2.0 (LaTaON₂). The synthesized materials possess bright colors (from yellow to red), and good thermal and chemical stability. Due to their remarkable optical and chemical properties Ca_{1-x}La_xTaO_{2-x}N_x oxynitrides were evaluated as substitutants for toxic Cd-containing yellow-red pigments [27].

Recently, optical properties of solid solutions of the general formula Sr_{1-x}La_xTiO_{3-x}N_x (x = 0.0–1.0) have been reported [54]. Although, the same principle of the co-substitution and the O/N-content control as in the Ca_{1-x}La_xTaO_{2-x}N_x system was realized, the band gap does not vary linearly with the nitrogen content. This can be explained in the following way. Increase of the degree of x within the Ca_{1-x}La_xTaO_{2-x}N_x series leads to a higher nitrogen content and increasing structure distortion ($r(\text{Ca}^{2+}) < r(\text{La}^{3+})$). Both factors are favorable for the optical band gap decrease in this system. Increase of x within the Sr_{1-x}La_xTiO_{3-x}N_x system leads to increasing nitrogen content and increasing structure distortion ($r(\text{Sr}^{2+}) > r(\text{La}^{3+})$). Whereas, the nitrogen content increase leads to a band gap decrease, the structure

distortion results in the optical band gap increase (Fig. 1.4B). Thus, both these factors partly compensate each other.

1.8. Photocatalytic properties of oxynitrides.

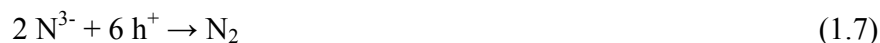
Recent efforts to improve the QE of oxide photocatalysts are concerned with improving their optical activity by means of anionic substitution. Theoretical calculations made by full-potential linearized augmented plane wave (FLAPW) formalism in the framework of the local density approximation (LDA) for S, C, N, P, F –doped TiO₂ show that *p*-states of N³⁻ and S²⁻ most effectively contribute to the band gap narrowing. Thus, N³⁻ and S²⁻ are the best candidates for a partial oxygen substitution [80]. However, only substitution with N³⁻ allows maintaining the oxide crystal structure type due to the better ionic radii matching.

Since *d*⁰ perovskite type oxides have shown a remarkable photocatalytic activity the photocatalytic properties of *d*⁰-oxynitride perovskites are of a great interest.

Indeed, since oxynitrides absorb in the visible region they are potential candidates for various photocatalytic applications (photocatalytic production of hydrogen from water or organic waste, or photocatalytic waste decomposition), *etc.* Only Zr⁴⁺, Ti⁴⁺, Ta⁵⁺, Nb⁵⁺–containing oxynitride-perovskites satisfy the stability criteria and hence, their photocatalytic properties are worthy to be examined.

Photocatalytic oxynitride-perovskites are a relatively new research topic. The first report on the photocatalytic water splitting into H₂ and O₂ with an oxynitride photocatalyst appeared in 2002. Kasahara *et. al* reported on the photocatalytic properties of LaTiO₂N and La_{0.75}Ca_{0.25}TiO_{2.75}N_{0.25} prepared by thermal ammonolysis of the citric route produced corresponding oxide precursors [77]. Photocatalytic reactions were carried out on powders, which surfaces were modified with IrO₂ (oxygen evolution catalyst) and Pt (hydrogen evolution catalyst) and in the presence of a sacrificial electron donor (methanol) and sacrificial electron acceptor (Ag⁺). The materials were tested under visible light of 420 < λ < 600 nm. The amount of 440 μmol O₂ was formed over 0.02 g of LaTiO₂N during 43 hours of irradiation. The maximum quantum efficiency achieved for the O₂ evolution was 1.5 %. Ca - modification led to a considerable increase in the quantum efficiency (from 1.5 % up to *ca.* 5 %). Moreover, substitution of 25 at % of La³⁺ in LaTiO₂N with Ca²⁺ led to a

suppression of the N₂ evolution observed during the photocatalytic oxygen production over LaTiO₂N and attributed to the reduction of the intrinsic N³⁻ with photochemically induced holes:



Later on it was found that in alkaline solutions with pH ~ 8.1 the N₂ evolution over LaTiO₂N during the photocatalytic O₂ production doesn't occur [11].

Both LaTiO₂N and La_{0.75}Ca_{0.25}TiO_{2.75}N_{0.25} were rather ineffective during the photocatalytic H₂-production tests: the maximum of 0.15 % quantum efficiency was achieved for LaTiO₂N.

Since then, photocatalytic properties of a number of Ta⁵⁺- and Nb⁵⁺-containing oxynitrides were investigated under the same experimental conditions. Ta⁵⁺-containing oxynitride-perovskites (CaTaO₂N, SrTaO₂N [81], NdTaO₂N and LaTaON₂ [79]) were able to catalyze H₂ production from water. Up to 38 μmol h⁻¹ of H₂ were achieved over LaTaON₂ [79]. However, these oxynitrides found to possess no activity during the photocatalytic oxygen production.

Recently photocatalytic properties of Nb⁵⁺-containing oxynitrides ANbO₂N (A = Ca²⁺, Sr²⁺, Ba²⁺) were investigated. The niobates with A = Sr²⁺, Ba²⁺ didn't show any photocatalytic activity, whereas CaNbO₂N was active during the photocatalytic production of oxygen (35 μmol h⁻¹ g⁻¹) [82].

Recently the first study on photocatalytic water oxidation over the perovskite related Rb_{1+x}Ca₂Nb₃O_{10-x}N_x*yH₂O (K₂NiF₄-type structure) oxynitride produced by thermal ammonolysis of Dion-Jacobson phase RbCa₂Nb₃O₁₀ in the presence of CaCO₃ was reported [83]. The materials appeared to be rather poor photocatalysts. Their maximum of the quantum efficiency for the O₂-production (0.70 %) was even lower than that of the starting oxide precursor (1.07 %). Moreover, they were found to decompose in contact with water.

As it was found before for oxides, the quantum efficiency of the oxynitrides is dependent upon the used co-catalyst. Thus, the highest evolution rate of H₂ (190 μmol h⁻¹ g⁻¹) over LaTaON₂ was achieved by adding 0.15 wt % Pt-0.25 % Ru loaded co-catalyst, whereas

separately performed tests of LaTaON₂ impregnated with 0.15 wt % of Pt and 0.25 wt % of Ru yielded in 15 and 40 $\mu\text{mol h}^{-1} \text{g}^{-1}$ of hydrogen evolution rate, respectively [79].

In some of the studies, dedicated to the synthesis and photocatalytic properties of oxynitrides it is emphasized, that low quantum efficiencies measured on oxynitride perovskites could be related to one of the following factors: complex defect structure of their surfaces, which can serve as recombination centers for the photochemically induced electron-hole couples or low absorption rate of the H₂ and O₂ evolution catalysts [11, 77].

Moreover, as it was pointed by Osterloh [29], the reported values of flat/band potentials exhibit large variations, which reflects experimental uncertainties, as well as intrinsic differences between materials, which arise from different routes used for materials preparation. The flat band potential is known to be dependent on ion absorption, surface defects and surface reactions. Yamasita *et. al* [81] stated that no O₂ evolution was detected over visible light irradiated SrTaO₂N and BaTaO₂N, whereas the authors of [82] reported on the photocatalytic oxygen production over these materials, tested under similar conditions. This difference can be explained only by deviations of synthesis procedures used for the tested materials.

The modification of oxynitride preparation procedures as well as the development of a method, which allow good impregnation rates of the co-catalysts for H₂ and O₂ evolution, has to be achieved. As a result, increase in photocatalytic activity of oxynitrides is expected.

1.9. Anionic ordering

Complete or partial O/N ordering has been reported for a number of perovskite- and perovskite-related oxynitrides, which contain cations from the VB group in d^0 -electronic configuration (Ta⁵⁺ and Nb⁵⁺) as well as Al³⁺ [52, 58]. A completely ordered N/O arrangement was reported for all the oxynitrides of the K₂NiF₄-type (Sr₂NbO_{3.3}N_{0.7} [55], Sr₂TaO₃N [45, 59], Ba₂TaO₃N [45], Nd₂AlO₃N [66]). In Ta- and Nb-containing oxynitrides of that type, N³⁻-ions occupy the equatorial positions (Fig. 1.8A) of the octahedra (along *a* and *b* axis). The ordering in these compounds is consistent with the less polarizable O²⁻-ions occupying *A*₅*BO*-octahedra (*A* = Sr²⁺, Ba²⁺, *B* = Ta⁵⁺), and are mostly surrounded by

less polarizing cations (Sr^{2+} , Ba^{2+}). More polarizable N^{3-} -ions occupy $A_4B_2\text{N}$ -octahedra (are mostly surrounded by more polarizing cations Ta^{5+} and Nb^{5+}). The type of the O/N- order found in $\text{Nd}_2\text{AlO}_3\text{N}$ is completely opposite: N^{3-} is in an octahedral AlNd_5N environment and O^{2-} occupies AlNd_5O and OAl_2Nd_4 octahedra (Fig. 1.8B). The reason for that is explained by a small difference in polarizabilities of Al^{3+} and Nd^{2+} [45]. Ta- and Al-containing oxynitrides of the K_2NiF_4 -type keep their anionic arrangement ordered up to 1673-1773 K [45, 59].

An ordered anionic arrangement was also reported for some of the simple oxynitride-perovskites. Currently, the origin of the partial or complete anionic ordering in this group of materials is not well understood. Depending on the preparation routes different degrees and directions of ordering have been reported for the same materials. For example, for SrTaO_2N prepared by thermal ammonolysis of a $\text{Ta}_2\text{O}_5/\text{SrCO}_3$ mixture with an addition of flux (NaCl), the space group $I4/mcm$ and a complete O/N-order was reported [58], while for the same compound, prepared from SrO and TaON in nitrogen atmosphere or prepared by thermal ammonolysis of $\text{Sr}_2\text{Ta}_2\text{O}_7$ with no flux a statistical distribution of O/N among the available sites was observed [45]. A completely ordered anionic arrangement was reported for LaTaO_2N prepared with an addition of the CaCl_2 flux (Fig. 1.9A). Recently, a partial O/N order was found in SrNbO_2N (Fig. 1.9B) [52]. Although, this material adopts the same space group as SrTaO_2N ($I4/mcm$), N^{3-} -ions of these compounds occupy preferably different anionic sites. It is reasonable to expect that the difference in the degree of the O/N-order reported for the simple perovskite-type oxynitrides arise from the difference in their thermal history. Therefore, it is interesting to investigate the influence of the thermal history on the O/N-order of these compounds.

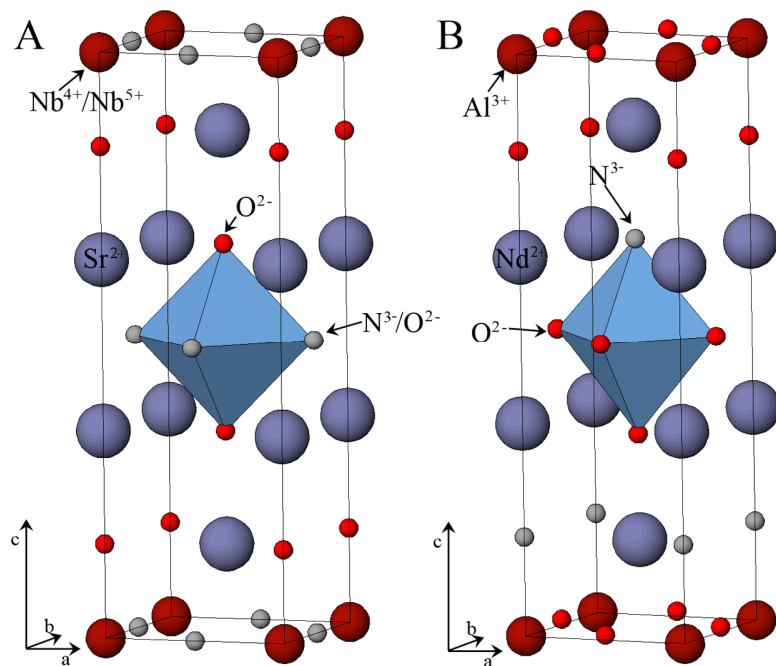


Figure 1.8. Anionic ordering in Ruddlesden-Popper oxynitrides: A. $\text{Sr}_2\text{NbO}_{3.3}\text{N}_{0.7}$ (N^{3-} is located within ab plane); B. $\text{Nd}_2\text{AlO}_3\text{N}$ (N^{3-} is located along the c -axis)

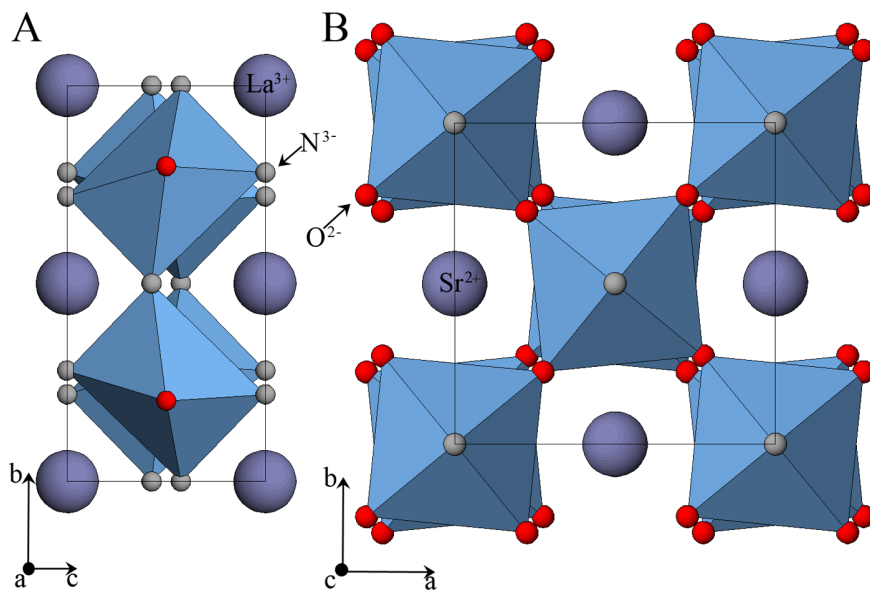


Figure 1.9. Anionic ordering in simple oxynitrides: A. In monoclinic LaTaON_2 (S.G. $C2/m$); B. In tetragonal SrTaON_2 (S.G. $I4/mcm$)

1.10. Mixed-valent oxynitride-perovskites

Since N^{3-} has a higher negative charge than O^{2-} , nitrogen insertion into the oxygen sublattice can lead to an increase of the *B*-site cation oxidation state, and, consequently, change the charge carriers concentration according to the charge compensation mechanism. This method was considered as an alternative to the cationic substitution to change electronic transport properties of the *p*-type conducting LaVO_3 [39]. Similar to the Ba^{2+} and Sr^{2+} substituted LaVO_3 the synthesized oxynitrides of general formula $\text{LaVO}_{3-x}\text{N}_x$ ($x < 0.53$) show an increased electrical conductivity compared to that of LaVO_3 . While the conductivity of Sr^{2+} and Ba^{2+} containing samples changes from semiconducting to metallic when increasing the substitution level of La^{3+} [84, 85], all the oxynitride samples remain semiconducting. Moreover, a decrease of the electrical conductivity with the increase of the nitrogen content was measured for the oxynitride samples with $x > 0.53$.

Another example, where oxygen substitution with nitrogen led to materials with modified physical properties, is the $\text{LaWO}_{3-x}\text{N}_x$ system [47]. Up to now, the members of this system with $x = 0.6$ and 0.7 were characterized. Both materials possess temperature independent low negative value of Seebeck coefficient ($|S| < 5 \mu\text{V K}^{-1}$) and low electrical conductivity ($\sim 15 \cdot 10^2 \text{ S m}^{-1}$), which is weakly temperature dependent ($E_A \sim 8 \cdot 10^{-3} \text{ eV}$). The low conductivity values indicate low mobility of charge carries, which is attributed to one of the following reasons:

1. Narrowing of the conductivity band due to the structural distortion (the crystal structure of the tested materials is tetragonal, $\overline{P4}$ with the W-(O,N)-W angle value equal to 164°).
2. Low compactness of the samples (50-60 %).
3. The presence of atoms with different formal oxidation state at the same crystallographic site (like $\text{O}^{2-}/\text{N}^{3-}$ or $\text{W}^{5+}/\text{W}^{6+}$), which is not favorable for the wide conduction band formation and can be responsible for trapping charge carriers.

Another tungsten containing oxynitride series which also possess low weakly temperature dependent electrical conductivity and high charge carriers concentration at the Fermi level (proven by magnetic susceptibility measurement) is $\text{SrWO}_{3-x}\text{N}_x$ [49].

Only low oxygen substitution with nitrogen was achieved for SrMoO_{3-x}N_x system. Up to now, studies on samples with $x \leq 0.5$ (SrMoO_{2.6}N_{0.4} and SrMoO_{2.5}N_{0.5}) have been described in the literature [48, 49]. Both neutron and x-ray diffraction studies confirmed no deviation from the cubic symmetry (space group $Pm\bar{3}m$) for these compositions. Their electrical conductivity was several orders of magnitude lower than that of SrMoO₃ and showed metallic-like temperature dependence [86]. Magnetic susceptibility measurements revealed Pauli paramagnetism ($\chi \sim 10^{-4}$ emu mol⁻¹ Oe⁻¹) at room temperature and a magnetic transition at $T \sim 54$ K. In [48] it is referred to as an antiferromagnetic transition, whereas the authors of [49] suggested a spin-glass formation. Synthesis of the members with $x > 1$ and investigation of their electronic and structural properties would be of interest.

One of the problems concerned with an accurate determination of oxynitrides electronic properties is low density of the characterized ceramics [39, 47-49]. Due to a higher bonding covalence of oxynitrides as compared to oxides, their sintering is difficult. It was reported that using an isostatic pressing technique partly solves the problem and allows increasing density of ceramic samples from 40-60 % up to 89 % [87, 88].

1.11. Scope of the present work

The first part of the present work (Chapters 3-4) is dedicated to the synthesis and characterization of d^0 -oxynitride-perovskites. The chosen systems and formulated tasks are as follows:

1. **Ca_{1-x}La_xTiO_{3-x}N_x (x = 0–0.7).** Investigation of the influence of cross substitution of Ca²⁺ with La³⁺ and O²⁻ with N³⁻ on the optical properties, structure and thermal stability of this complex oxynitride system.

Two previously reported members of this family (LaTiO₂N and La_{0.75}Ca_{0.25}TiO_{2.25}N_{0.75}) are among the most effective visible light driven water splitting photo catalysts. Therefore it is interesting to explore a lower degree of substitution in the Ca_{1-x}La_xTiO_{3-x}N_x system and to establish crystal structure-optical properties relation for the system. Moreover, optical properties of that system can be potentially interesting for the pigment application. Since that application of these

materials requires working in air, thermal stability of the compounds has to be further investigated.

2. **LaNbON₂**. Since Nb⁵⁺ possesses the lowest electronegativity among the early transition metal cations with the same electronic configuration and due to the high nitrogen content, which potentially can be achieved, LaNbON₂ is expected to possess one of the smallest optical band gaps among the known oxynitrides. Relatively few information on this material is available in the literature. Its preparation by thermal ammonolysis of LaNbO₄ oxide precursor and lattice parameters were firstly reported by Marchand *et al.* [53] Apart from this, there is no further information on that material available. In the present study we were focused on the preparation of LaNbON₂ samples suitable for the crystallographic characterization, determination of its crystallographic parameters, investigation of the anionic composition and anionic distribution dependence from thermal history as well as characterization of its optical, photochemical properties and thermal stability.

The second part of the work (Chapter 5) is dedicated to the synthesis and characterization of Mo-containing mixed-valent oxynitride-perovskites. The following systems have been investigated:

3. **SrMoO_{3-x}N_x (x > 1)**. Up to now the only known molybdenum containing oxynitride-perovskite system is SrMoO_{3-x}N_x (x = 0.4, 0.5) [48, 49]. It was prepared by thermal ammonolysis of SrMoO₄ containing Mo in its air-stable formal oxidation state +6, at T = 1023-1073 K. In this system the formal oxidation state of molybdenum varies between +4.4 and +4.5 depending on the anionic composition. Herein we report on synthesis of previously unreported highly substituted SrMoO_{3-x}N_x (with x > 1, e.g. containing Mo⁵⁺/Mo⁶⁺), examination of their crystal structure, anionic composition and distribution, physical properties and thermal stability.
4. **CaMoO_{3-x}N_x, BaMoO_{3-x}N_x**. Although perovskite-type oxides CaMoO₃ and BaMoO₃ are known [86, 89-91], no reports on the synthesis of the corresponding oxynitrides are available in the literature. Thus, possible thermal ammonolysis synthesis methods for previously unreported CaMo(O,N)₃ and BaMo(O,N)₃ were developed.

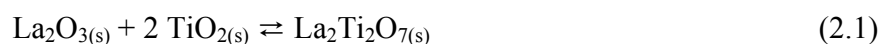
The crystal structure of $\text{CaMo}(\text{O},\text{N})_3$ and $\text{BaMo}(\text{O},\text{N})_3$ was compared with that of the corresponding oxides CaMoO_3 and BaMoO_3 .

2. Experimental techniques

2.1. Synthesis of oxide precursors

2.1.1. Ceramic method

Polycrystalline $\text{Ca}_{1-x}\text{La}_x\text{TiO}_{3+y}$ were synthesized by a standard ceramic method. Stoichiometric amounts of La_2O_3 , $\text{Ca}(\text{NO}_3)_2 \cdot 4\text{H}_2\text{O}$ and TiO_2 were thoroughly mixed with ethanol in an agate mortar and annealed 3 times (24 hours each time) at $T = 1673$ K. As an example, the reaction between La_2O_3 and TiO_2 can be expressed by the following equation:



During ceramic synthesis the phase formation occurs at the interphase between the reacting particles. If the particles are not in contact, the ions have to diffuse to the reaction zone, which requires heating the reactants to relatively high temperatures (typically above 1373 K). Besides, the reactants should be thoroughly grinded to obtain a homogeneous composition. In many cases, to achieve a single phase compound, several heating-regrinding cycles are required.

2.1.2. Soft chemistry synthesis

The decomposition of complex precursors containing a premix of the cations on a molecular level can be used as an alternative to the standard ceramic method to achieve single phase crystalline oxides [92]. This soft chemistry (*chimie douce*) approach consists in the preparation of the stable metal chelate complexes with certain α -hydroxycarboxylic acids (citric acid, glycine *etc.*) with their subsequent thermal decomposition. In the metal chelate matrix the starting cations are mixed on a molecular level. The phase formation occurs at relatively low temperatures (typically below 1273 K) because no diffusion

processes are necessary [92, 93]. Besides, molecular level mixing allows to maintain good chemical homogeneity of the synthesized oxides.

In the present work a modified Pechini method, which employs citric acid as a complexing agent was used to synthesize Nb⁵⁺-, Ti⁴⁺- [94, 95] (Chapters 3 and 4) and Mo⁶⁺-containing [96] (Chapter 5) oxide precursors as shown on Figs.2.1-2.3.

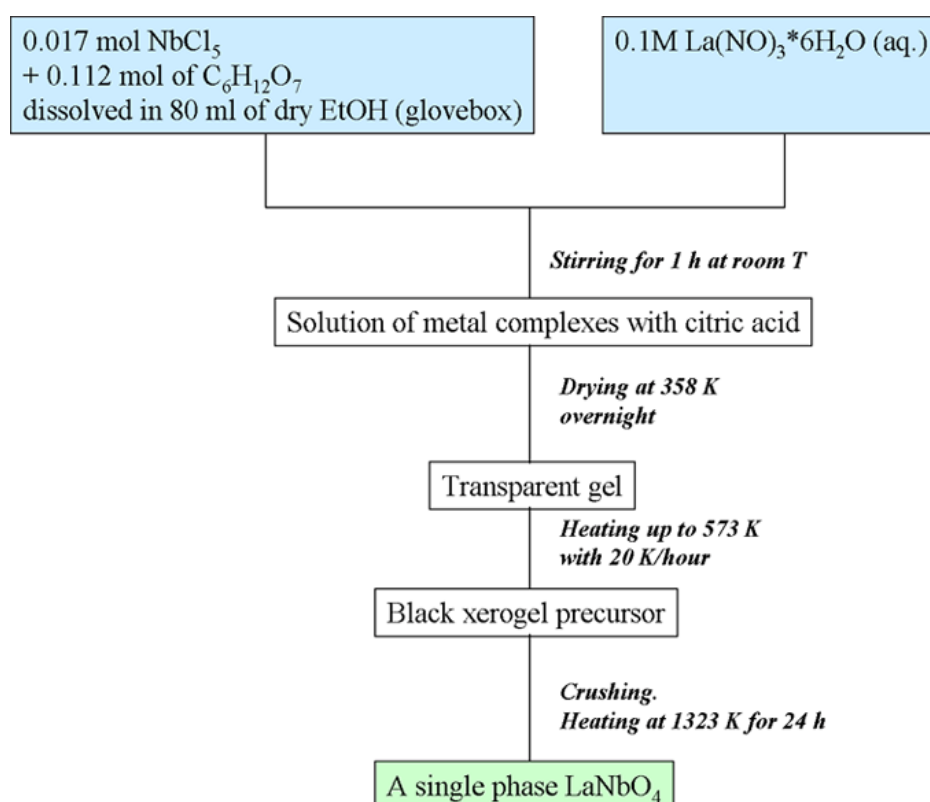


Figure 2.1. Flow chart for the synthesis of the LaNbO₄ oxide precursor.

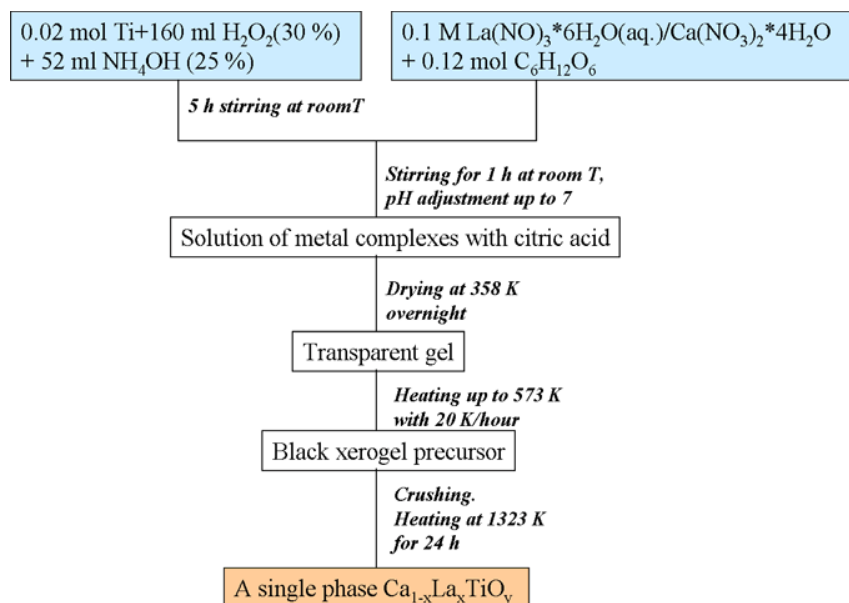


Figure 2.2. Flow chart for the synthesis of $\text{Ca}_{1-x}\text{La}_x\text{TiO}_y$ oxide precursors.

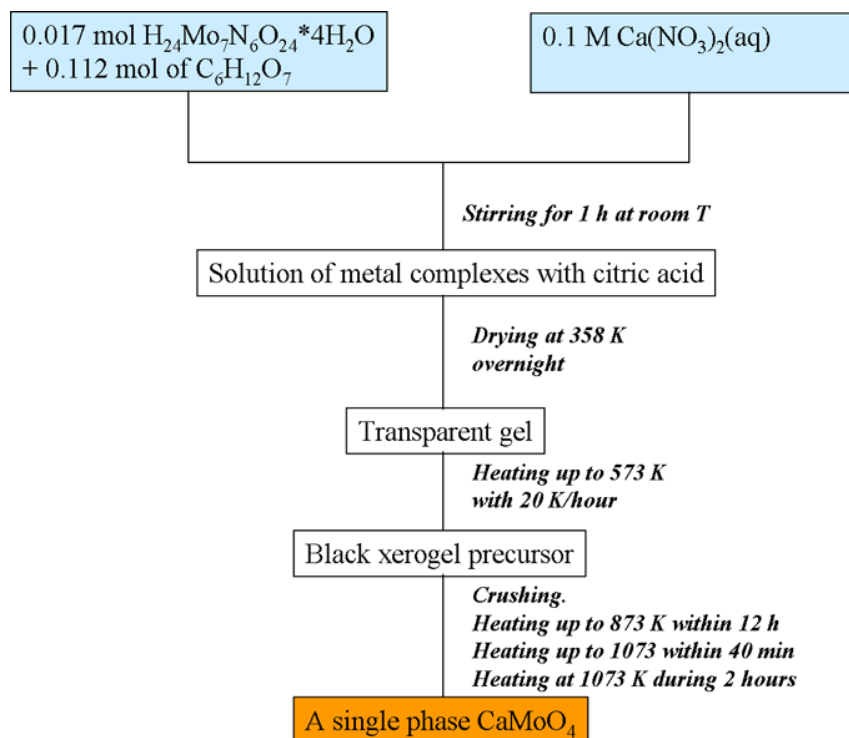
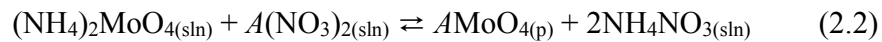


Figure 2.3. Flow chart for the synthesis of CaMoO_4 oxide precursor.

2.1.3. Precipitation from aqueous solution

This method was employed to synthesize molybdates of the general formula $AMo^{6+}O_4$ ($A = Ca^{2+}, Sr^{2+}, Ba^{2+}$) [88, 96]. Synthesis of these materials by the ceramic method requires using MoO_3 as one of the reagents. The main disadvantage of using this oxide is its high vapor pressure (10^{-2} mbar at $T \sim 873$ K). Therefore, to obtain $AMo^{6+}O_4$ with the proper stoichiometry the atomic ratio of $A:Mo$ and the synthesis temperature have to be optimized. However, oxide $AMoO_4$ can be easily prepared either by precipitation or by a soft chemistry approach (as it was mentioned before for $CaMoO_4$).

To prepare $AMoO_4$ 0.04 mol MoO_3 (JMC, Specpure) is dissolved in a minimal amount (*ca* 20 ml) of NH_3 (aq, 25 %) and precipitated with 100 ml of an aqueous solution of $Sr(NO_3)_2$ (Merck, >99%) with the concentration 0.4 mol L^{-1} :



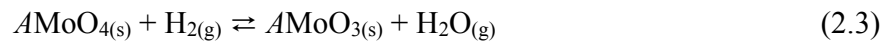
The precipitate was washed with distilled water, dried and annealed at 1073 K for 4 hours to form a phase pure well crystalline $AMoO_4$.

2.1.4. Reduction of $AMoO_4$ to $AMoO_3$

$CaMoO_3$ was synthesized by reduction of $CaMoO_4$ produced by the citrate method with forming gas (5% H_2 / 95% N_2 , 99.999% purity, Pangas) [90]. The reduction of 1 g of $CaMoO_4$ was carried out at 1173 K during 12 hours (with an intermediate regrinding after 4 h and 8 h of the reaction) under a forming gas flow of $100\text{-}300 \text{ mL min}^{-1}$ [95]. The forming gas was supplied through a gas inlet quartz tube with a diameter of 5.8 mm ending above the sample and about 2 mm from the reactor end. After the reaction, the sample was quenched down to room temperature within 1 minute

$SrMoO_3$ and $BaMoO_3$ were synthesized by reduction of the corresponding oxide precursors $SrMoO_4$ and $BaMoO_4$ (1 g) with a forming gas flow of $250\text{-}300 \text{ mL min}^{-1}$. The reduction was carried out at $T = 1373$ K and $T = 1473$ K during 5 and 15 hours for $SrMoO_4$ and $BaMoO_4$, respectively.

The reduction of $AMoO_3$ proceeds according to the following equation:



All the reduction experiments were done in a horizontal tubular quartz reactor with an internal diameter of 30 mm.

2.2. Thermal ammonolysis

All the oxynitride samples were produced by a thermal ammonolysis reaction carried out in a self-made set-up (Fig. 2.4).

The general aims of the construction were the following:

1. To obtain oxynitride powders with a uniform anionic composition.
2. To apply different cooling programs for the samples.
3. To allow working with fluxes.
4. To allow simultaneous thermal ammonolysis experiments for several precursors (screening).

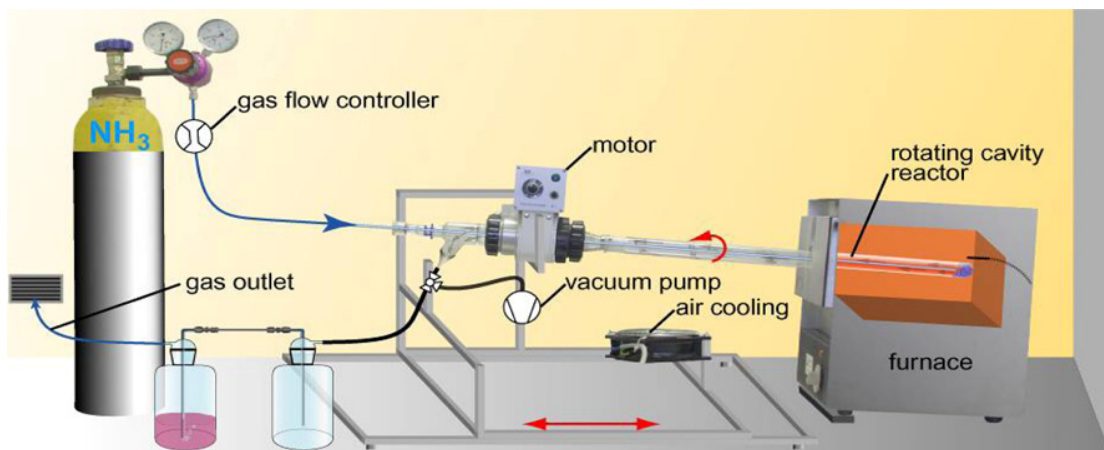


Figure 2.4. The scheme of the self-made thermal ammonolysis set-up.

The scheme of the self-built thermal ammonolysis set-up is shown on Fig. 2.4. The main parts of the setup are: the furnace (Labortherm N3, operating at T up to 1273 K) with a temperature controller (REX-C₁₀₀₀ from RKC), the tubular reactor, the gas supply and the

evacuation system. The gas supply and the evacuation system include a mass flow controller (model 5850E from Brooks Instrument), gas communications (Swagelog), a digital vacuummeter (DVR 2 from Vacuubrand) and a membrane pump (MZ-2 C from Müller+Krempel AG). The reactor with an internal diameter of 30 mm is connected to the motor with an adjustable rotation speed (KRvrTD 65/45 from Büchi rotavapor) and an air fan, all mounted on the Al-made frame (Aphoenix mechano from RK Rose+Krieger). The frame itself was placed on the Al-made sledges. The sledges allow that the reactor slides along the horizontal plane for fast introduction and the withdrawal of the reactor from the furnace. This is especially important, when the quenching of the material is required. The purpose of the motor is to rotate the reactor and thus to mix the material during the ammonolysis reaction with the intention to improve the uniformity of the oxynitride anionic composition by better exposure of the powder to the gas flow.



Figure 2.5. Photograph of the self built Al₂O₃ sample holder used for the screening experiments.

A special sample holder was designed to react different precursors under the same ammonolysis conditions at the same time. It was made from one piece of Al₂O₃ (Fig. 2.5). Its lower part was cut and polished to allow sliding inside the reactor. Four holes were drilled in its upper part to carry four different materials.

The reactors used for the ammonolysis are made of two different materials: Al₂O₃ and SiO₂. The alumina reactor is used for the screening experiments and for the experiments which involve mineralizers. The quartz reactor is used, when the material has to be quenched.

Gases are supplied through the gas inlet quartz tube placed 1-2 cm from the sample. Such a close location of the NH₃ supplying tube to the sample surface is necessary to prevent NH₃ decomposition before contacting the sample.

The thermal ammonolysis reactions were performed in the following steps:

1. Air was evacuated from the system by using the vacuum pump until the rest pressure of 30 - 40 torr was reached;
2. The reactor was filled with nitrogen until the pressure inside the tube slightly exceeded atmospheric pressure;
3. Nitrogen was replaced by ammonia;
4. The reactor was heated up to the ammonolysis temperature;
5. After the ammonolysis completion the reactor was cooled down to room temperature.

Ammonia of >99.98 % purity was used for all experiments.

Cooling of the samples was normally performed in 3 different ways:

1. Quenching within 1 minute down to room temperature;
2. Slow cooling under NH_3 ;
3. Slow cooling under N_2 (99.999 % purity).

Potassium chloride (KCl) was used as a mineralizer (flux) during the synthesis of LaNbON_2 (Chapter 4). The flux was mixed with the oxide precursor in molar ratio of 3(flux):1(oxide). After the ammonolysis the flux was washed out with deionized water.

2.3. Structural and microstructural characterization by diffraction techniques

X-ray-, neutron- and electron diffraction investigations were carried out to obtain structural and microstructural information on the starting oxide, the oxynitride and the reoxidation intermediate powders as explained below.

2.3.1. X-ray diffraction

The experiments were performed using a Phillips X'Pert PRO MPD Θ - Θ System. Single crystalline silicon sample holders for low background were used for the qualitative phase analysis; scattered x-rays were detected with a linear detector X'Celerator. Front load infinite thickness sample holders made of steel were used for the quantitative analysis and

crystallographic parameters determination; scattered x-rays were detected with a proportional counter. A secondary monochromator made from pyrolytic graphite was used to reduce the fluorescent background contribution.

2.3.2. Neutron diffraction

In the present work thermal neutrons ($\lambda = 1.494 \text{ \AA}$) were used to study the anionic composition and to determine both atomic coordinates and thermal displacement factors of the synthesized oxynitrides.

The neutron diffraction (ND) data were recorded at the high resolution powder diffractometer for thermal neutrons (HRPT) [97] located at the Swiss Spallation Neutron Source (SINQ) of the Paul Scherrer Institut in Switzerland. The samples were placed in cylindrical vanadium cans with 6-8 mm diameter. The measurements were performed in the angular range of $4.6 - 164.9^\circ$ with a step size of $0.1-0.05^\circ$.

2.3.3. Structural and microstructural analysis from powder diffraction data by using the Rietveld method

In the present work The Rietveld method (also denoted to as Rietveld refinement) was employed to obtain accurate values of atomic positions, lattice constants, anionic site occupation factors, displacement parameters of novel oxynitrides (Chapters 3-5) as well as to determine particle size and strain of the oxides and the oxynitrides (Chapter 5) from the neutron- and x-ray powder diffraction spectra. The principle of the method is described below.

2.3.3.1. Theoretical background

The intensity measured during the x-ray or neutron diffraction experiments can be modeled. The calculated intensity at i^{th} step is equal to:

$$y_{ci} = s \sum_K L_K |F_K|^2 \phi(2\Theta_i - 2\Theta_k) P_K A + y_{bi} \quad (2.4)$$

where

s is the scale factor,

K represents the Miller indices, $h k l$, for a Bragg reflection,

L_K contains the Lorentz, polarization and multiplicity factors,

ϕ is the reflection profile function,

P_K is the preferred orientation function,

A is the absorption factor,

F_K is the structure factor for the K^{th} Bragg reflection,

y_{bi} is the background intensity at the i^{th} step,

Θ_i is the scattering angle,

Θ_k is the Bragg angle.

The Rietveld method consists of refining a crystal structure by minimizing the weighted squared difference between the observed and the calculated pattern against the parameter vector β :

$$S^2 = \sum_{i=1}^n \omega_i (y_i - y_{ci}(\beta))^2 \quad (2.5)$$

$$\omega_i = \frac{1}{\sigma_i^2} \quad (2.6)$$

where

y_i is the observed intensity,

ω_i is the variance of the i^{th} observation,

σ_i is the standard deviation of the i^{th} observation

The necessary condition for S^2 to reach the minimum is:

$$\frac{\partial(S^2)}{\partial\beta} = \mathbf{0} \quad (2.7)$$

The starting values β_0 for the refined parameters β are normally known from the structure solution step. A Taylor expansion of $y_{ci}(\beta)$ around β_0 allows applying an iterative process. The shifts applied to the parameters at each cycle for improving S^2 are calculated by solving a linear system of equations:

$$A\delta_{\beta_0} = b \quad (2.8)$$

where

the elements of the A and the b matrixes are expressed as follows:

$$A_{kl} = \sum_i \omega_i \frac{\partial y_{ic}(\beta_0)}{\partial \beta_k} \frac{\partial y_{ic}(\beta_0)}{\partial \beta_l} \quad (2.9)$$

$$b_k = \sum_i \omega_i (y_i - y_{ic}) \frac{\partial y_{ic}(\beta_0)}{\partial \beta_k} \quad (2.10)$$

The shifts of the parameters obtained by solving the system of equations are added to the starting parameters:

$$\beta_1 = \beta_0 + \delta_{\beta_0} \quad (2.11)$$

The new parameters are considered as starting ones for the next cycle. The procedure is repeated until the criterion of the convergence is satisfied.

Thus, the Rietveld method provides values of structural and microstructural parameters which correspond to the local minimum of S^2 .

The variance of the adjusted parameters $\sigma(\beta_k)$ is calculated from the expression:

$$\sigma^2(\beta_k) = (A^{-1})_{kk} S^2 \quad (2.12)$$

where

$$\chi^2 = \frac{S^2}{N - P} \quad (2.13)$$

where

N is the number of independent observations,

P is the number of least-squares parameters

The quality of the refinement is evaluated from the fit quality indicators (so-called, R-factors), calculated for the regions, where the Bragg reflections contribute to the diffraction pattern:

$$R_p = \frac{\sum_i |y_i - y_{ic}|}{y_i} \times 100\% \text{ (R-pattern)} \quad (2.14)$$

$$R_{wp} = \left\{ \frac{\sum_i w_i (y_i - y_{ic})^2}{\sum_i w_i y_i^2} \right\}^{1/2} \times 100\% \text{ (R-weighted pattern)} \quad (2.15)$$

$$R_{\text{exp}} = \left\{ \frac{(N - P + C)}{\sum_i w_i y_i^2} \right\}^{1/2} \times 100\% \text{ (R-expected)} \quad (2.16)$$

$$\chi^2 = \left(\frac{R_{wp}}{R_{\text{exp}}} \right)^2 \text{ (reduced Chi-square)} \quad (2.17)$$

The acceptable values for the refinements R-factors, which will be presented in the following chapters are the following: $R_p < 0.15$, R_{wp} (wR_p) < 0.2 [98-100].

2.3.3.2. Structural information

The structure factor can be expressed as:

$$F_K = \sum_{j=1}^n g_j f_j \exp[2\pi i(hx_j + ky_j + lz_j)] \exp\left(-8\pi^2 \bar{u}_j^2 \frac{\sin^2 \Theta}{\lambda^2}\right) \quad (2.18)$$

Thus, it contains information about atomic coordinates (xyz), their deviation from the equilibrium position (\bar{u}^2) and occupation (g). The Rietveld method allows accurate refinement of these parameters.

2.3.3.3. Microstructural information

The microstructural effects were treated using the Voight approximation [101]: both instrumental and sample intrinsic profiles were supposed to be approximately described by a convolution of Lorentzian and Gaussian components. The Thompson-Cox-Hastings (TCH) pseudo-Voight (pV) profile function was used to mimic the exact Voight function:

$$pV(x) = \eta L(x) + (1 - \eta)G(x) \quad (2.19)$$

$$pV(x) = pV(\Theta, \eta, H) \quad (2.20)$$

where

$L(x)$ – Lorentzian function,

$G(x)$ – Gaussian function,

η – mixing parameter,

H – full width of the reflection at half maximum (FWHM).

The microstructural information (particles size, strain) was obtained according to the following procedure:

1. Lorentzian and Gaussian components of the reflections full widths at half maximum (FWHM) were modeled according to Thomson-Cox-Hastings (TCH):

$$H_G^2 = (U + U_s) \tan^2 \Theta + V \tan \Theta + W + P_s / \cos^2 \Theta \quad (2.21)$$

$$H_L = (X + X_s) \tan \Theta + (Y + Y_s) / \cos \Theta \quad (2.22)$$

2. Coefficients U , V , W , X , Y , which determine an instrument resolution function, were refined from the XRPD data of the NIST standard reference material SRM 660, LaB₆.
3. The sample related coefficients U_s , P_s , X_s and Y_s were refined from the XRPD data of the investigated material. The refinement was performed using the instrument resolution file based on the predetermined U , V , W , X , Y coefficients.
4. H_i and η_i (where i stands for size and strain) were calculated from TCH equations:

$$H_i^5 = (H_{Gi}^5 + 2.69 H_{Gi}^4 H_{Li} + 2.43 H_{Gi}^3 H_{Li}^2 + 4.47 H_{Gi}^2 H_{Li}^3 + 0.08 H_{Gi} H_{Li}^4 + H_{Li}^5) \quad (2.23)$$

$$\eta_i = 1.36603 \frac{H_{Li}}{H_i} - 0.47719 \left(\frac{H_{Li}}{H_i} \right)^2 + 0.11116 \left(\frac{H_{Li}}{H_i} \right)^3 \quad (2.24)$$

5. Size-strain related integral breadth (β_i) of the reflection, was calculated from the formula:

$$\beta_i = \frac{1}{pV(0)} = \frac{\pi H_i / 2}{\eta_i + (1 - \eta_i) \sqrt{\pi \ln 2}} \quad (2.25)$$

6. The obtained β_i values were used for the average volume weighted particles size ($\langle D \rangle_v$) and maximum strain (ϵ) values calculation:

$$\langle D \rangle_v = \frac{\lambda}{\beta_{size} \cos \Theta} \quad (\text{Scherrer formula}) \quad (2.26)$$

$$e = \frac{1}{4} \beta_{strain} \cot \Theta \quad (2.27)$$

All the refinements were done by using the software *Fullprof* [102].

2.3.4. Transmission electron microscopy

Electron diffraction and high resolution studies were done by transmission electron microscopy (TEM) using a Philips CM30 microscope operating at 300 kV. Double-tilt sample holders were used for copper grids with the product powders. Diffraction simulations were performed using software JEMS [103].

2.4. Composition and microstructure studies

The anionic composition of the synthesized oxynitrides was studied with thermal analysis methods (hotgas-extraction and thermogravimetric analysis, TGA) as well as with neutron diffraction and Elastic recoil detection analysis (ERDA). The cationic composition was studied with Rutherford backscattering spectrometry (RBS) and energy dispersive x-ray spectrometry (EDX).

2.4.1. Hotgas-extraction

Since the properties of oxynitrides are sensitive to their nitrogen content, correct determination of the anionic composition is highly important. The most commonly used thermal methods for the O/N content determination are hotgas-extraction and thermogravimetric analysis (TGA).

In this work the hotgas-extraction experiments were performed using a LECO TC500 analyzer (Fig. 2.6). It uses an electrode furnace capable of producing high electrical current to heat the sample material.

Nitrogen is measured by thermal conductivity and oxygen is measured by infrared radiation.

Analysis begins by placing an empty graphite crucible (sealed and purged of atmosphere) between two electrodes in the furnace. High current passes through the crucible generating

high heat ($T \sim 573 \text{ K}$), which drives off gases trapped in the graphite (out-gassing). Then, the sample is dropped from the loading mechanism into the crucible. High current ($T \sim 3273 \text{ K}$) is passed through the crucible again driving off gases released from the sample.

The oxygen from the sample combines with carbon from the crucible to form carbon monoxide (CO). Sample gases then pass through heated rare earth copper oxide, which converts CO to CO_2 . The sample gases then pass through the infrared cell, which measures the oxygen as carbon dioxide. Then, CO_2 is removed by an absorber (Lecosorb). The gasses pass through the thermal conductivity cell which detects nitrogen.

The analyzer is calibrated with SiO_2 and SiN standards.



Figure 2.6. LECO TC500 analyzer.

The advantage of the hotgas-extraction is the promptness of the analysis: it only takes about 3 minutes to measure the O/N content of a sample. This method also allows simultaneous determination of oxygen and nitrogen contents.

2.4.2. Thermogravimetric (TGA) and Differential Thermal (DTA) analysis

Thermogravimetric analysis (TGA) is a technique used to determine the change of the sample weight in relation to the programmed change in temperature or time. The changes of the sample weight are accompanied by the adsorption or evolution of various gases. The

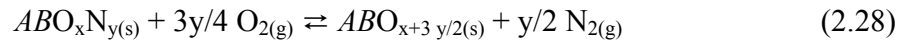
gases can be identified by means of mass spectrometry (MS). The method employs fragmentation of gas molecules into ions and measuring their mass-to-charge ratio.

Exothermic or endothermic changes in the sample can be detected by differential thermal analysis (DTA). This technique measures the temperature difference between the sample and the reference as a function of the reference sample temperature or time.

In the present work TGA/DTA/MS were used to study the decomposition of the soft chemistry precursors (synthetic air), the thermal stability (He, Ar, N₂) and the thermal reoxidation (synthetic air) of the oxynitrides and to determine the nitrogen content of the oxynitrides (Chapters 3 and 4).

These studies were performed in the temperature range of 300 K <T< 1673 K using a NETZSCH STA 409CD thermobalance coupled by a heated quartz capillary to an 409C Aeolos Quadrupol Mass Spectrometer (MS). Heating rates of 2 K min⁻¹, 5 K min⁻¹ and 10 K min⁻¹ and a gas flow of 50 mL min⁻¹ were used. The studies were done using Al₂O₃ crucibles. Purity of all the gases used in thermal gravimetric analysis was ≥ 99.9999 %.

The *d*⁰-perovskite-type oxynitrides reoxidize upon heating them in synthetic air according to the equation:



The reoxidation leads to *d*⁰-oxides as identified by x-ray diffraction.

The amount of evolved nitrogen can be determined from the weight gain (Δm), measured during the reoxidation experiment.

From that value nitrogen stoichiometry (*y*) can be calculated:

$$y = \left(\frac{\Delta m}{\frac{3}{2} M(O_2) - M(N_2)} \right) \times \frac{M(ABO_{x+3y/2})}{m(ABO_{x+3y/2})} \quad (2.29)$$

where

$M(N_2)$ – molar mass of molecular nitrogen,

$M(O_2)$ – molar mass of molecular oxygen,

$M(ABO_{x+3y/2})$ – molar mass of the formed oxide,

$m(ABO_{x+3y/2})$ – mass of the formed oxide.

2.4.3. Neutron diffraction

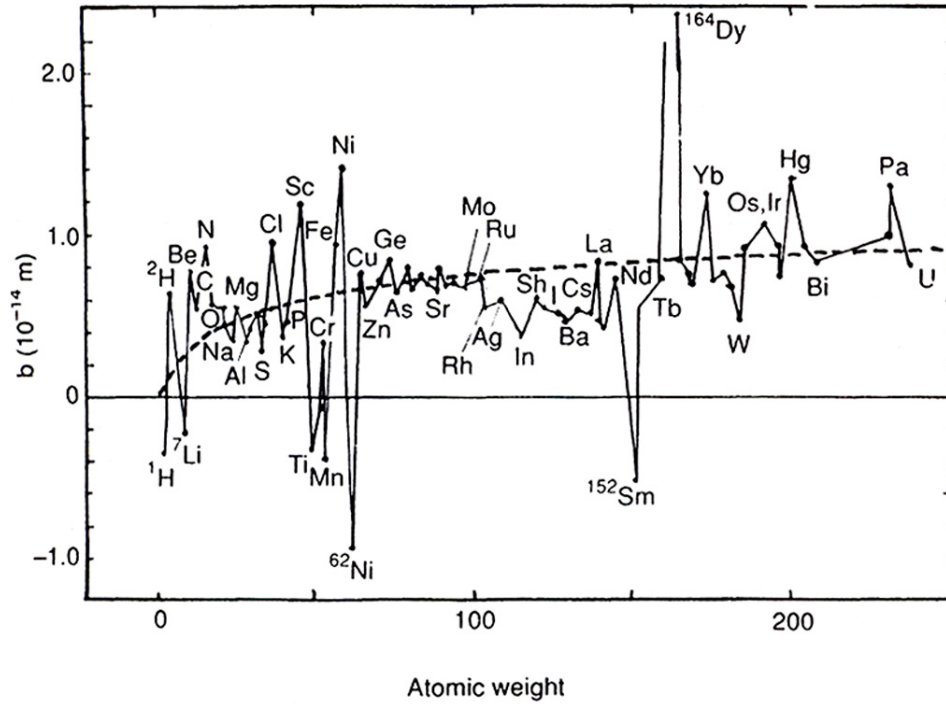


Figure 2.7. The dependence of the neutron scattering length from the atomic number.

Additionally to the thermal analysis methods neutron diffraction was employed to study the anionic composition of the synthesized oxynitrides. This technique offers 2 particular advantages over the thermal analysis methods:

1. It allows the selective O/N content determination in a particular bulk phase of the multicomponent mixture, *i.e.* the result is not affected by the presence of impurities.
2. It allows to study the anionic distribution over available crystallographic sites.

Neutrons as uncharged particles interact with the atomic nuclei. The radius of atomic nuclei $r_N < 10^{-14}$ m is much smaller than the wavelength of thermal neutrons. Therefore, the

nuclei act as a point scatterer for thermal neutrons, *e.g.* its scattering amplitude does not vary with the scattering angle θ . Hence, the scattered wave function for neutrons (ψ_n) is:

$$\psi_n = \left(\frac{-b}{r_p} \right) \exp[-ik_1 \cdot r_p] \quad (2.30)$$

where

k_p is the scattered wave vector,

r_p is the position of the wave front,

b is the neutron scattering length.

The neutron scattering length is measured in barns (1 barn = 10^{-15} m) and it is related with the atomic weight (A) of an element through the following equation:

$$b = 15A^{1/3} \quad (2.31)$$

While the general $A^{1/3}$ dependence of b is observed due to the resonant absorption in compounds nucleus, b does not vary gradually with $A^{1/3}$ (Fig. 2.7). This offers the possibility to distinguish between the closely located atomic elements such as oxygen and nitrogen. Indeed, the neutron scattering length for nitrogen (9.36 barns) strongly differs from that of oxygen (5.803 barns).

2.4.4. Scanning electron microscopy and energy dispersive analysis

Microstructure studies were performed using a LEO JSM-6300F scanning electron microscope. The cationic composition was studied by energy dispersive x-ray spectrometry (EDX-Link Pentafet 5947, from Oxford Microanalysis).

2.4.5. Measurements of the specific surface area

The surface area of the starting oxides and the produced oxynitride samples was measured by the BET method using a Chembet-3000 system (Quantachrome instruments). The

measurement is based on the physical adsorption of inert gas molecules on a surface of the material. The BET adsorption isotherm equation is the following:

$$\frac{1}{v} \left[\left(\frac{P}{P_o} \right) - 1 \right] = \left(c - \frac{1}{v_m c} \right) \left(\frac{P}{P_o} \right) + \frac{1}{v_m c} \quad (2.32)$$

where

v – quantity of the adsorbed gas,

v_m – volume of the adsorbed gas (it corresponds to the volume, which is required to cover all surface with layer of a unimolecular thickness),

P – equilibrium pressure of the adsorbed gas at the adsorption temperature,

P_o – saturation pressure of the adsorbed gas at the adsorption temperature,

c – BET constant:

$$c = \exp \left[E_1 - \frac{E_L}{RT} \right] \quad (2.33)$$

where

E_1 – heat of adsorption for the first layer,

E_L – heat of adsorption for the second and higher layers,

R – gas constant (8.314 J mol⁻¹ K⁻¹),

T – temperature (in K).

The BET isotherm can be plotted as $\frac{P_o}{P}$ vs. $\frac{1}{v} \left[\left(\frac{P}{P_o} \right) - 1 \right]$. The linearity of the plot is

maintained only at low pressures ($0.05 < \frac{P}{P_o} < 0.35$). Its slope and the intercept with y -axis were used to calculate v_m and c . From the values obtained, the specific surface area S was calculated as:

$$S = \frac{v_m N_A s}{Mm} \quad (2.34)$$

where

N_A – is Avogadro's number,

s – adsorption cross-section,

M – molecular weight of the adsorbed gas,

m – is the sample weight.

2.5. Photocatalytic activity

In the present work we report on the photocatalytic performance of LaNbON₂ (Chapter 4). In many cases noble metal (Au, Pt) impregnation allows to improve the performance of the photocatalyst [29]. Therefore, we additionally studied the photocatalytic performance of the Pt-impregnated LaNbON₂ (Chapter 4).

2.5.1. Platinum impregnation

The Pt-impregnation was carried out as follows. 5 mg tetraamineplatinum (II) nitrate, Pt(NH₃)₄(NO₃)₂ (Alfa Aesar, CAS 20634-12-2), was dissolved in 1 ml deionized water. The solution was slowly poured into a 250 mL flask containing a suspension of LaNbO₄/LaNbON₂/TiO₂ (495 mg) in deionized water (10 mL). The suspension was kept at room temperature for 24 hours under a constant stirring. Then, water was removed by heating the suspension at T = 318 K under vacuum in a rotavapor. The platinum reduction was carried out at T = 623 K in a tubular furnace using a 10 vol % H₂ mixture with He. The gas flow was set to 40 mL min⁻¹. The time of reduction was 80 minutes.

2.5.2. Photocatalytic water decomposition

Photocatalytic water splitting was carried out at the University of Milano (in collaboration with Prof. Milena Selli). A typical reaction solution placed in the photochemical reaction vessel comprised 43 ml of methanol (6 vol. %) aqueous solution, containing 14 mg of the analyzed powder (catalyst). Before starting the reaction the solution was placed in an

ultrasound bath for 10 minutes for the dispersion of the catalyst. Either an iron halogenide mercury arc medium pressure 250 W lamp (Jelosil HG 200), emitting mainly in the 320–400 nm range (UV-region), or an Osram Powerstar HCl1-T Neutral White 150W lamp (Visible-region), mounted on a Twin Beam support, emitting at the 340-450 nm range, were employed as irradiation sources. Concentrations of the evolved H₂ and O₂ were determined by means of gas chromatography. The photocatalytic activity of the oxynitrides was compared with that of known photocatalysts such as TiO₂ (Degussa P25 with $s = 50 \text{ m}^2 \text{ g}^{-1}$) and SrTiO₃ (FP, $s = 107 \text{ m}^2 \text{ g}^{-1}$).

2.6. Spectroscopic characterization

2.6.1. UV-Vis diffuse reflectance spectroscopy

Optical properties of the polycrystalline powders were investigated by UV-Vis diffuse reflectance spectroscopy. Reflectance data were collected with a Varian Cary 500 Scan UV-Vis-NIR scanning double-beam spectrometer equipped with a 150mm Labsphere DRA-CA-50 integrating sphere over the spectral range of 250–2000 nm (0.6–5 eV). The measured reflectance (R) was transformed into the Kubelka-Munk (KM) function $F(R)$:

$$F(R) = \frac{(1-R)^2}{2R} = \frac{K}{S} \quad (2.35)$$

where

K is the absorption coefficient and

S is the scattering coefficient.

In the linear region, where a steep increase in the KM function is observed the Tauc equation can be applied:

$$K \cdot h\nu = B \cdot (h\nu - E_{g,opt})^n \quad (2.36)$$

where

h is the Planck's constant ($6.62606896(33) \cdot 10^{-34}$ J s or $4.13566733(10) \cdot 10^{-15}$ eV s),

B is the constant,

$E_{g:opt}$ is the optical band gap value,

ν is the frequency of the electromagnetic wave:

$$\nu = \frac{c}{\lambda} \quad (2.37)$$

where

c – velocity of light in vacuum ($2.9979 \cdot 10^8$ m s⁻¹),

λ – wavelength.

The equation can be transformed into:

$$\left(\frac{K \cdot h\nu}{B} \right) = h\nu - E_{g:opt} = (F(R) \cdot h\nu)^2 \quad (2.38)$$

The further evaluation of the band gap was carried out according to Davis-Mott [104] and Shapiro's [105] methods. According to the Davis-Mott method the graph of $(F(R) \cdot h\nu)^2$ vs. E (in eV) was plotted. The region, where a steep increase in the plotted function is observed, was fitted with a linear function, which intersection with the energy axis was considered as the value for the band gap.

The Shapiro's method of the optical band gap determination is based on extrapolating the onset of the absorption to the wavelength axis.

2.6.2. Raman and infrared spectroscopy

Raman and infrared spectroscopy were used to monitor the presence of the carbonate and reoxidation intermediate impurities in the oxynitrides as explained in Chapter 3.

Raman spectroscopic studies were performed using a He-Ne laser, which emits at 632.8 nm in a single mode (Renishaw NIR 780TF series).

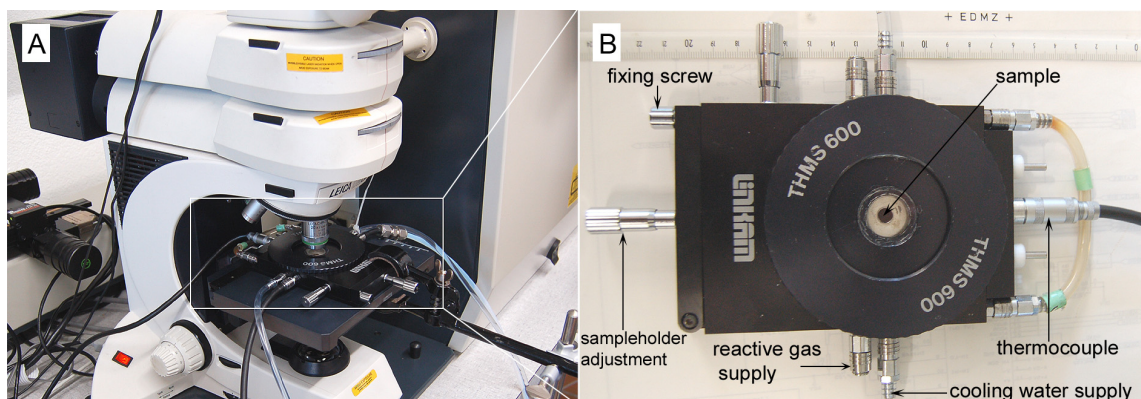


Figure 2.8. The scheme of the setup used for the Raman spectroscopic investigations: A. A general view. B. A close view on the employed measurement cell.

Infrared spectra (IR) from all samples were recorded in the $650 - 4000 \text{ cm}^{-1}$ region using a Fourier Transform – Infrared Spectrometer BIO RAD FTS 175C (Fig. 2.8).

Raman and infrared spectroscopic studies of strongly absorbing samples were performed under the flowing inert gas to prevent the samples from reoxidation, which can be induced by laser heating.

2.6.3. Extended X-ray absorption spectroscopy

XANES measurements at the Mo *K*-edge were performed at the beamline CEMO at the Hamburger Synchrotron Radiation Laboratory, HASYLAB, Germany. Data were collected in the transmission mode. The energy scale was calibrated from the first inflection point in the *K*-edge of Mo metal (19.999 KeV), which was measured simultaneously as reference. The beamline was equipped with a double-crystal fixed exit monochromator with Si (311) crystal pairs. Signal intensities were detuned to 40% of their maximum levels to minimize contributions of higher harmonics. Spectra were acquired in 2 eV increments for the pre-edge region (19.80 - 19.98 KeV) and 0.20 eV near the edge (19.98 - 20.03 KeV). SrMoO_3 and SrMoO_4 were measured as standards for Mo^{4+} and Mo^{6+} respectively. The software package WinXAS v3.1 was used for data analysis [106].

2.7. Physical properties

2.7.1. Magnetic susceptibility

Magnetic susceptibility measurements were performed on pressed powder samples in the temperature range of $T = 5 \text{ K}-300 \text{ K}$ and in a magnetic field range of $-5 \text{ T}-+5 \text{ T}$ using a vibrating sample magnetometer VSM (Quantum Design PPMS,) and SQUID (Quantum design MPMS). For the VSM measurements brass half tube sample holders and plastic cylinders, which give together a negligible magnetic signal of order $10^{-8} \text{ emu T}^{-1}$, were used. The sample was centered on the sample holder using a Quantum Design supplied centering device, then slightly pressed from both sides with plastic cylinders of low magnetic susceptibility and finally sealed using a weakly magnetic varnish. The varnish possesses magnetic susceptibility of $-8.02 \cdot 10^{-9} \text{ emu Oe}^{-1} \text{ mol}^{-1}$ as determined from the separate measurement. Obtained field cooled (FC) and zero field cooled (ZFC) magnetization values were recalculated to the molar magnetic susceptibility values using following equation:

$$\chi = \frac{M}{T \times n} \quad (2.39)$$

where

χ – molar magnetic susceptibility,

M – magnetization (in emu),

T – magnetic field (in Oe),

n – amount of the measured material (mole).

Obtained susceptibility values were corrected for the signal coming from the varnish, shape factor and ionic core diamagnetism.

2.7.2. Electronic transport measurements

Electrical transport measurements were performed on bars with dimensions of $1.65 \text{ mm} \times 5-10 \text{ mm} \times 1 \text{ mm}$. The bars were obtained under an uniaxial pressure of 10 bar followed by

a cold isostatic pressing at 2000 bar. The bars were sintered at $T = 1073$ K for 30 min under flowing ammonia.

High temperature electrical conductivity (DC four-probe method) and Seebeck coefficient were measured simultaneously as a function of temperature in the temperature range of $340 \text{ K} < T < 950 \text{ K}$ using a RZ2001i measurement system from Ozawa science, Japan. Pt-contacts were used for these measurements.

In the temperature range of $5 \text{ K} < T < 300 \text{ K}$ the electrical resistivity was measured using a Quantum Design PPMS. Electrical contacts used for the measurements were made of Ag-containing double composite epoxy. Contacts to the measurement Puck were performed using Au-wires and In-solder. Before the measurements, the epoxy was dried under inert gas atmosphere at $T = 373$ K during 2 hours.

The measured resistance was recalculated to conductivity using the following formula:

$$\sigma = \frac{l}{R \times S} \quad (2.40)$$

where

σ – electrical conductivity,

R – measured resistivity,

l – distance between the voltage probes,

S – area.

3. $\text{Ca}_{1-x}\text{La}_x\text{TiO}_{3-x}\text{N}_x$ ($x = 0 - 0.7$) oxynitrides

3.1. Synthesis and thermal stability

Oxide precursors for the ammonolysis were prepared by a modified Pechini method as explained in Chapter 2. Titanium (Alfa Aesar, 99.99%), $\text{La}(\text{NO}_3)_3 \cdot 6\text{H}_2\text{O}$ (Merck, >99.0%), $\text{Ca}(\text{NO}_3)_2 \cdot 4\text{H}_2\text{O}$ (Merck, >99.0%) and citric acid (Merck, >99%) were used as starting compounds.

Additionally, $\text{La}_2\text{Ti}_2\text{O}_7$ was prepared by the standard ceramic method using TiO_2 (Merck, >99%), La_2O_3 (Fluka, 99.99%) and $\text{Ca}(\text{NO}_3)_2 \cdot 4\text{H}_2\text{O}$ (Merck, >99.0%) (Chapter 2).

Powder x-ray diffraction confirmed the phase purity of $\text{La}_2\text{Ti}_2\text{O}_7$ produced by both methods (Figure 3.1A, D). Oxide precursors with $x = 1, 0.7, 0.5$ obtained at 873 K by soft chemistry were x-ray amorphous (Figure 3.1B), while reflexes of the perovskite-type structure were resolved for samples with $x = 0.3$ and 1.0 (Figure 3.1C). A TGA analysis of the precursor with $x = 1$ revealed a progressive weight loss of 4.5 % starting at about 1070 K, which is accompanied by the appearance of a peak with $m/z = 44$ in the corresponding MS spectra. This signal can be attributed to CO_2 evolution. XRPD confirmed the formation of crystalline $\text{La}_2\text{Ti}_2\text{O}_7$ after the TGA measurement (Figure 3.1D). Based on our TGA experiments and the earlier Infrared spectroscopic studies of Bocher *et. al* [94] the observed thermal behavior of the precursor is attributed to the decomposition of carbonates followed by the formation of the crystalline oxide phase [94, 107-109]. From the TGA study the composition of the amorphous precursor can formally be expressed with the formula $\text{La}_2\text{Ti}_2\text{O}_{6.4}(\text{CO}_3)_{0.6}$.

The compound $\text{La}_2\text{Ti}_2\text{O}_7$ has a perovskite-related crystal structure. It is a member of the family of oxides of general formula $A_nB_n\text{O}_{3n+2}$. Their crystal structure is derived from the simple perovskite structure ABO_3 by separating layers of corner-sharing BO_6 octahedra

along the (110) plane [110]. Therefore, they are often denoted to as “(110) layered perovskites”.

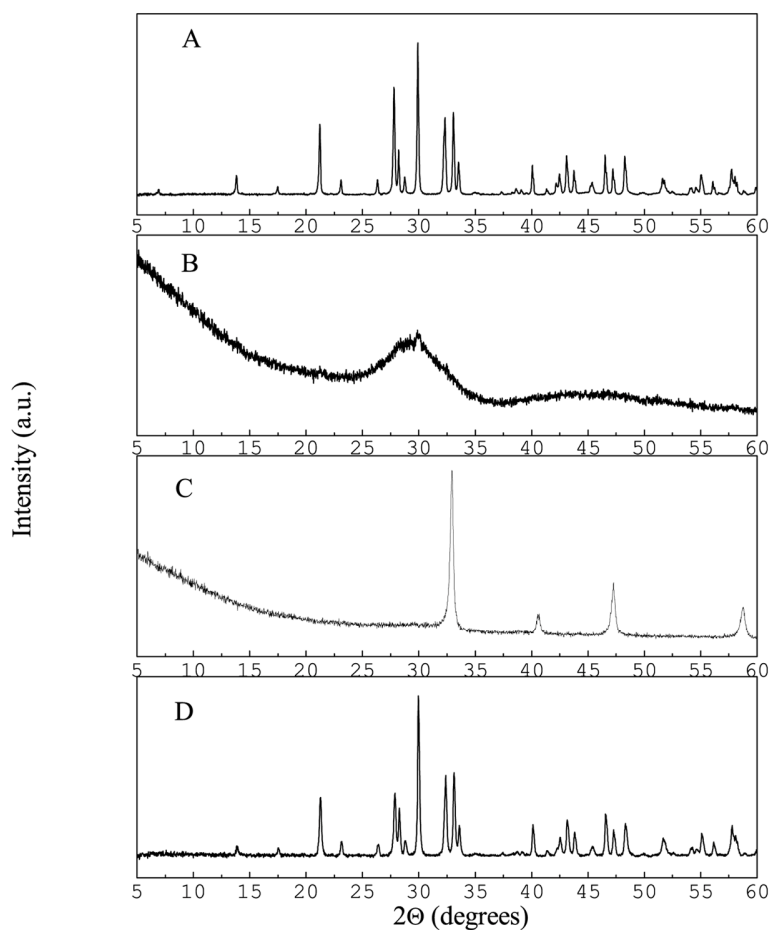


Figure 3.1. XRPD patterns of A. Ceramic precursor with $x = 1$, prepared at 1673 K; B. Precursor with $x = 1$, produced by the soft chemistry route and annealed at 873 K; C. Precursor with $x = 0.3$, produced by the soft chemistry route and annealed at 873 K; D. Precursor with $x = 1$, produced by the soft chemistry route and annealed at 1223 K in the TGA.

Table 3.1. Adjusted parameters of the ammonolysis and N/O content of the synthesized oxynitrides determined by hotgas-extraction

Composition	T, K	NH ₃ flow, mL min ⁻¹	Time, min	N content (hotgas)	O content (hotgas)
LaTiO ₂ N	1223	360	2020	0.96±0.05	2.16±0.05
La _{0.7} Ca _{0.3} TiO _{2.3} N _{0.7}	1123-1173	200	2835	0.76±0.01	2.22±0.02
La _{0.5} Ca _{0.5} TiO _{2.5} N _{0.5}	1073-1098	100	2850	0.58±0.02	2.54±0.04
La _{0.3} Ca _{0.7} TiO _{2.7} N _{0.3}	1073	100	1676	0.36±0.01	2.74±0.02

Ammonolysis was performed in a rotating cavity reactor. Air in the reactor was replaced by nitrogen (MESSER, 99.5%) by applying a nitrogen gas flow of 100 mL min⁻¹. Then the samples were heated until the reaction temperature was reached and nitrogen was exchanged for ammonia (PanGas, 99.98%). LaTiO₂N was synthesized at T = 1223 K. XRPD of all the Ca-containing oxides reacted at this temperature revealed considerable amounts of CaO and TiN impurities. Decreasing the reaction temperature ammonia flow, reaction time and using soft chemistry produced precursors allowed to decrease the amount of impurities. The adjusted reaction parameters of all the samples are collected in Table 3.1. After the reaction all the Ca-containing oxynitrides were cooled down to 473 K in ammonia gas flow and further to room temperature in nitrogen gas flow to remove unreacted ammonia gas. The cooling of LaTiO₂N (prepared from the standard ceramic route produced precursor) was performed either in ammonia or in nitrogen atmosphere. The quenching was performed after switching off the ammonia flow. Additionally, one of the LaTiO₂N samples was cooled in ammonia down to 1000 K. Then ammonia was changed for nitrogen and further cooling proceeded. These different cooling modes were applied to study the influence of the cooling procedure on the anionic content and surface composition of this material.

Thermal reoxidation studies reveal 3 stages during the transformation of the synthesized oxynitrides to the corresponding oxides (Fig. 3.2). The first stage corresponds to the temperature range of 300 K < T < 600 K. A very small weight loss (0-0.5 weight %) is observed in the TGA-signal. MS-signals of H₂O (m/z = 18), and CO₂ (m/z = 44) evolution are monitored in the same temperature region, which is concluded to be due to the release

of the surface adsorbed molecules. The second stage starts at temperatures higher than 600 K when a progressive weight gain is observed. It is accompanied by an exothermic signal in the DTA and a molecular nitrogen evolution signal ($m/z = 28$) in the MS spectra. Beside N_2 , a weak signal with $m/z = 30$ which is attributed to nitrogen monoxide NO is measured by MS. The phase which has formed decomposes further during the third stage, again with molecular nitrogen release. It can be concluded that this phase corresponds to the dinitrogen fragments containing intermediate [50, 68, 69, 73]. During its decomposition the weight loss is detected by TGA.

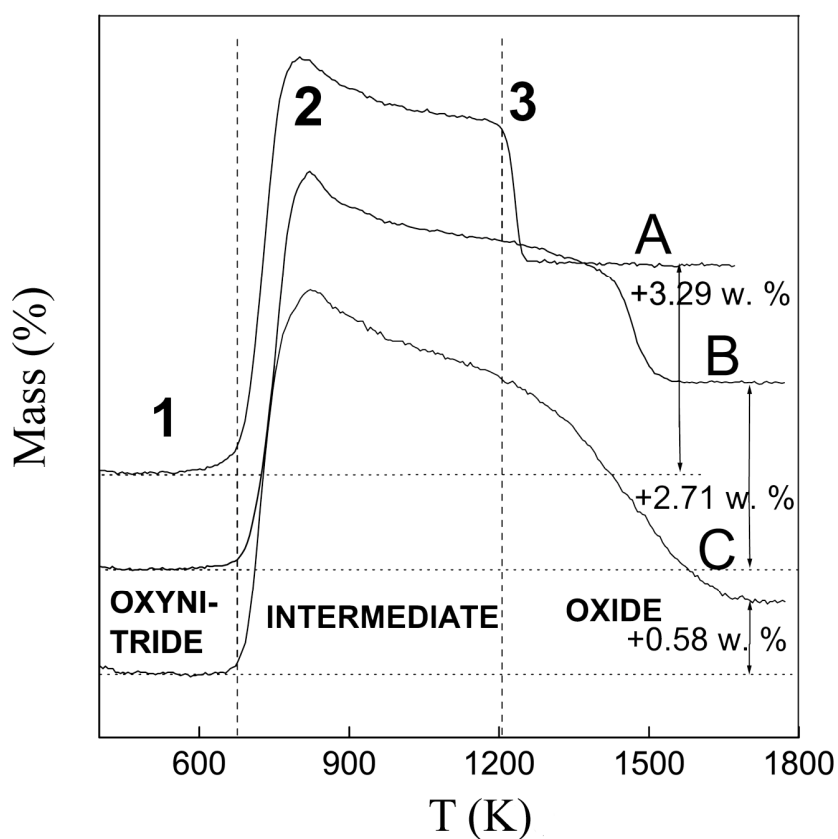


Figure 3.2. TGA of the reoxidation of: A. $LaTiO_2N$; B. $La_{0.7}Ca_{0.3}TiO_{2.3}N_{0.7}$; C. $La_{0.5}Ca_{0.5}TiO_{2.5}N_{0.5}$. Heating rate 2 K min^{-1} .

A difference in the decomposition rates of the intermediates during this third stage is observed. Thus the intermediate of the LaTiO_2N reoxidation process completely decomposes in the temperature interval of $1090 \text{ K} < T < 1223 \text{ K}$, when heating it with 2, 5 or 10 K min^{-1} . Its decomposition is accompanied by a sharp signal of molecular nitrogen emission in the MS spectrum (Fig. 3.3) and a small exothermic signal in the DTA curve. For the Ca containing samples broadening of the molecular nitrogen signal is observed (Fig. 3.3). The DTA signal, which should accompany this process, can't be resolved using the particular experiment arrangement. In the region of the intermediate decomposition the slope of the TGA graph decreases as the Ca content increases (Fig. 3.2). The observed differences in the thermal behavior of the intermediates indicate a decrease in the intermediates decomposition rate with increasing x.

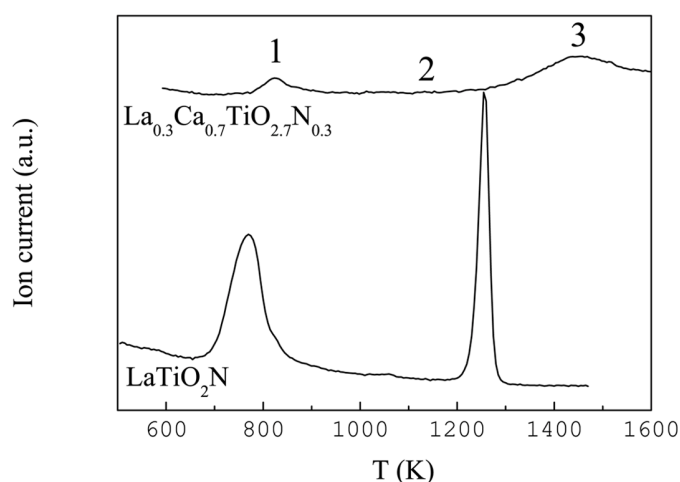


Figure 3.3. Molecular nitrogen in the MS spectra appeared during reoxidation of $\text{La}_{0.3}\text{Ca}_{0.7}\text{TiO}_{2.7}\text{N}_{0.3}$ and LaTiO_2N . Heating rate 10 K min^{-1} .

The intermediates of all the oxynitrides were isolated by quenching them from 873 K to 300 K with a cooling rate 40 K min^{-1} within the TGA. XRPD studies of the isolated samples reveal the formation of phases with the same crystallographic structure as for the parent oxynitrides but of lower crystallinity as broadening of the reflections is observed on the XRPD patterns.

XRPD analysis was also carried out on the completely reoxidized oxynitrides. The reaction product of the LaTiO_2N reoxidation was assigned to $\text{La}_2\text{Ti}_2\text{O}_7$ (2D, monoclinic). On the XRPD pattern of the reoxidized $\text{La}_{0.3}\text{Ca}_{0.7}\text{TiO}_{2.7}\text{N}_{0.3}$ only reflections, which can be attributed to a perovskite type phase were resolved. However at 2Θ region near 30° background slightly increases. This can be attributed to the second phase presence, which is x-ray amorphous. The perovskite type phase should be one that was previously reported [111]. It is represented by A-site deficient $\text{La}_{0.3}\text{Ca}_{0.7}\text{TiO}_3$ (mostly due to Lanthanum vacancies formation, when the oxygen content is close to 3.0). Thus the second phase should be Lanthanum enriched. For the other oxynitrides corresponding reoxidized samples were multiphase products. With increasing Ca content the decrease in the intensity of the perovskite phase assigned reflections was observed.

Apparently the main crystallographic changes occur during the third stage when the intermediate decomposes and the oxide phase is formed. Crystallographic studies confirm that for the $\text{La}_{0.3}\text{Ca}_{0.7}\text{TiO}_{2.7}\text{N}_{0.3}$ reoxidation intermediate the third stage proceeds without significant change in the crystallographic structure, whereas for other intermediates the structure changes partly or completely from 3D (simple perovskite) to 2D ((110) layered perovskite).

Recently thermodynamic aspects of the intermediates formation and decomposition were studied. It was shown by Tessier *et al.* [73] that the enthalpy of the transformation perovskite-layered perovskite comprises the main contribution to the value of enthalpy drop during the intermediate decomposition. From our observations it can be concluded that changes in the crystallographic structure influence also the kinetics of the intermediates decomposition.

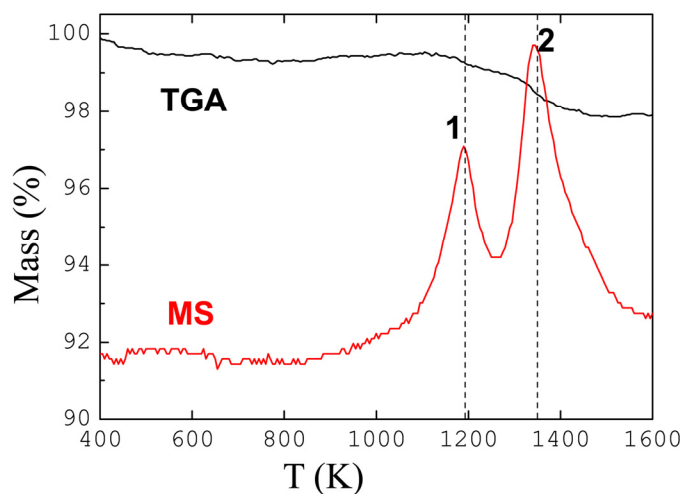


Figure 3.4. TGA-MS of the LaTiO_2N two step decomposition in He. Heating rate 10 K min^{-1} . MS signal corresponds to N_2 evolution ($m/z=28$).

Thermal stability studies in helium atmosphere (Fig. 3.4) reveal a decomposition of all the studied oxynitrides. A weight loss was detected starting at a temperature near 1073 K and finished near 1373 K. Only a molecular nitrogen signal ($m/z = 28$) was detected by means of mass spectrometry during both steps (Fig. 3.4). Changing the atmosphere for nitrogen doesn't suppress the decomposition. Phase analysis using XRPD was performed on the decomposed phases. For LaTiO_2N and $\text{La}_{0.7}\text{Ca}_{0.3}\text{TiO}_{2.3}\text{N}_{0.3}$ it reveals the formation of La_2O_3 and TiN together with a perovskite-type phase of unknown composition. The thermal treatment of $\text{La}_{0.3}\text{Ca}_{0.7}\text{TiO}_{2.7}\text{N}_{0.3}$ and $\text{La}_{0.5}\text{Ca}_{0.5}\text{TiO}_{2.5}\text{N}_{0.5}$ results in a mixture of TiN and the perovskite-type phase.

3.2. Structure

The x-ray diffraction powder pattern of LaTiO_2N formed after the ammonolysis of both ceramic and soft chemistry produced precursors can be indexed using a cubic perovskite unit cell. However, since the atomic scattering factors of O^{2-} and N^{3-} are close and significantly lower than those for La^{3+} and Ti^{4+} , the collected data cannot provide sufficient information for the correct space group assignment. In fact, neutron diffraction reveals the

presence of supercell reflections, corresponding to the unit cell with $a \approx \sqrt{2} * a_p$, $b \approx 2 * a_p$, $c \approx \sqrt{2} * a_p$ (where a_p is denoted to the cubic perovskite lattice parameter). Further neutron data refinements in the profile matching mode reveal that the unit cell is at least orthorhombically distorted and possibly *I*- or *C*-centered. Examination of the Rietveld fits quality of *I*- and *C*- centered orthorhombic, monoclinic and triclinic models derived for perovskites ended up with two possible structural models, *Imma* ($wR_p = 8.19$, $R_p = 8.15$, $\chi^2 = 2.46$) and $I\bar{1}$ ($wR_p = 7.99$, $R_p = 7.85$, $\chi^2 = 2.48$). Since, in the present case the material has very close values for two of its lattice parameters ($a \approx c$) and a size-strain reflections broadening often measured for oxynitrides [65], a care should be taken when choosing between two structural models with close Rietveld refinement statistics.

Since the electron atomic scattering amplitude is $f_e \sim Z^{1/3}$ (where Z = atomic number), light elements like oxygen/nitrogen scatter electrons more strongly than x-rays. Hence, electron diffraction is a well suited technique to study pseudosymmetry in perovskites. Space groups *Imma* and $I\bar{1}$ have different reflection conditions. Thus, they can be distinguished by electron diffraction. Moreover, ED can reveal important microstructural features of the compound and deviations from the ideal structure, which can not be detected by x-ray or neutron diffraction techniques.

According to the lattice parameters settings used by Howard *et al.* [4, 112] *Imma* can be related to $I\bar{1}$ by the matrix:

$$\begin{pmatrix} 1/2 & 1/2 & 1 \\ 1/2 & -1/2 & 0 \\ 1/2 & 1/2 & -1 \end{pmatrix}$$

The reflection condition ($hk0$): $h = 2n$ does not allow the reflection $\{110\}$, which belongs to the zone axis $[001]/[111]/[112]$, to appear in the S.G. *Imma*. This reflection corresponds to the reflection $\{011\}$ allowed in the S.G. $I\bar{1}$.

Electron diffraction images (Figure 3.5) taken from the LaTiO_2N sample confirmed the absence of the extinctions characteristic for the S.G. $Imma$, which confirms that the true space group, describing the average crystal structure of LaTiO_2N , is $I\bar{1}$.

Further TEM examination of the material indicated the presence of twin-domains of different types and orientations. Some examples of such domains are given in Figure 3.6A, B. The presence of domains can be explained by the small mismatch in the values of the lattice parameters a and c (0.06 %) and the fact that $c^2 \approx a^2 + b^2$. It confirms structural transition(s) for LaTiO_2N , which occur(s) in the temperature region of $T = 1223 - 298$ K. Beside twin domains, incommensurate superstructure reflections were observed in some of the ED patterns (Figure 3.6C). This confirms the presence of some intermediate phase of different symmetry than $I\bar{1}$ at room temperature.

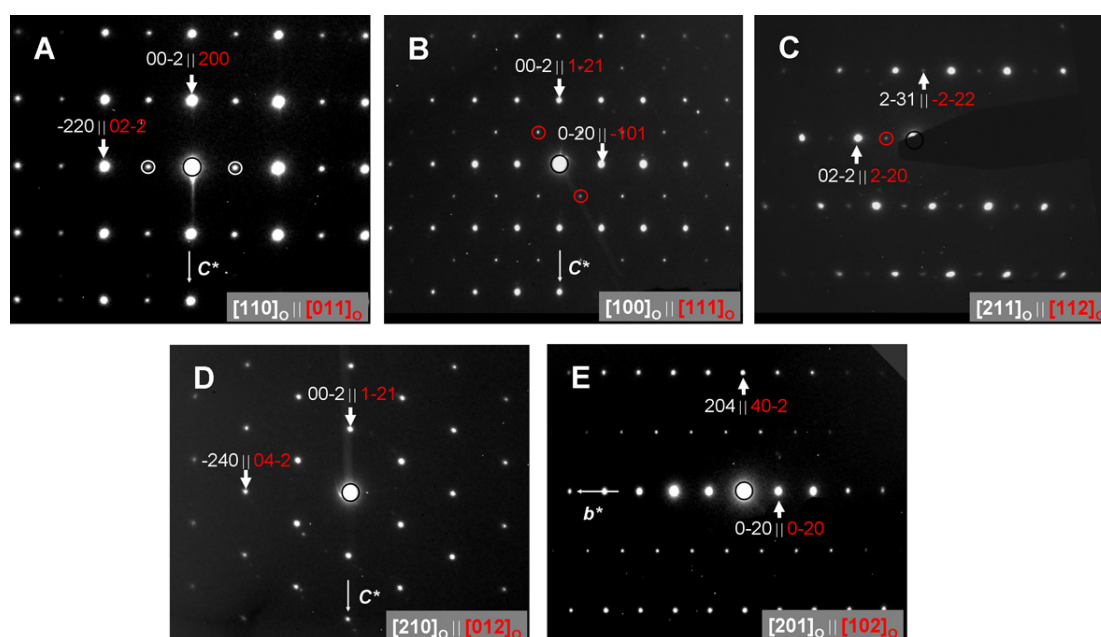


Figure 3.5. Electron diffraction patterns of LaTiO_2N taken along the A. $[100] \parallel [111]$; B. $[110] \parallel [011]$; C. $[210] \parallel [012]$; D. $[201] \parallel [102]$, E. $[211] \parallel [112]$ orthorhombic zone axis. Red and white colors are used to distinguish between similar zone axes. Reflections forbidden in the S.G. $Imma$ are marked with circles.

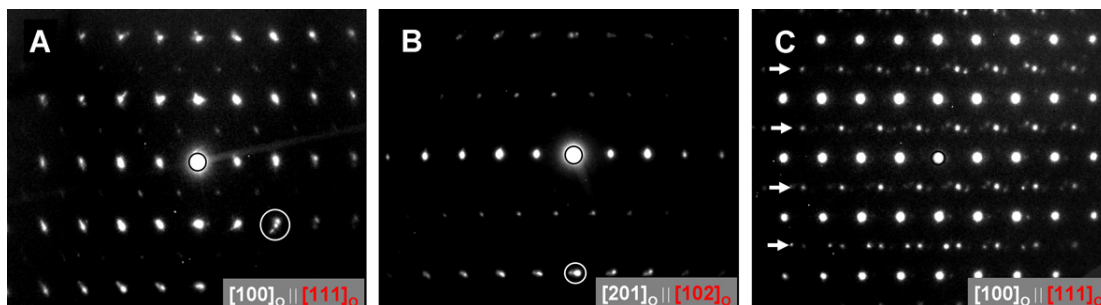


Figure 3.6. Electron diffraction patterns showing microstructural features of LaTiO₂N. A. Rotation twin-domains formed along $[100]_o \parallel [111]_o$ orthorhombic zone axis; B. Rotation twin-domains formed along $[201]_o \parallel [102]_o$ orthorhombic zone axis (characteristic reflections splitting is marked with circles); C. Incommensurate superstructure reflections along $[100]_o \parallel [111]_o$ orthorhombic zone axis (rows with the superstructure reflections are marked with arrows).

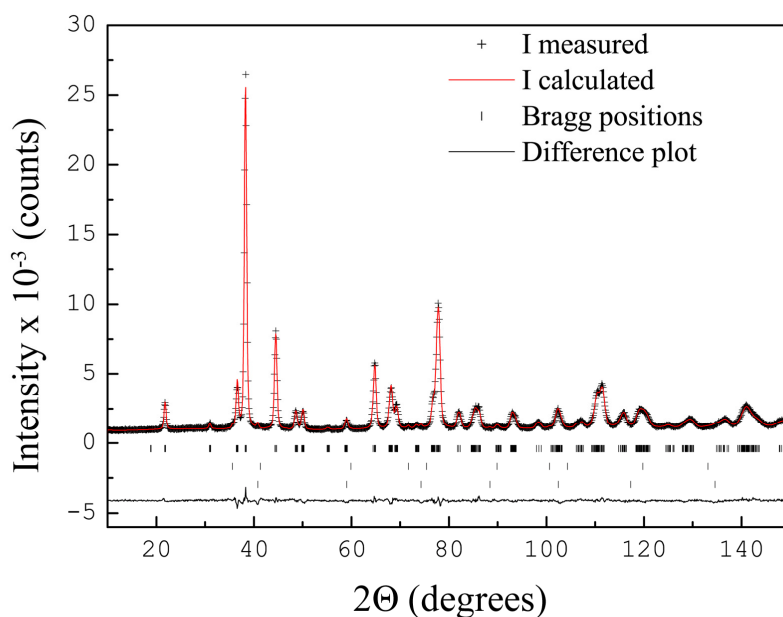


Figure 3.7. Rietveld refinement plot of the neutron powder diffraction data for the ammonia cooled LaTiO₂N, prepared from the soft chemistry produced precursor. Space group: $I\bar{1}$. The observed intensities, calculated profile, difference curve and Bragg positions are shown. TiN (second row of ticks below the graph) has been included as a minor impurity phase in the refinement, as well as vanadium (the container material).

The refinement of the neutron data against the $I\bar{1}$ model (Figure 3.7) converged with reliable fit characteristics ($wR_p = 9.76$, $R_p = 10.6$, $\chi^2 = 1.69$ for the oxynitride sample synthesized from the soft chemistry produced precursor and $wR_p = 7.99$, $R_p = 7.85$, $\chi^2 = 2.48$ for the oxynitride sample obtained from the standard ceramic route synthesized precursor).

The summary of the refinements against $I\bar{1}$ space group for the ceramic precursor synthesized LaTiO_2N is given in Table 3.2. As it can be seen a significant degree of the O/N ordering occurs in the oxynitride sample prepared from the ceramic precursor. Nitrogen tends to occupy one of the available 4i sites preferably. Within the estimated standard deviation (ESD) the same degree of the O/N ordering was found for both the samples. Hence, the starting precursor preparation route has barely any influence on the degree of the O/N ordering of LaTiO_2N .

The refinement of O/N occupancies leads to compositions $\text{LaTiO}_{1.97(6)}\text{N}_{1.03(6)}$ and $\text{LaTiO}_{1.98(6)}\text{N}_{1.02(6)}$ for the oxynitrides synthesized from the ceramic and the soft chemistry precursors, respectively. The refined O/N content confirms that the anionic composition of the samples is close to the ideal, e.g. 2O^{2-} and 1N^{3-} .

The refined TiN impurity content was equal to 0.4 wt.% and 1.0 wt.% for the samples synthesized from the ceramic and the soft chemistry precursors, respectively.

Space groups for the Ca-substituted LaTiO_2N samples were assigned based solely on Rietveld refinements of their neutron data (lower crystallinity of these samples as compared to that of LaTiO_2N didn't allow us to corroborate space group assignments by TEM). The refined crystallographic data of the Ca-substituted derivatives of LaTiO_2N is given in Table 3.2.

Table 3.2. Structural parameters of the synthesized oxynitrides of general composition $\text{Ca}_{1-x}\text{La}_x\text{TiO}_{3-x}\text{N}_x$ refined from the neutron diffraction data.

Sample	x = 1	x = 0.7	x = 0.5	x = 0.3
Radiation	neutron	neutron	neutron	neutron
λ , Å	1.494	1.494	1.494	1.494
T, K	298	298	298	298
S.G.	$I\bar{1}$	<i>Pnma</i>	<i>Pnma</i>	<i>Pnma</i>

a , Å		5.6056(2)	5.5467(3)	5.5001(8)	5.4926(4)
b , Å		7.8627(4)	7.8287(5)	7.7678(15)	7.7374(6)
c , Å		5.5722(3)	5.5643(4)	5.4876(12)	5.4735(4)
α , °		90.194(6)	90	90	90
β , °		90.213(5)	90	90	90
γ , °		89.982(13)	90	90	90
V , Å ³		245.59(2)	241.63(2)	234.45(8)	232.62(3)
Z		4	4	4	4
La/Ca	x	0.5058(10)	0.0070(11)	0.008(2)	0.0215(11)
	y	¼	¼	¼	¼
	z	0.0015(17)	0.0054(15)	-0.008(4)	-0.005(2)
	B_{iso} , Å ²	0.63(4)	0.78(5)	1.26(9)	0.83(7)
	site	4i	4c	4c	4c
	occ.	1	0.7/0.3	0.5/0.5	0.3/0.7
Ti(1)	x	0	½	½	½
	y	0	0	0	0
	z	0	0	0	0
	B_{iso} , Å ²	0.54(4)	0.65(5)	0.50(8)	0.76(8)
	site	2a	4b	4b	4b
	occ.	1	1	1	1
Ti(2)	x	0	-	-	-
	y	½	-	-	-
	z	0	-	-	-
	B_{iso} , Å ²	0.54(4)	-	-	-
	site	2c	-	-	-
	occ.	1	-	-	-
O/N(1)	x	-0.0587(7)	0.4951(18)	0.497(2)	0.4894(13)
	y	0.294(4)	¼	¼	¼
	z	0.009(2)	0.0635(7)	0.0467(17)	0.0661(16)
	B_{iso} , Å ²	1.21(3)	1.06(3)	1.48(5)	0.90(4)
	site	4i	4c	4c	4c
	occ.	0.73(2)/0.27(2)	0.78(2)/0.22(2)	0.56(2)/0.44(2)	0.85(2)/0.15(2)
O/N(2)	x	0.261(4)	0.2652(8)	0.2784(11)	0.2809(8)
	y	0.0350(13)	0.0330(3)	0.0341(10)	0.0337(6)
	z	0.242(4)	0.7335(8)	0.7239(13)	0.7189(8)
	B_{iso} , Å ²	1.21(3)	1.06(3)	1.48(5)	0.90(4)
	site	4i	8h	8h	8h
	occ.	0.72(2)/0.28(2)	0.79(2)/0.21(2)	0.93(2)/0.07(2)	0.95(2)/0.05(2)
O/N(3)	x	0.261(4)	-	-	-
	y	0.4699(10)	-	-	-
	z	0.757(4)	-	-	-
	B_{iso} , Å ²	1.21(3)	-	-	-
	site	4i	-	-	-
	occ.	0.52(2)/0.48(2)	-	-	-
<Ti-O/N>		1.99(2)	1.990(3)	1.967(5)	1.970(3)
<Ti-O/N-Ti>		163.3(6)	162.10(13)	161.8(2)	159.03(14)

Anionic content	O _{1.97(6)} N _{1.03(6)}	O _{2.36(4)} N _{0.64(4)}	O _{2.42(4)} N _{0.58(4)}	O _{2.85(4)} N _{0.25(4)}
χ^2	2.48	1.56	2.65	1.17
wR_p^b	0.0799	0.127	0.119	0.128
R_p^b	0.0785	0.132	0.131	0.157

As it can be seen from the refined anionic compositions, it is possible to adjust nitrogen content to the level very close to the expected by varying Ca-content of the samples. The refined lattice parameters and $\langle \text{Ti-O/N-Ti} \rangle$ angle values confirm that simultaneous substitution of La^{3+} with Ca^{2+} and N^{3-} with O^{2-} leads to the increase of the structure distortion energy. This can be expected from the smaller ionic radii of Ca^{2+} and O^{2-} compared to those of La^{3+} and N^{3-} [35, 36]. For the same reason it could be expected that the average $\langle \text{Ti-O/N} \rangle$ distance should decrease continuously upon simultaneous substitution of La^{3+} with Ca^{2+} and N^{3-} with O^{2-} . However, this is not confirmed experimentally. The only reason for that is the presence of cationic and/or anionic defects, such as Ti^{3+} and/or oxygen vacancies.

3.3. Influence of cooling on the bulk anionic and surface composition of LaTiO_2N

A significant deviation in the O/N content calculated from the TGA and hotgas-extraction together with neutron diffraction was found for all the oxynitrides (Figure 3.8).

To study the origin of these deviations we compared the O/N content of the LaTiO_2N samples cooled in different ways as explained in Chapter 3.1.

For the LaTiO_2N samples, which were cooled in N_2 and quenched in NH_3 , respectively, the nitrogen content calculated from the thermal reoxidation in TGA led to the compositions $\text{LaTiO}_{2.06(2)}\text{N}_{0.96(1)}$ and $\text{LaTiO}_{2.075(3)}\text{N}_{0.95(2)}$. This finding is in good agreement with the results obtained by hotgas extraction, which led to $\text{LaTiO}_{2.11(1)}\text{N}_{0.95(2)}$ for the nitrogen cooled sample and $\text{LaTiO}_{2.10(3)}\text{N}_{0.97(3)}$ for the sample quenched in NH_3 .

In contrast, for the NH_3 cooled samples the weight gain in the TGA experiment was much smaller than expected, leading to a value of 0.75 for the nitrogen content (Figure 3.8). The obtained result suggests a presence of cationic vacancies, which is not in agreement with

the result of the Rietveld refinement of the cationic composition. On the other hand, from the hotgas extraction experiments the calculated composition is $\text{LaTiO}_{2.11(2)}\text{N}_{1.10(1)}$.

There are several factors, which could influence the obtained result like the presence of volatile impurities, or the formation of carbonates/oxy carbonates, especially those that decompose in the temperature region in which the reoxidation proceeds, and finally a partial reduction of the transition metal. These possible effects lead to an underestimation of the nitrogen content, whereas the presence of transition metal nitrides leads to an overestimation of the nitrogen content.

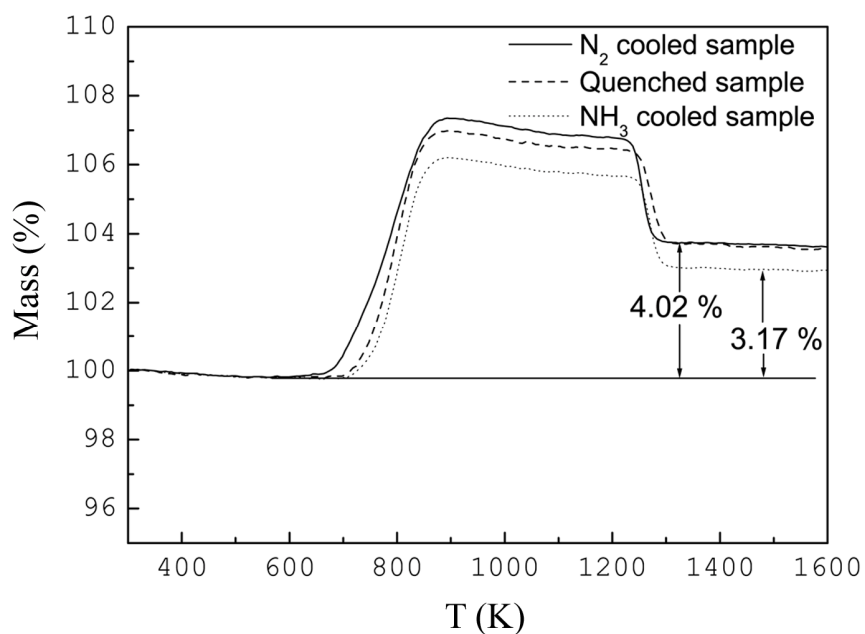


Figure 3.8. TGA of nitrogen cooled, ammonia cooled and quenched samples performed in the synthetic air with a heating rate of 10 K min^{-1} .

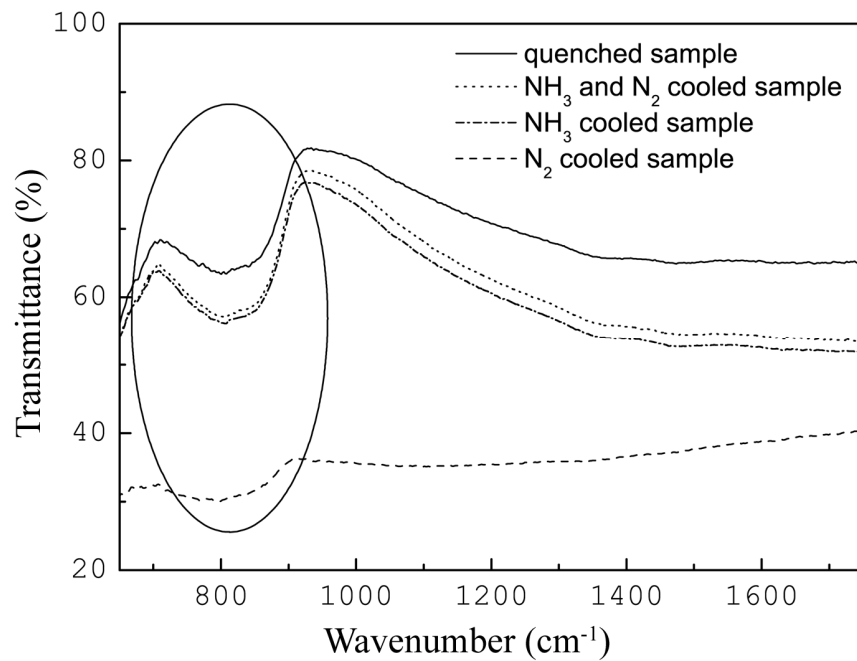


Figure 3.9. FTIR spectra of LaTiO₂N samples quenched and cooled under different atmospheres.

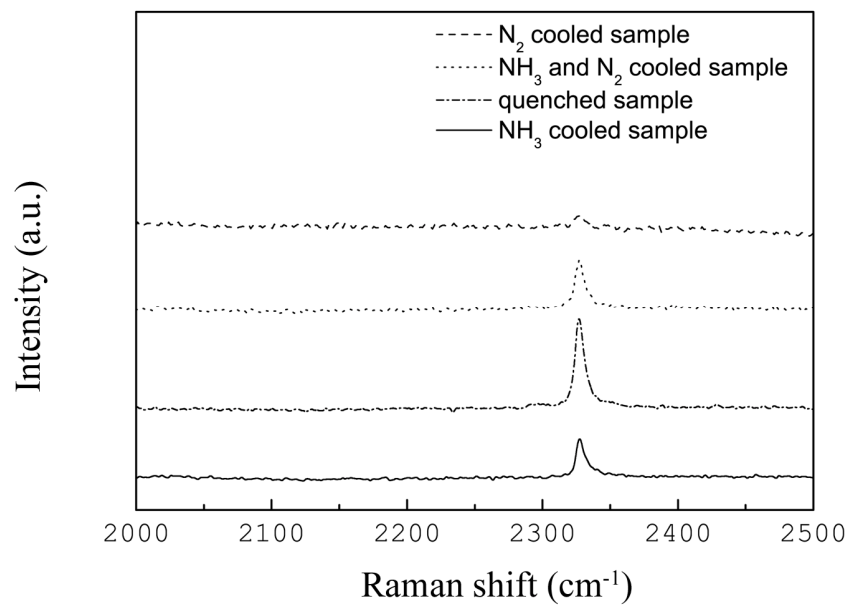


Figure 3.10. Raman spectra of LaTiO₂N samples quenched and cooled under different atmospheres.

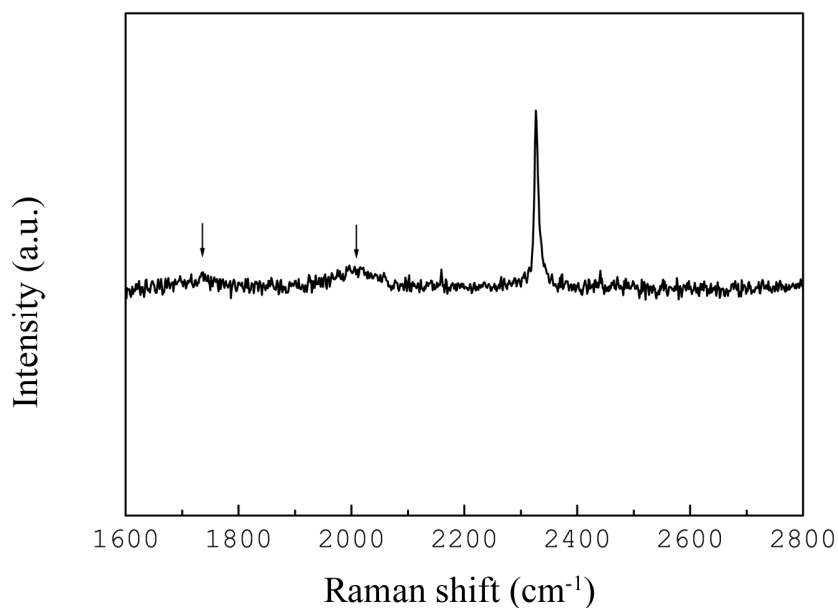


Figure 3.11. Raman spectrum of the ammonia cooled sample. The arrows indicate two additionally resolved peaks.

Results of the hotgas extraction analysis are as well affected by volatile impurities in the sample. The presence of such impurities can, on the other hand, be determined by coupling the TGA system with a mass spectrometer (MS) or by applying IR/Raman spectroscopy. Fourier Transformed Infrared (FTIR) and Raman spectra of the corresponding samples are shown in Figures 3.9,10. In the FTIR spectra broad absorption bands can be observed in the region $700\text{-}900\text{ cm}^{-1}$. The observed bands can be attributed either to the CO_3^{2-} -ion ($\nu_2 = 725\text{ cm}^{-1}$ and $\nu_4 = 850\text{ cm}^{-1}$) or to the $\text{NO}_3^-/\text{NO}_2^-$ -ions ($\nu = 800\text{-}850\text{ cm}^{-1}$). The most intense signals at these frequencies were measured for the ammonia cooled samples, whereas the weakest signal was measured for the nitrogen cooled sample. The presence of traces of carbonates and nitrates in these samples was confirmed by the evolution of CO_2 ($m/z = 44$) and NO ($m/z = 30$) detected by MS during the reoxidation of all the samples in TGA. It is to be noted that the neither x-ray nor neutron diffraction gave hints for the carbonates/nitrates.

In the Raman spectra shown in Figure 3.10 the frequency region which is characteristic for dinitrogen containing reoxidation intermediates (approx. 2235 cm^{-1}) [50, 68, 69, 71, 73, 95] is depicted. The most intense signal of N_2 is measured for the quenched sample. This can be explained by oxygen diffusion inside the reactor due to the pressure drop during the quenching.

Comparison of the anionic composition of the ammonia cooled sample and the sample which was cooled in ammonia to 1000 K and in nitrogen to room temperature suggests that the main changes within the samples appear in the temperature region between 1223 and 1000 K. The nitrogen content in both samples is 10 % higher than the theoretical value. Close inspection of the Raman and IR data reveals two additional weak features at $\nu = 1700$ and 2000 cm^{-1} in the spectra of these samples (Figure 3.11). These frequencies cannot be detected in the spectra of the nitrogen cooled and quenched samples. Very weak frequency at $\nu = 2000\text{ cm}^{-1}$ can be attributed to the $\text{C} \equiv \text{N}$ stretching mode of CN^- ions, which may be part of a $[\text{Ti}^{3+}(\text{CN})_n]^{3-n}$ complex [113]. The frequency at 1700 cm^{-1} corresponds to the NH_4^+ ion. Presence of those two species should lead to overestimated N content for the samples cooled in ammonia.

According to the information from the gas supplier ammonia contains traces of H_2O , CO , CO_2 , O_2 and oil. Hence, the carbonization of the material surface must occur due to the interaction between the carbon containing gases coming with ammonia and La^{3+} which is known for its high affinity to carbon. Additionally, partial reoxidation of the material surface occurs due to the presence of oxygen traces.

The enhancement of the chemical stability of the oxynitride samples, which have their surface carbonized and reoxidized, can be seen when comparing their reoxidation curves with those of the samples with a noncontaminated surface (Figure 3.8). Apparently, the former starts to react with oxygen at lower temperatures than the latter one. Hence, the impurity layer on the top of the LaTiO_2N particles acts as a barrier layer, protecting the material from decomposition. This effect occurs due to the chemical stability of the compounds formed on the surface, for example lanthanum carbonate, which has its decomposition temperature around 1223 K.

3.4. Optical properties

Diffuse reflectance spectra of the synthesized oxynitrides are presented in Fig. 3.12. Corresponding band gap values for the direct optical transitions and colors of the obtained oxynitrides are listed in Table 3.3. Band gap values calculated from the Mott-Davis and Shapiro's methods are equal for all the compositions except of LaTiO_2N . For this compound the Mott-Davis method resulted in the band gap value of 2.2 eV, whereas Shapiro's method gave the value of 2.1 eV. The difference is most probably caused by the change in the diffuse reflectance of that compound which is not steep enough for the unambiguous determination of the linear region. The value of 2.1 eV is in accordance with the literature reported band gap value of LaTiO_2N [11]. As it can be seen from Figures 3.13 and 3.14 the band gap width increases with the increase in Ca content. The observed band gap width increase is in accordance with the measured decrease in the nitrogen content and the structure distortion energy increase (as it follows from the $\langle\text{Ti-O/N-Ti}\rangle$ angle values obtained from the neutron diffraction study).

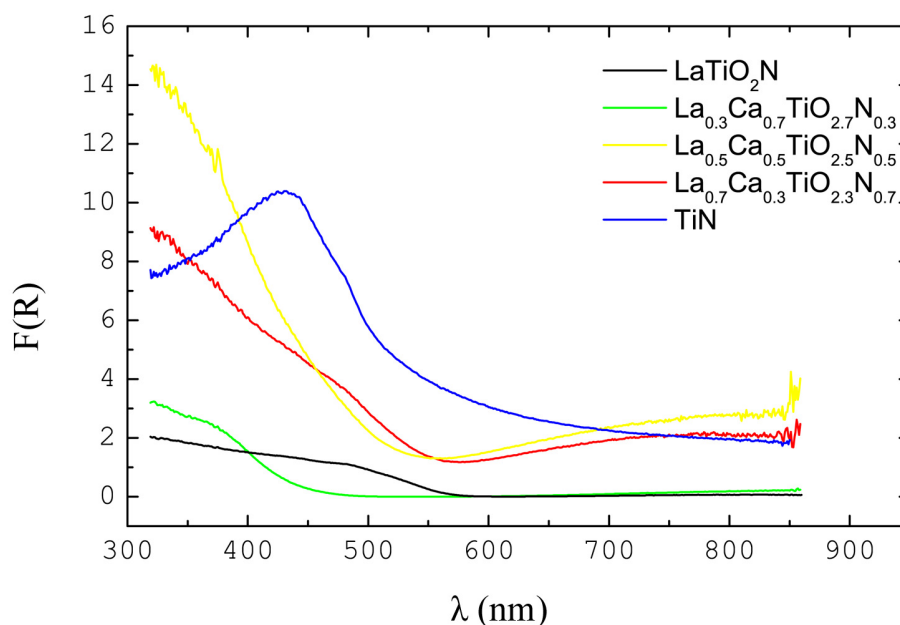


Figure 3.12. UV-VIS diffuse reflectance spectra for the $\text{Ca}_{1-x}\text{La}_x\text{TiO}_{3-x}\text{N}_x$ oxynitrides.

Table 3.3. Optical band gaps and colors of the $\text{Ca}_{1-x}\text{La}_x\text{TiO}_{3-x}\text{N}_x$ oxynitrides.

Composition	Band gap, eV (Davis-Mott)	Band gap, eV (Shapiro)	Color
LaTiO_2N	2.23	2.11	Brown
$\text{La}_{0.7}\text{Ca}_{0.3}\text{TiO}_{2.3}\text{N}_{0.7}$	2.34	2.30	Brownish-Green
$\text{La}_{0.5}\text{Ca}_{0.5}\text{TiO}_{2.5}\text{N}_{0.5}$	2.75	2.72	Green
$\text{La}_{0.3}\text{Ca}_{0.7}\text{TiO}_{2.7}\text{N}_{0.3}$	2.96	2.95	Light-Green
CaTiO_3	3.31	3.30	White

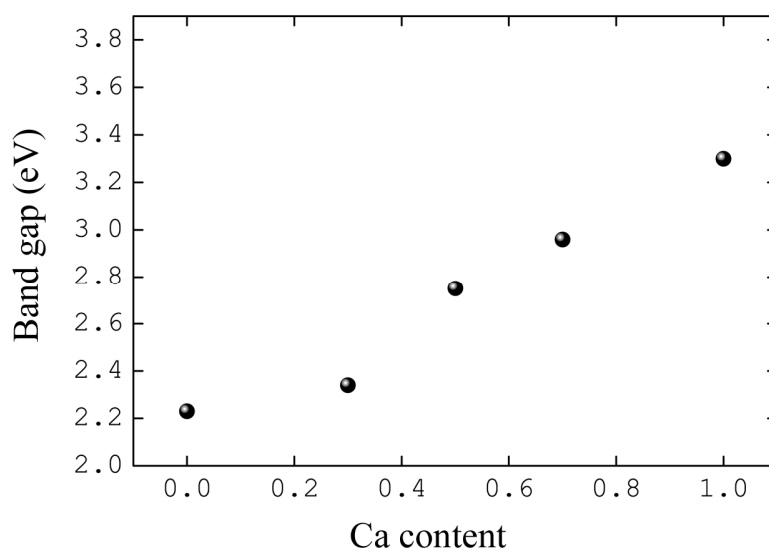


Figure 3.13. Band gap energy (as evaluated by the Mott-Davis method) dependence on Ca content.

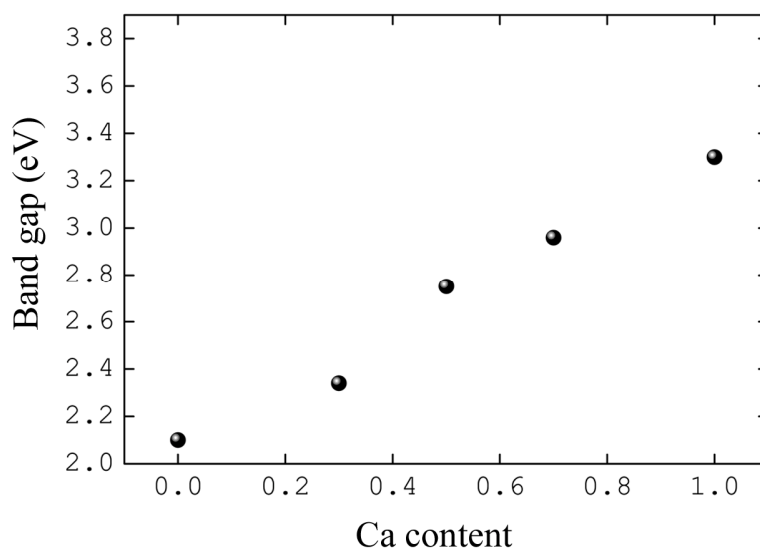


Figure 3.14. Band gap energy (as evaluated by the Shapiro's interpolation method) dependence on Ca content.

The measured band gap width dependence on Ca content is close to the linear, which confirms the possibility of fine-tuning the band gap energy by cross-substitution.

3.5. Conclusions

Oxynitrides with the general formula $\text{Ca}_{1-x}\text{La}_x\text{TiO}_{3-x}\text{N}_x$ ($x=0, 0.3, 0.5, 0.7$) were synthesized for the first time. Their crystal structure, thermal stability and optical properties were studied.

All the materials were prepared by thermal ammonolysis of the corresponding oxide precursors. However, Ca-containing oxynitrides are metastable under the ammonolysis conditions. Thus, time, temperature and ammonia flow have to be carefully adjusted to reduce amounts of the secondary phases (TiN and CaO).

Thermal reoxidation of the synthesized oxynitrides proceeds via the formation of dinitrogen-containing intermediates. The decomposition rate of the reoxidation

intermediates correlates with the structural changes occurring during their transformation to the corresponding oxides.

Thermal treatment of the obtained oxynitrides in nitrogen and helium atmospheres leads to their decomposition. The decomposition results in multiphase mixtures, which contain Ti^{3+} . Since the only detected species in the atmosphere are N_2 molecules the self reduction with the intrinsic N^{3-} occurs. Apparently, the formation of the stable N_2 molecule is the main driving force of this process.

All the oxynitrides crystallize in a distorted perovskite-type structure. The degree of the perovskite structure distortion decreases with increasing Ca content (as confirmed by neutron diffraction) mainly due to the smaller ionic radii of Ca^{2+} and O^{2-} as compared to those of La^{3+} and N^{3-} . Neutron diffraction and hot-gas extraction confirm the O/N content of the synthesized samples close to the predicted.

The amorphous carbonate, nitrate and reoxidation intermediate impurities formed on the surface of $LaTiO_2N$ during the synthesis cannot be detected either by x-ray or by neutron diffraction. For this purpose the IR and Raman spectroscopic techniques have to be applied to avoid serious mistakes on the O/N content evaluation when using TGA.

The combination of the diffraction and spectroscopic techniques allowed revealing important relations between the cooling mode, the surface- and the anionic composition of $LaTiO_2N$. The obtained results are essential for understanding physical and catalytic properties of oxynitrides as well as for their accurate O/N content determination.

In general, the surface contamination has to be taken into account since it often leads to a decrease of the photocatalytic performance. Special precaution should be taken during the synthesis procedure in this case, i.e. high purity gases should be utilized for the sample cooling. Alternatively, the sample can be rapidly quenched down to the room temperature.

The band gap of the materials increases linearly with increasing Ca^{2+} content (decreasing N^{3-} content), i.e. the concomitantly increasing ionicity of the chemical bonds and increasing the perovskite structure distortion energy. Due to the linear response between the optical band gap value and composition, cross substitution within $Ca_{1-x}La_xTiO_{3-x}N_x$ series is effective to change optical properties of the constituent members. Together with good

thermal and chemical stability, this makes the synthesized oxynitrides prominent for the photocatalytic and pigment applications study.

4. LaNbON₂

4.1. Synthesis and stability

The oxide precursor for the ammonolysis was prepared by a complex polymerization method [50] as described in Chapter 2. La(NO₃)₃•6H₂O (Merck, >99.0%), NbCl₅ (Aldrich, 99.0%) and citric acid (Merck, >99%) were used as starting compounds.

A mass of 0.5 g of NbCl₅ was dissolved in a 50 ml of pure ethanol. An excess of citric acid in molar ratio of 3(citric acid):1(total amount of cations) was added to the formed solution under the constant stirring. After complete dissolution of citric acid La(NO₃)₃•6H₂O was added. The obtained solution was predried at 573 K and calcined at 1323 K to yield in LaNbO₄.

The ammonolysis reaction was performed in a rotating cavity reactor made of alumina. Air in the reactor was replaced by nitrogen (PanGas, 99.999%). The sample was then heated under a nitrogen flow of 100 mL min⁻¹ until the reaction temperature was reached and nitrogen was replaced by ammonia (PanGas, >99.985%). 2 g of the oxide precursor was ammonolyzed at 1223 K, using an ammonia flow of 300-400 mL min⁻¹. The reaction time was 31 h. Oxide samples were ammonolyzed with- and without adding a flux (KCl). One of the ammonolyzed samples was quenched down to room temperature within 2 minutes, whereas the other was slowly cooled down within 7 hours.

XRPD confirmed the phase purity of LaNbO₄ produced at 1323 K. (Figure 4.1). XRPD pattern of the oxynitride phase formed after the ammonolysis without KCl revealed broad reflections which can be indexed using a cubic perovskite unit cell (Figure 4.2A). Asymmetry of high-angle reflections confirms that the actual symmetry of that material is lower than cubic. More reflections could be resolved on the XRPD pattern of the oxynitride samples obtained by the ammonolysis with KCl (Figure 4.2B). This confirms its better crystallinity as compared to the sample synthesized without the flux. SEM images taken from that the starting LaNbO₄ and the synthesized oxynitrides are shown in Figure 4.3.

SEM of the starting oxide shows $\mu\text{-size}$ particles (Figure 4.3A). For the sample ammonolyzed without flux 1-2 μm agglomerates formed by ~ 100 nm-size particles can be seen (Figure 4.3B). Apparently the sample of such a low crystallinity is not suitable to attempt its crystal structure determination. SEM of the oxynitride sample synthesized with the flux (Figure 4.3C) revealed that its microstructure is mainly represented by $\mu\text{-size}$ rectangular particles coexisting with agglomerates similar to those found for the flux-free ammonolyzed sample. The presence of these agglomerates in the flux-ammonolyzed sample can be attributed to the nonuniform flux distribution. Due to the better crystallinity of the flux-ammonolyzed samples they were used for the crystallographic study.

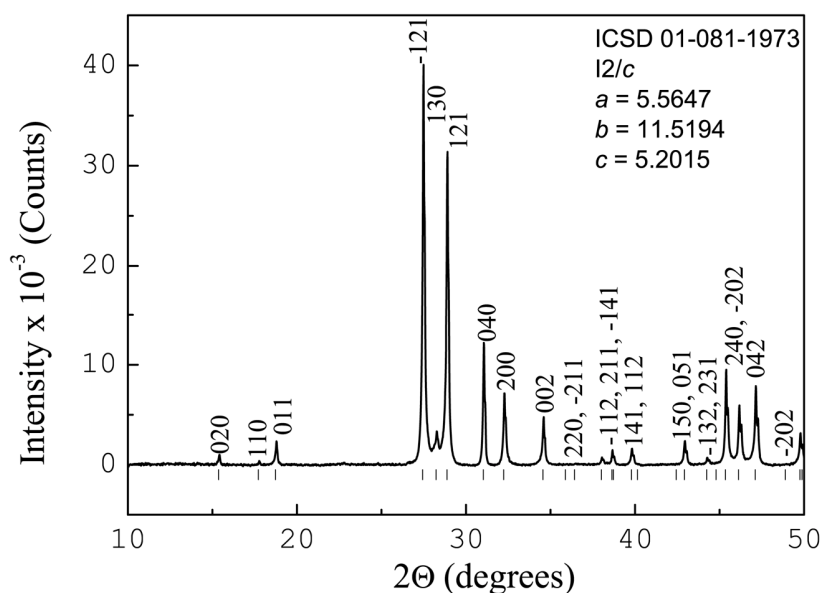


Figure 4.1. XRPD pattern of LaNbO_4 after annealing at 1323 K for 12 hours. Space group: $I2/c$. The reflections are assigned according to the pdf entry 01-081-1973.

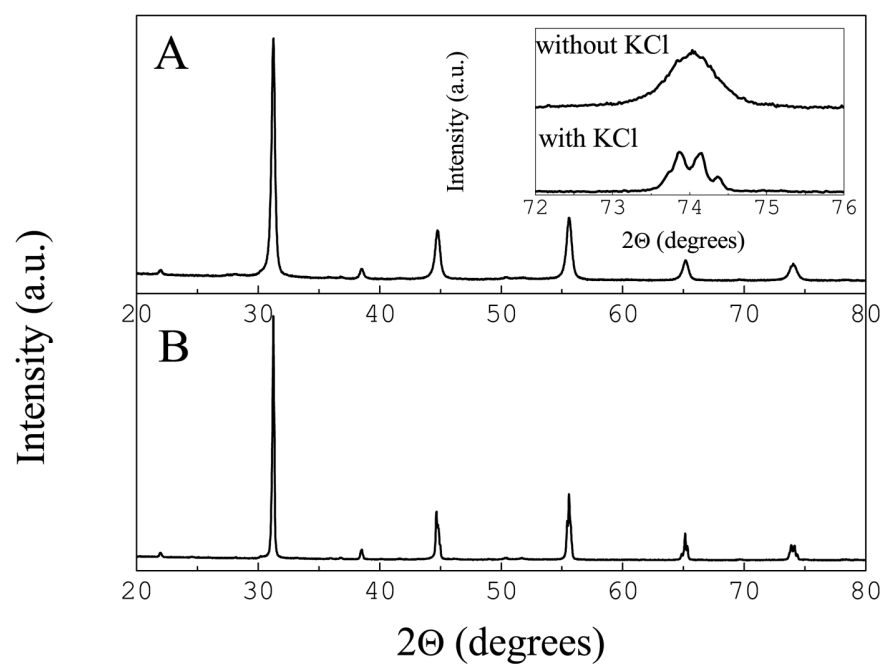


Figure 4.2. XRPD pattern of LaNbON₂ synthesized: A. Without adding a flux (KCl); B. With adding the flux. The inset demonstrates difference in crystallinity of the oxynitride powders synthesized with and without adding the flux.

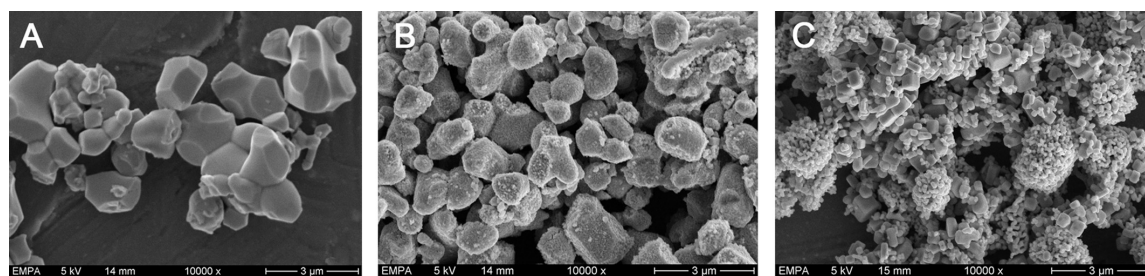


Figure 4.3. SEM micrographs of: A. LaNbO₄; B. LaNbON₂ synthesized without the flux; C. LaNbON₂ synthesized with the flux (KCl).

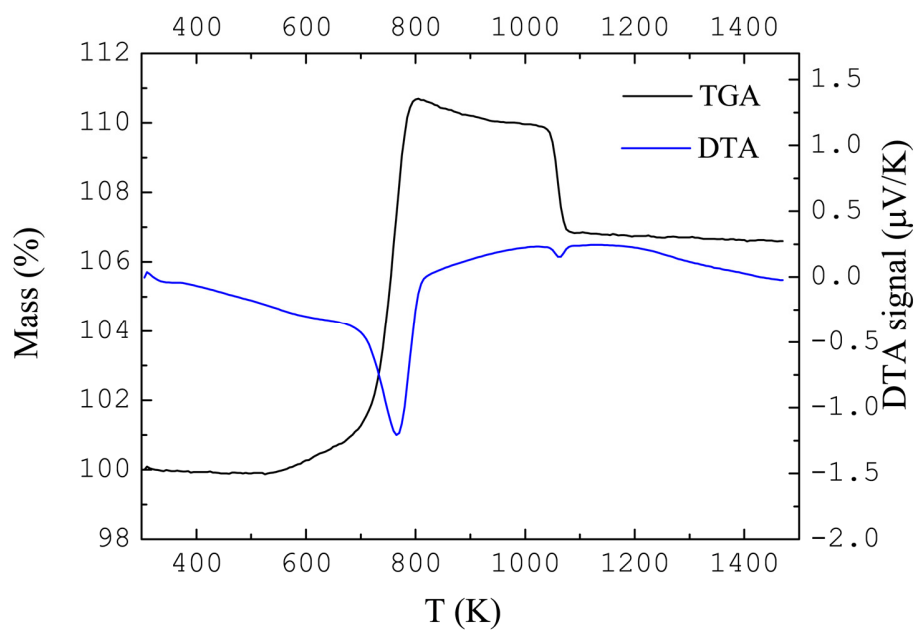


Figure 4.4. TGA and DTA thermal reoxidation curves of LaNbON_2

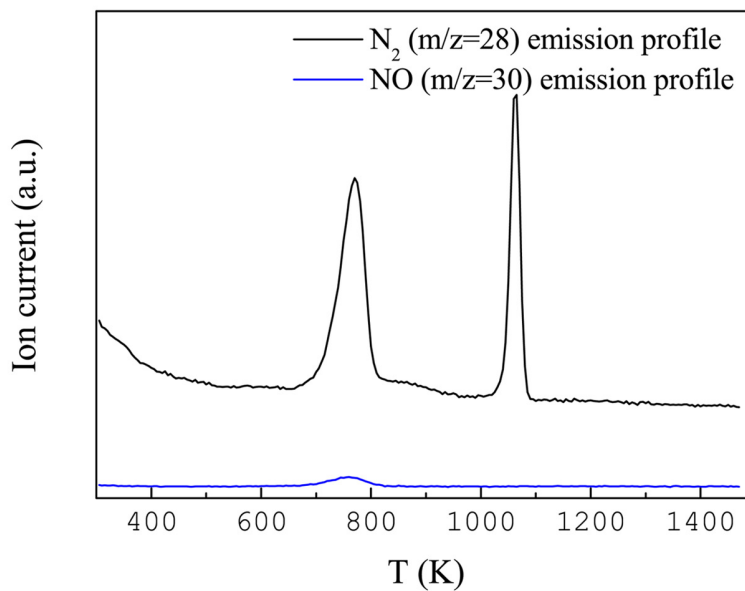


Figure 4.5. MS signals of N_2 ($m/z = 28$) and NO ($m/z = 30$) monitored during the thermal reoxidation of LaNbON_2

Reoxidation study of LaNbON_2 performed under synthetic air in the TGA (Figure 4.4) revealed the stability of the material up to $T = 500$ K. Further heating led to the formation of the reoxidation intermediate. The intermediate decomposed at $T > 1000$ K resulting in the formation of the single phase LaNbO_4 . Thus, the decomposition proceeded according to the scenario, which was already established for other perovskite-type oxynitrides [68, 69, 73] and was discussed in details in Chapter 3. MS revealed N_2 ($m/z = 28$) retention during the intermediate formation and decomposition steps (Figure 4.5). Moreover, NO ($m/z = 30$) retention was measured during the formation of the reoxidation intermediate.

The weight gain measured during the reoxidation of the quenched sample corresponds to the composition of $\text{LaNbO}_{1.07(2)}\text{N}_{1.93(2)}$.

4.2. Room and low T crystal structure

Due to similar ionic radii of Ta^{5+} and Nb^{5+} , we attempted to refine the LaNbON_2 XRPD data using the structural model reported before for LaTaON_2 (S.G. $C2/m$) [58]. Le-Bail refinement of the XRPD data performed using this structural model revealed a fairly good fit, however a close examination of the XRPD profile revealed weak superstructure reflections, which were not accounted for by the $C2/m$ model and could not be attributed to the most probable impurity phases (La_2O_3 , NbON , KCl and unreacted LaNbO_4). Subsequent Rietveld refinement of the XRPD data revealed unstable thermal displacement parameters and a strong correlation between the c – lattice parameter and the angle β . The refined value for the angle $\beta = 134.90(5)$ is close to the value 135° , which means that the actual symmetry of the material can be higher than monoclinic. All the observed reflections can be indexed on the base of a primitive unit cell with $a \approx c \approx \sqrt{2} * a_p$ and $b \approx 2 * a_p$. The observed extinctions can correspond to the space group $Pnma$ or its subgroup $P2_1/n$. According to the lattice parameters settings used by Howard and Stoke [4, 112], $Pnma$ can be related to $P2_1/n$ by the following matrix:

$$\begin{pmatrix} 1/2 & 1/2 & 1/2 \\ 1/2 & -1/2 & 1/2 \\ 1 & 0 & -1 \end{pmatrix}$$

The reflection condition $(hk0)$: $h = 2n$ does not allow the reflection (110) , which belongs to the zone axis $[001]$, to appear in the S.G. $Pnma$. The reflection corresponds to the reflection (101) in the $P2_1/n$ and is allowed in this space group. Hence, if no twinning occurs, these space groups can easily be distinguished from the electron diffraction images. Electron diffraction of LaNbON_2 confirmed the absence of (110) reflection in $[001]$ zone axis (Figure 4.6A).

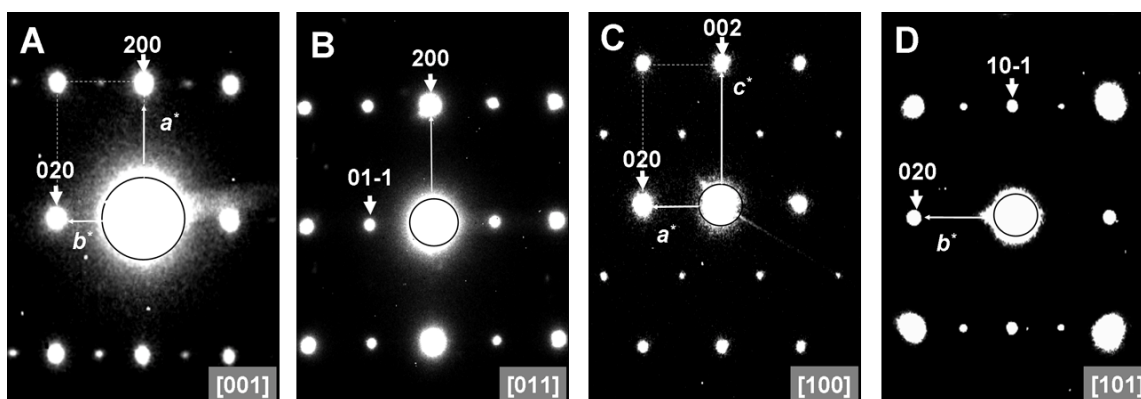


Figure 4.6. Electron diffraction patterns of LaNbON_2 taken along: A. $[001]$ zone axis; B. $[011]$ zone axis; C. $[100]$ zone axis; D. $[101]$ zone axis.

Diffraction patterns taken along other zone axis confirmed the reflection conditions for the space group $Pnma$ (Figure 4.6): $(0kl)$: $k+l = 2n$; $(h00)$: $h = 2n$; $(k00)$: $k=2n$; $(00l)$: $l = 2n$. Further Rietveld refinement of the neutron diffraction data was performed in the space group $Pnma$. The cationic composition was fixed to the stoichiometric ratio 1:1. Anionic sites were initially randomly populated by O^{2-} - and N^{3-} - ions with the molar ratio 1:2. Lattice parameters obtained from the preliminary Le-Bail refinement were used as starting ones. The refinement of the detectors zero, background, profile parameters, atomic coordinates, lattice parameters and isotropic thermal displacement factors ended up with $\chi^2 = 1.7$. Further refinement of the anisotropic thermal displacement factors reduced this value down to 1.52 (Figure 4.7).

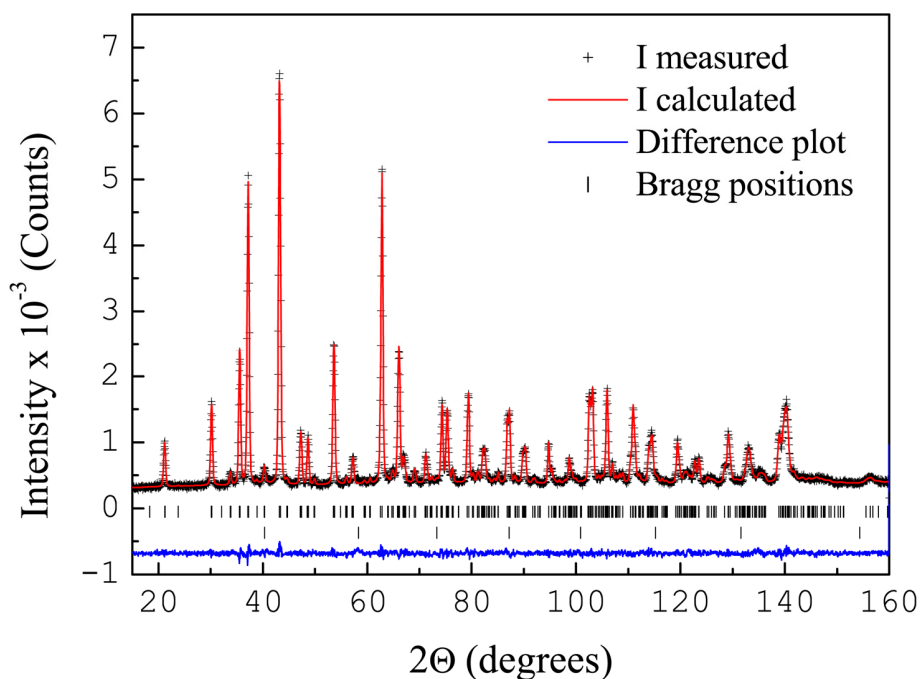


Figure 4.7. Rietveld refinement plot of the neutron powder diffraction data for the ammonia cooled LaNbON_2 . Space group: $Pnma$. The observed intensities, calculated profile, difference curve and Bragg positions are shown. Vanadium (the container material) has been included as a minor impurity phase in the refinement.

The refinement of the cationic occupancies with the fixed anionic occupancies did not give any hint for possible cationic vacancies. The refinement of the anionic occupancy resulted in $\text{LaNbN}_{1.98(5)}\text{O}_{1.02(5)}$ and $\text{LaNbN}_{1.97(5)}\text{O}_{1.03(5)}$ composition for the quenched and the slowly cooled oxynitride, respectively, and a totally disordered anionic arrangement for both the samples. Within the doubled standard deviation (2σ) the refined O/N content values are close to those determined from the TGA experiment. The analysis of the correlation matrix revealed no serious correlations between the structural parameters. The summary of the refinements against the space group $Pnma$ is given in Tables 4.1 and 4.2. Cooling the sample down to 1.5 K does not cause its crystallographic symmetry change, but the

increase of the structure distortion degree. The latter is reflected in the lower value of the average $\langle \text{Nb}-(\text{O}/\text{N})-\text{Nb} \rangle$ angle measured for the cooled sample (Table 4.2).

Table 4.1. Structural parameters of LaNbON_2 at 298 K and 1.5 K refined from the neutron diffraction data.

Name		LaNbON_2	LaNbON_2
radiation		neutron (HRPT, PSI)	neutron (HRPT, PSI)
	λ , Å	1.494	1.494
	T, K	298	1.5
	S.G.	<i>Pbnm</i>	<i>Pbnm</i>
	a , Å	5.7307(1)	5.7221(1)
	b , Å	8.0836(1)	8.0684(1)
	c , Å	5.7558(1)	5.7428(1)
	V , Å ³	266.63(1)	265.13(1)
	Z	4	4
La	x	-0.0146(4)	-0.0179(3)
	y	$\frac{1}{4}$	$\frac{1}{4}$
	z	-0.0038(4)	-0.0044(4)
	B_{iso} , Å ²	1.10(3)	0.74(3)
Nb	site	4c	4c
	occ.	1	1
	x	$\frac{1}{2}$	$\frac{1}{2}$
	y	0	0
O/N(1)	z	0	0
	$B_{iso}(eq)$, Å ²	0.86	0.89
	site	4b	4b
	occ.	1	1
O/N(2)	x	0.5052(5)	0.5082(5)
	y	$\frac{1}{4}$	$\frac{1}{4}$
	z	0.0719(3)	0.0743(3)
	$B_{iso}(eq)$, Å ²	1.11	0.83
O/N(2)	site	4c	4c
	occ.	0.60(2)/0.40(2)	0.56(3)/0.44(3)
	x	0.2310(3)	0.2281(3)
	y	0.03751(15)	0.03829(16)
	z	0.7689(3)	0.7722(3)
	$B_{iso}(eq)$, Å ²	1.61	1.45
	site	8d	8d
	occ.	0.692(15)/0.308(15)	0.725(18)/0.275(18)
χ^2		1.52	1.59
wR_p^b		0.0930	0.115
R_p^b		0.0876	0.108

Anisotropic displacement parameters of atoms in Å²

Atom	B_{11}	B_{22}	B_{33}	B_{12}	B_{13}	B_{23}
298 K						
Nb	0.0093(5)	0.0027(3)	0.0051(5)	0.0005(4)	0	0.0005(4)
O/N(1)	0.0131(8)	0.0022(3)	0.0078(5)	0	0.0036(6)	0
O/N(2)	0.0120(5)	0.0060(2)	0.0127(5)	0.0022(3)	-0.0073(3)	-0.0019(4)
1.5 K						
Nb	0.0079(6)	0.0031(3)	0.0061(6)	0.0008(4)	0.0013(9)	-0.0009(4)
O/N(1)	0.0121(8)	0.0010(3)	0.0051(5)	0	0.0034(6)	0
O/N(2)	0.0110(5)	0.0057(2)	0.0110(5)	0.0014(3)	-0.0055(3)	-0.015(3)

Table 4.2. Selected bond distances in Å and angles in degrees for LaNbON₂ at 298 K and 1.5 K.

		LaNbON ₂ 298 K	LaNbON ₂ 1.5 K
Nb-O/N(1)	x2	2.0630(3)	2.0623(4)
Nb-O/N(2)	x2	2.0586(17)	2.0561(17)
Nb-O/N(2)	x2	2.0591(17)	2.0597(17)
<Nb-O/N>		2.0602(12)	2.0594(12)
La-O/N(1)		2.786(4)	2.750(3)
La-O/N(1)		3.011(4)	3.044(3)
La-O/N(1)		3.272(3)	3.276(3)
La-O/N(1)		2.489(3)	2.474(3)
La-O/N(2)	x2	2.721(2)	2.720(2)
La-O/N(2)	x2	2.961(2)	2.939(2)
La-O/N(2)	x2	3.241(2)	3.268(2)
La-O/N(2)	x2	2.577(2)	2.558(2)
<La-O/N> _(8 short)		2.724(2)	2.707(2)
Nb-O/N(1)-Nb	x2	156.795(14)	155.972(14)
Nb-O/N(2)-Nb	x4	160.99(7)	160.02(7)
<Nb-O/N-Nb>		159.59(5)	158.67(5)

A number of differences can be noticed between crystal structures of LaNbON₂ and LaTaON₂. One of the most significant is the difference in the crystallographic symmetry. This could not be predicted, since Ta⁵⁺ and Nb⁵⁺ have identical ionic radii [35, 36]. Indeed,

all the previously synthesized niobium- and tantalum-oxynitrides of the general formula ABO_2N ($A = Ca^{2+}, Sr^{2+}, Ba^{2+}, B = Nb^{5+}, Ta^{5+}$) with the same A -site cation are isostructural [38, 87]. The difference in the anionic/cationic composition of $LaNbON_2$ and $LaTaON_2$ is the most reasonable explanation for the observed difference in the symmetry. Another significant difference is that $LaNbON_2$ possesses a totally disordered anionic arrangement, whereas a totally ordered anionic arrangement was reported for $LaTaON_2$ [58]. The origin of the partial or complete anionic ordering in oxynitride-type perovskites is not well understood. However, it seems to be connected with the differences in their preparation (in particular, the difference in the temperature of the ammonolysis, the cooling program or the mineralizer used).

4.3. Optical properties and photocatalytic activity

UV-Vis DR spectra of the starting oxide and the synthesized oxynitrides reveal that partial replacement of oxygen with nitrogen leads to a progressive reduction of band gap width (Figure 4.8). For the starting oxide $LaNbO_4$ band gap values calculated from Shapiro's and Davis-Mott methods are equal to 3.3 eV and 3.7 eV, respectively. For the slowly cooled and quenched oxynitride samples both these methods give the value of 1.7 eV. So far, the smallest band gap values have been reported for $BaTaO_2N$ (1.8 eV) and $BaNbO_2N$ (1.8 eV). Among the tantalum containing oxynitride-perovskites with different A -site cations, the band gap decreases in the following order: $CaTaO_2N$ (2.4 eV) > $SrTaO_2N$ (2.1 eV) > $LaTaON_2$ (1.9 eV) > $BaTaO_2N$ (1.8 eV) [38]. For the Nb^{5+} -containing analogues the following sequence is observed: $CaNbO_2N$ (2.1 eV) > $SrNbO_2N$ (1.9 eV) > $BaNbO_2N$ (1.8 eV) [38]. As it is discussed in Chapter 1, optical band gap values of oxynitrides depend primarily upon their B -site cation electronegativity, degree of the structure distortion and nitrogen content. The higher average band gap value for tantalates as compared to niobates is in the accordance with higher electronegativity of Nb^{5+} as compared to that of Ta^{5+} [5]. Within the tantalate series of general formula $ATaO_2N$, the band gap value decreases as the degree of the structure distortion decreases, *i.e.* as the ionic radii of the A -site cation increases. When the structure distortion is large enough it can fully compensate the influence of the nitrogen content increase on the band gap value. This explains the larger

band gap value for cubic BaTaO₂N ($\langle\text{Ta-O/N-Ta}\rangle=180^0$) as compared to monoclinic LaTaON₂ ($\langle\text{Ta-O/N-Ta}\rangle=156.77^0$) [58]. Hence, among the tantalate series the influence of the structure distortion on the band gap value dominates over the influence of the nitrogen content. Within the niobate series (ANbO₂N) the band gap value decreases as the degree of the structure distortion decreases, similar to the observation in the tantalate series. However, within the niobate series $E_{\text{band.g}}(\text{BaNbO}_2\text{N}) < E_{\text{band.g}}(\text{LaNbON}_2)$. The fact that $E_{\text{band.g}}(\text{LaTaON}_2) > E_{\text{band.g}}(\text{BaTaO}_2\text{N})$, whereas $E_{\text{band.g}}(\text{BaNbO}_2\text{N}) < E_{\text{band.g}}(\text{LaNbON}_2)$ can be explained by the difference in the degree of the structure distortion of LaNbON₂ and LaTaON₂. The latter is reflected in their $\langle B\text{-O/N-B}\rangle$ angle values ($B = \text{Ta}^{5+}, \text{Nb}^{5+}$). The $\langle\text{Nb-O/N-Nb}\rangle$ angle value of LaNbON₂ is equal to 159.59^0 , which is slightly larger than the $\langle\text{Ta-O/N-Ta}\rangle$ angle value of LaTaON₂ (156.77^0). Hence, in LaNbON₂ the influence of the high nitrogen content on the band gap value is not fully compensated by the structure distortion.

Table 4.3 contains the information on the photocatalytic activity and surface area of LaNbON₂, LaNbO₄ and TiO₂ (P25) used as a reference. As it can be seen from the Table, the partial oxygen replacement with nitrogen in LaNbO₄ leads to the significant improvement of the photocatalytic activity. Although, TiO₂ with- and without Pt modification produces more hydrogen (in $\mu\text{mol g}^{-1} \text{h}^{-1}$) than LaNbON₂, it should be noted that the surface area of TiO₂ is about ten times larger than that of LaNbON₂. The hydrogen evolution rate normalized to the sample's surface area ($\mu\text{mol g}^{-1} \text{h}^{-1} \text{m}^{-2}$) is about 4 times higher for LaNbON₂ than for TiO₂. Platinum modification significantly improves the photocatalytic performance of TiO₂. For LaNbON₂ the opposite influence of the Pt-modification on the photocatalytic performance is revealed: the hydrogen evolution rate decreases from $12.7 \mu\text{mol g}^{-1} \text{h}^{-1} \text{m}^{-2}$ down to $0.2 \mu\text{mol g}^{-1} \text{h}^{-1} \text{m}^{-2}$. Annealing of Pt-modified LaNbON₂ at $T=373 \text{ K}$ in air during 1 hour slightly increases the hydrogen evolution rate up to $1.7 \mu\text{mol g}^{-1} \text{h}^{-1} \text{m}^{-2}$. This data confirms that partial reduction of LaNbON₂ surface occurs during the Pt-impregnation process. Within testing time of 4 hours no significant changes in the hydrogen evolution rate were detected, which evidences that LaNbON₂ is stable under the reaction conditions.

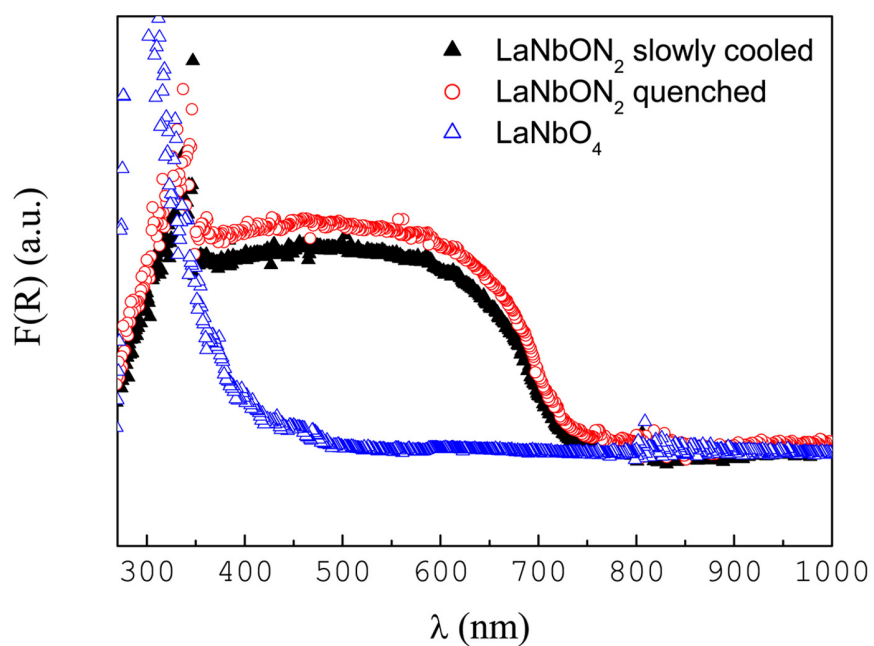


Figure 4.8. Optical spectra of LaNbO_4 and LaNbON_2 (slowly cooled and quenched).

Table 4.3. Photocatalytic activity and surface area of Pt-modified and as-prepared TiO_2 , LaNbON_2 and Pt-modified LaNbO_4 .

Sample	H_2 evolution rate, $\mu\text{mol g}^{-1} \text{h}^{-1}$	H_2 evolution rate, $\mu\text{mol g}^{-1} \text{h}^{-1} \text{m}^{-2}$	Surface area, $\text{m}^2 \text{g}^{-1}$
LaNbON_2 (q)	65	12.7	5.1
LaNbON_2 (q)+Pt	1.0	0.2	5.1
LaNbON_2 (q)+Pt, air annealed	8.9	1.7	5.1
LaNbO_4 +Pt	1.1	0.4	2.7
TiO_2	152	3.04	50
TiO_2 +Pt	3721.3	74.72	50

4.4. Conclusions

Perovskite-type oxynitride LaNbON_2 was successfully synthesized by thermal ammonolysis of the oxide precursor LaNbO_4 . Addition of the KCl flux during ammonolysis resulted in a material with better crystallinity, which is essential for the crystal structure determination and refinement. At room temperature LaNbON_2 crystallizes in the distorted GdFeO_3 -like structure (space group: $Pnma$) as derived from the x-ray and electron diffraction studies. According to the neutron diffraction data, LaNbON_2 possesses totally disordered anionic arrangement irrespective of the thermal history.

According to the UV-Vis DR spectroscopic study, LaNbON_2 possesses the smallest optical band gap (1.7 eV) among the known oxynitride-perovskites.

The material shows considerable photocatalytic activity comparable with that of commercial TiO_2 . An attempt to modify LaNbON_2 surface with 0.5 wt % of Pt led to the surface reduction and, consequently, degradation of the photocatalytic behavior. From the photocatalytic activity tests it follows that the further improvement of the photocatalytic performance of LaNbON_2 can be achieved by: (1) development of the method, which assures effective deposition of platinum on the material's surface without causing its reduction; (2) development of the method, which allows producing the oxynitride with high surface area.

5. Mo-containing oxynitrides

5.1. SrMoO_{3-x}N_x (x > 1)

5.1.1. Synthesis and stability

0.04 mol of MoO₃ (JMC, Specpure) was dissolved in a minimal amount (*ca* 20 ml) of NH₃ (aq, 25 %) and precipitated with 100 ml of an aqueous solution of Sr(NO₃)₂ (Merck, > 99%) with the concentration of 0.4 mol L⁻¹. The precipitate was washed with distilled water, dried and annealed at 1073 K for 4 hours to form phase pure, well crystalline SrMoO₄ as confirmed by XRPD (Fig. 5.1A).

SrMoO₃ was prepared by reduction of 1 g freshly synthesized SrMoO₄ at T = 1373 K with forming gas (5% H₂ / 95% N₂, 99.999% purity, Pangas). A gas flow of 300 mL min⁻¹ was applied. The reduction was completed in 5 hours. The prepared material was of a purple-red color. Its phase purity was confirmed by XRPD (Fig. 5.1B) [86]. When stored at ambient conditions SrMoO₃ transforms slowly to SrMoO₄. The presence of moisture promotes a faster SrMoO₄ formation. Therefore, in between handlings the material was kept in a desiccator.

The amount of 2.25 g of the SrMoO₄ powder was ammonolyzed at T = 1073 K under ammonia (PanGas, >99.98%) flow of 150 mL min⁻¹. The synthesis temperature was reached with a heating rate of 10 K min⁻¹. After the reaction, the furnace was cooled down to room temperature with a cooling rate of 10 K min⁻¹ under flowing ammonia. Three samples with different O/N content were obtained after 11 h, 48 h and 72 h of the ammonolysis.

According to the XRPD results (Fig. 5.1C), a perovskite-type single phase oxynitride is already obtained after 11 h of ammonolysis at T = 1073 K, whereas the formation of Mo₂N impurity phase was observed at higher temperatures.

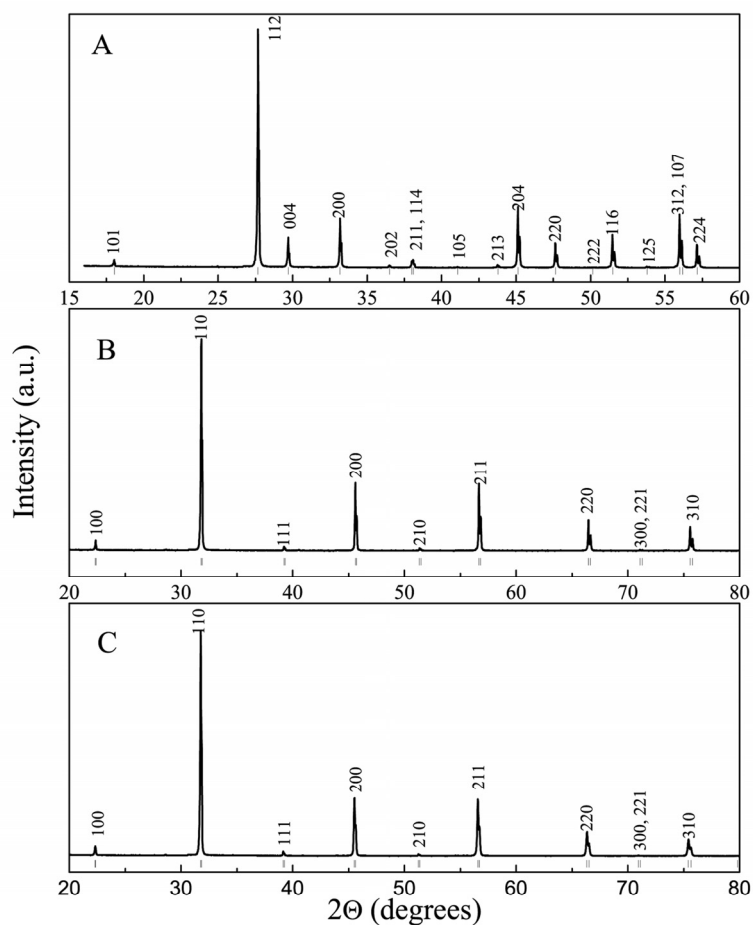


Figure 5.1. XRPD patterns confirming the phase purity of: A. SrMoO_4 after annealing at 1073 K for 4 hours. Space group: $I4_1/a$. The reflections are assigned according to the pdf entry 01-085-0809. B. SrMoO_3 ($Pm\bar{3}m$) obtained by the reduction of SrMoO_4 . C. SrMoO_2N ($Pm\bar{3}m$) obtained by thermal ammonolysis of SrMoO_4 .

The samples are of a dark-blue color. Similar to SrMoO_3 they are sensitive to the storing conditions. In particular, in contact with moisture they evolve ammonia and transform into SrMoO_4 within a period of a few months. Since the samples may also react with oxygen they were stored in dry N_2 after the synthesis.

The O/N content measured by hotgas extraction corresponds to the compositions $\text{SrMoO}_{1.95(5)}\text{N}_{1.05(5)}$, $\text{SrMoO}_{1.81(5)}\text{N}_{1.19(5)}$ and $\text{SrMoO}_{1.73(5)}\text{N}_{1.27(5)}$ for the compounds obtained after 11, 48 and 72 hours of ammonolysis, respectively. Hence, the nitrogen content of our samples is more than twice higher than reported before [48, 49]. The measured O/N content corresponds to a mixed oxidation state between +5/+6 for molybdenum. EDX reveals an average Sr:Mo ratio of all oxide and oxynitride samples equal to 0.98(1):1.02(2). Thus, within this method mistake (about 3 %) the obtained ratio is very close to the ideal ratio 1:1.

5.1.2. Structure and microstructure

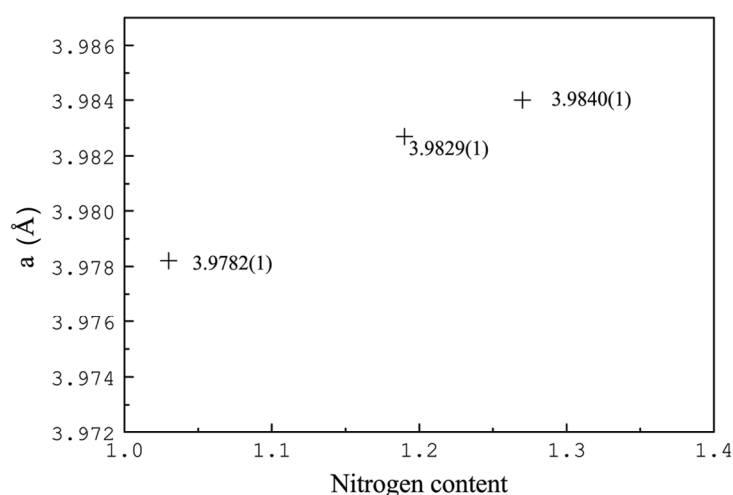


Figure 5.2. The influence of the nitrogen content (measured by hotgas extraction) on the lattice constants (refined from XRPD data) of the samples.

XRPD confirms the same space group $Pm\bar{3}m$ for SrMoO_3 and all the prepared oxynitride samples. The lattice parameter of SrMoO_3 refined from the XRPD data, $a = 3.9752(1) \text{ \AA}$, is in perfect agreement with the previously reported value of $3.9751(3) \text{ \AA}$ for the sample with anionic stoichiometry equal to 3. The dependence of the measured lattice constant from the nitrogen content of the oxynitride samples is shown in Fig. 5.2. The lattice parameter of the

sample treated for 11 h is 3.9782(1) Å, which is higher of that reported in the literature for SrMoO_{2.5}N_{0.5} (3.9773(1) Å) [49] and of SrMoO₃. Larger lattice constants were found for the samples with higher nitrogen content. Nitrogen insertion is expected to lead to an increase of the cell parameter since the effective ionic radius of N³⁻ (1.32 Å) is larger than that of O²⁻ (1.26 Å). On the other hand, oxidation of Mo⁴⁺ (0.79 Å) to Mo⁵⁺ (0.75 Å) and Mo⁶⁺ (0.73 Å) [35, 36] should lead to a decrease of the lattice constant. Although these two factors are expected to partly compensate each other, an increase of the lattice constant with the nitrogen content is measured, indicating that the influence of the larger anionic radius is the dominating effect.

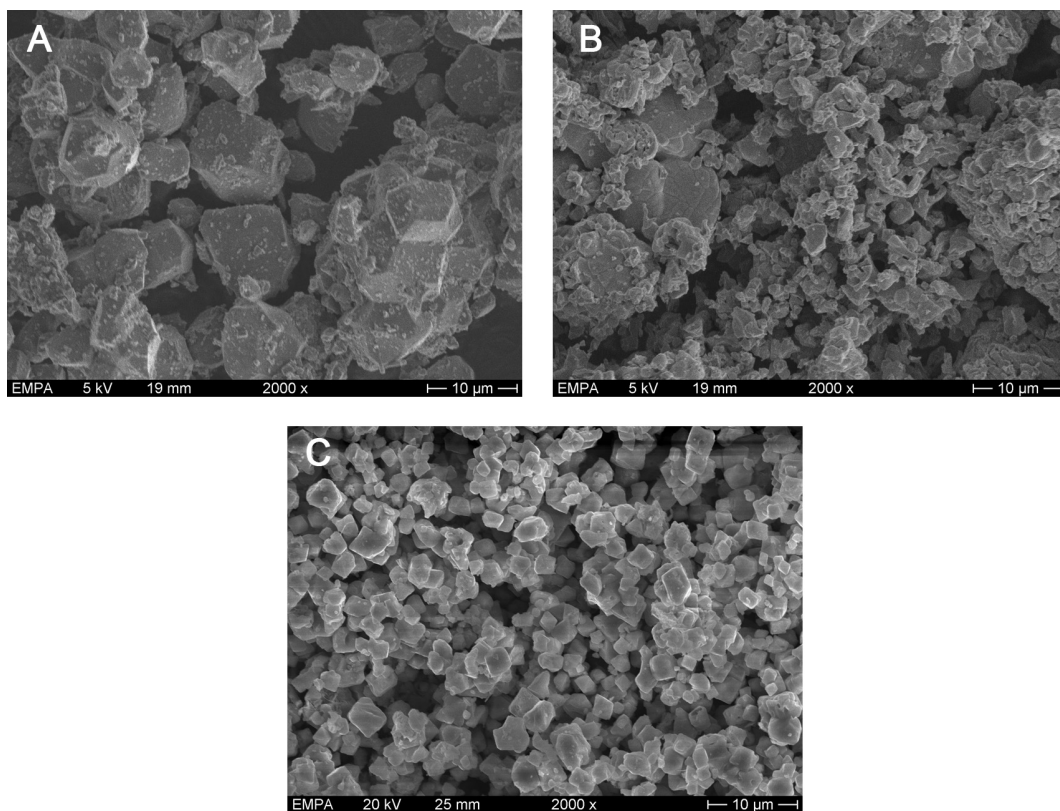


Figure 5.3. Microstructure of: A. SrMoO₄. B. SrMoO₃. C. 11 hours ammonia reacted SrMoO₄.

The microstructure of SrMoO₄, SrMoO₃ and of 11 hours ammonia treated sample is represented by 1-10 µm-size particles (Figure 5.3).

Perovskite-type compounds often possess pseudosymmetry which originates from a tilting of the BO₆-octahedra, while the cations occupy the same positions as in the cubic aristotype

structure. When the tilting is rather small it can not be probed by XRPD due to a low X-ray scattering power of anions. In contrast, the neutron scattering lengths of oxygen and nitrogen are large and therefore superstructure reflections, which occur due to the pseudosymmetry, are often intense. One example for such pseudosymmetry is SrNbO₂N, which, according to X-ray diffraction, crystallizes in a simple cubic perovskite structure, while ND revealed a tetragonal supercell [52]. Additionally, since oxygen and nitrogen are distinguishable with neutrons, ND allows to verify the O/N content measured by hotgas extraction.

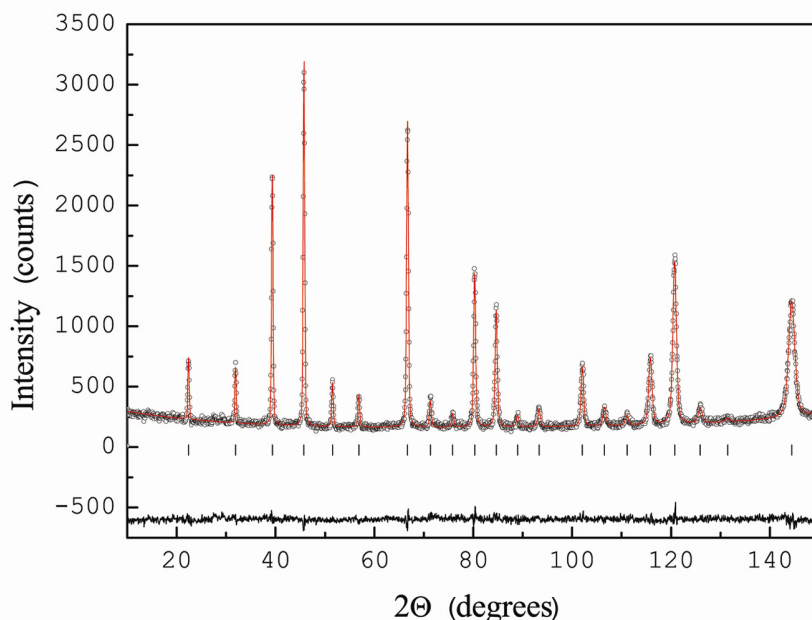


Figure 5.4. Rietveld refinement plot of the ND data for the 11 hours ammonolyzed sample.

Space group: $Pm\bar{3}m$, $a = 3.9835(1) \text{ \AA}$, $wR_p = 6.78$, $R_p = 5.20$, $\chi^2 = 1.36$

Rietveld refinement of the ND data collected from the 11 h ammonolyzed sample was carried out in the space group $Pm\bar{3}m$. In the starting structural model the Sr:Mo ratio was set to 1:1 (based on the cationic compositions study), whereas the O:N ratio was set to 2:1. Thermal displacement factors were refined isotropically for all atoms.

Table 5.1. Structural parameters of the SrMoO_{1.95}N_{1.05} refined from neutron powder data. Space group: ***Pm* $\bar{3}$ *m*** ($a = 3.9835(1)$ Å, $wR_p = 6.78$, $R_p = 5.20$, $\chi^2 = 1.36$).

Name	x	y	z	$B_{iso}, \text{Å}^2$	Occupancy factor	site
Sr	1/2	1/2	1/2	0.92(4)	1	1b
Mo	0	0	0	0.72(4)	1	1a
O/N(1)	1/2	0	0	0.64(2)	0.64(1)/0.36(1)	3d

The occupancy factors for oxygen and nitrogen were initially refined with the anionic site constrained to be fully occupied. In succeeding runs the occupancy factors of the anions were refined independently. Finally, the lattice and the profile parameters, $2\Theta_0$, the background coefficients, the thermal displacement factors and the anionic occupancies were refined together. Within the doubled standard deviation (2σ) no difference between the parameters obtained with the constrained and the unconstrained model were found. For this reason in the final refinement a complete occupation of the anionic sites was assumed and only the O/N ratio was refined. Refinements of the cationic occupancies gave no hints for the presence of the cationic vacancies. Summary of the structural parameters refined from the neutron data can be found in Table 5.1. The statistics of the refinement, the visual inspection of the fit (Fig. 5.4) and the refined values of the thermal displacement factors indicate that the chosen model is correct. The refined O/N content corresponds to the composition SrMoO_{1.89(2)}N_{1.11(2)}, which is in a reasonable agreement with the result obtained by hotgas extraction.

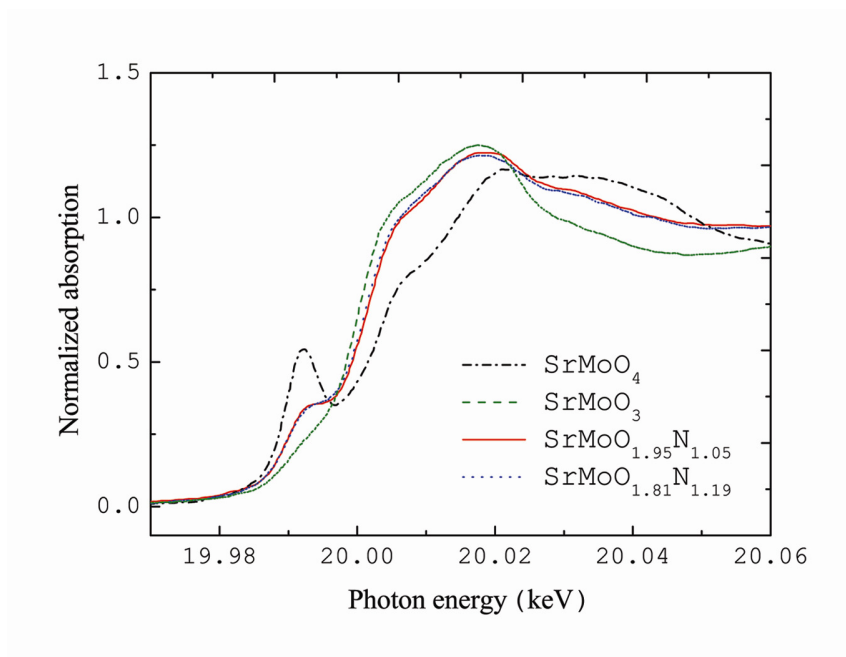


Figure 5.5. Normalized Mo K-edge XANES spectra of the oxynitrides in comparison to the SrMoO_3 and SrMoO_4 standards.

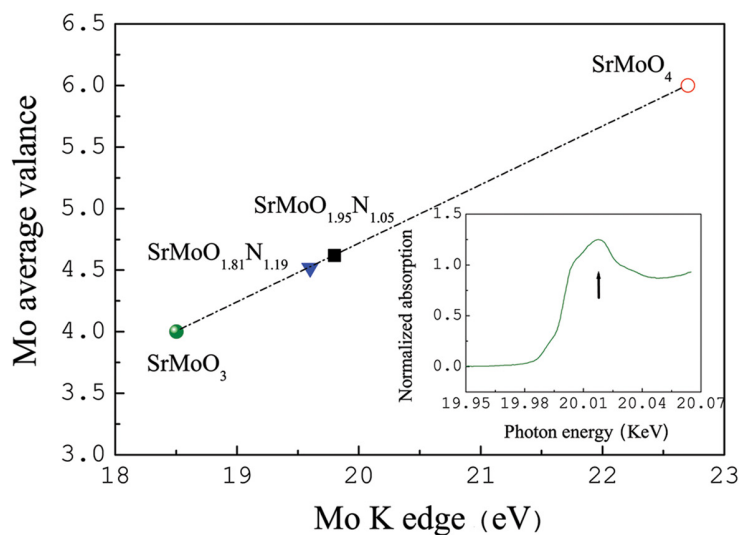


Figure 5.6. Linear relationship of average Mo valence and Mo K-edge position (relative to Mo metal) calculated from K-edge position of the standards SrMoO_3 and SrMoO_4 .

The Mo K-edge XANES spectra of SrMoO_3 , SrMoO_4 , $\text{SrMoO}_{1.95(5)}\text{N}_{1.05(5)}$ and $\text{SrMoO}_{1.81(5)}\text{N}_{1.19(5)}$, are shown in Figure 5.5. The edge shifts are obtained by using a well resolved feature above the absorption edge as shown in the inset of Figure 5.6, and are reported relative to the first inflection point in the Mo metal K-edge at 19.999 KeV [114]. The shift of the Mo K absorption edge to higher photon energies with respect to the metal standard gives information about the average valence of the Mo while the pre-edge features correspond to its coordination geometry [115].

The XANES spectrum of SrMoO_4 shows a strong pre-edge peak which arises from an allowed $1s - 4d$ electronic transition for tetrahedral symmetry [116]. This characteristic can also be observed as a shoulder for the oxynitrides with compositions $\text{SrMoO}_{1.95(5)}\text{N}_{1.05(5)}$ and $\text{SrMoO}_{1.81(5)}\text{N}_{1.19(5)}$. Since no SrMoO_4 impurity was detected with XRPD and ND, the feature most probably corresponds to a distortion in the octahedral oxygen environment of Mo – ions reported before for MoO_3 [115]. In the XANES spectrum of SrMoO_3 , where Mo is in a regular octahedron, this feature is not observed. Since for the oxynitrides no deviations from the cubic symmetry and no anomalous displacement parameters of their constituent ions have been detected by using ND (see Table 5.1), the local distortions in the surrounding of the Mo ions must have a too small coherence length to be detected with diffraction techniques. Most probably, the symmetry reduction arises from the different polarizabilities of O^{2-} and N^{3-} -ions, and their disordered arrangement around the Mo-ions. This interpretation is in accordance with recent EXAFS studies on BaTaO_2N , which reveal distorted octahedral arrangement of the Ta^{5+} -ions [117]. It should be noted that like in our case neither XRPD nor ND had given any hints on the possible deviation of the local symmetry from O_h . While diffraction methods give information on a long range ordering averaged over the whole sample, XAS is sensitive to the short-range surrounding of the respective element and therefore this method is well suited to detect local deviations from the average symmetry [118].

From the energy shift of the X-ray absorption edge, the oxidation state of transition metals can be derived [119]. Figure 5.7 depicts the calculated average Mo valence state for $\text{SrMoO}_{1.95(5)}\text{N}_{1.05(5)}$ (+4.62) and $\text{SrMoO}_{1.81(5)}\text{N}_{1.19(5)}$ (+4.52). On the other hand, the valence states obtained from the O/N content of these samples are +5.03 for $\text{SrMoO}_{1.95(5)}\text{N}_{1.05(5)}$ and

+5.19 for $\text{SrMoO}_{1.81(5)}\text{N}_{1.19(5)}$. This seeming discrepancy can be explained by the fact, that the absorption edge shift originates from both the "valence shift" (i.e. shift due to changing the oxidation state) and the "chemical shift" (shift due to different electronegativities of O^{2-} and N^{3-} - ligands). Since the oxide standards used are not able to account for differences in electronegativity of the anions, a big discrepancy between the calculated and the expected Mo valences arises.

5.1.3. High temperature physical properties

The measured Seebeck coefficient values for the synthesized samples are up to 3 times higher than those reported for SrMoO_3 ($S = 4\text{-}9 \mu\text{V K}^{-1}$) [86] but still close to those of metals. The Seebeck coefficient increases with increasing nitrogen content of the samples. The evolution of S with temperature and N content is shown in Figure 5.7.

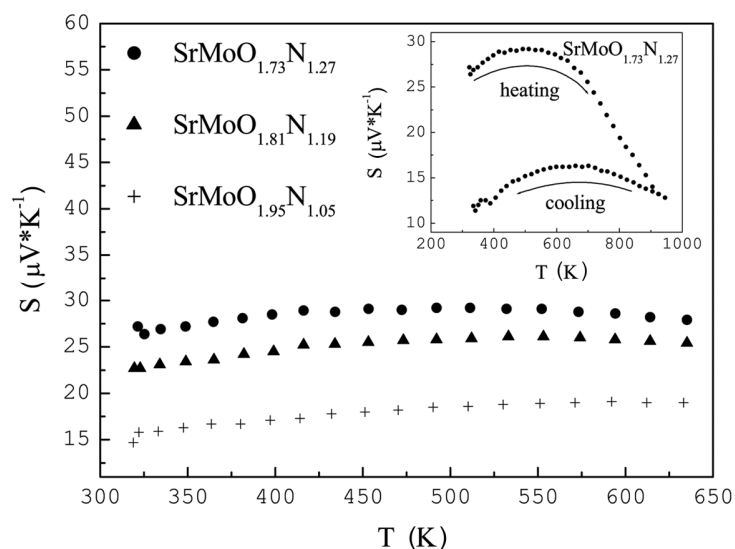


Figure 5.7. Temperature dependence of Seebeck coefficient of the oxynitrides. The inset shows an irreversible decrease of the measured values when samples were heated above their decomposition temperature.

Apparently, the values for all samples increase with temperature passing through a maximum at $T = 650$ K for $\text{SrMoO}_{1.95}\text{N}_{1.05}$, $T = 600$ K for $\text{SrMoO}_{1.81}\text{N}_{1.19}$ and $T = 550$ K for $\text{SrMoO}_{1.73}\text{N}_{1.27}$. Further heating of the samples is leading to the formation of metallic Mo impurity phase as revealed by XRPD and an irreversible decrease of the Seebeck coefficient. Thus, the temperature at which the maximum of the Seebeck is reached can be considered as decomposition temperature. Apparently, the formation of metallic Mo is connected with a nitrogen release from the samples. We have already reported similar behavior for Ca-substituted LaTiO_2N heated under N_2 (1 atm) [95]. The main driving force for the reduction of molybdenum is the formation of the very stable N_2 molecule (941 kJ mole^{-1}).

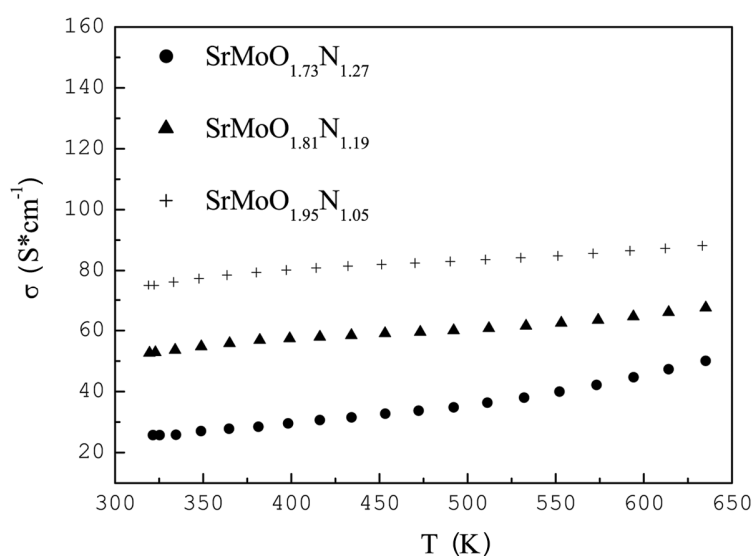


Figure 5.8. Temperature dependence of electrical conductivity of the oxynitrides.

The electrical conductivity of the samples decreases with increasing nitrogen content as shown in Figure 5.8. Contrary to the metallic SrMoO_3 the electrical conductivity of the oxynitrides increases with temperature, *i.e.* a semiconducting behavior is observed. The measured conductivity values are 3 orders of magnitude lower than those of SrMoO_3

($12.8 \times 10^3 \text{ S cm}^{-1}$) [86] and are of the same order of magnitude than those of $\text{SrMoO}_{2.6}\text{N}_{0.4}$ (66.7 S cm^{-1}) [48], but one order of magnitude higher than reported for $\text{SrMoO}_{2.5}\text{N}_{0.5}$ (2 S cm^{-1}) [49]. It should also be noticed that the temperature dependence of the $\text{SrMoO}_{2.6}\text{N}_{0.4}$ conductivity is semiconductor-like [48] similar to our samples, whereas that of $\text{SrMoO}_{2.5}\text{N}_{0.5}$ was described as metallic [49].

The power factor of the samples increases with temperature (Fig. 5.9). The measured values are lower than those reported for SrMoO_3 [120] due to the lower electrical conductivity of the oxynitrides.

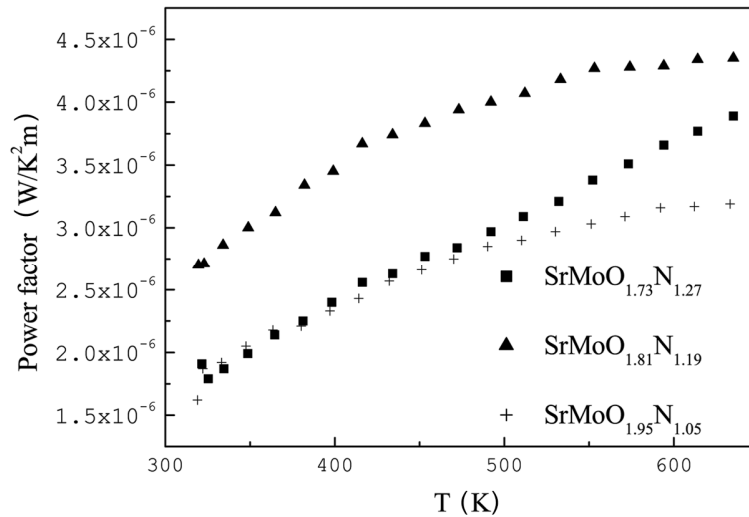


Figure 5.9. Variation of power factor of the oxynitrides samples with temperature.

The conductivity values and behavior of our samples are typical for semiconductors or poor metals. The density achieved for the ceramics (up to 89 % of the theoretical density) resembles the one reported for SrMoO_3 (90.8 %) [86]. Therefore, the observed high deviation between the conductivity values measured on our samples and reported for SrMoO_3 can not be attributed to the difference between the samples density. Another factor that can affect the conductivity and its temperature dependence is the composition of grain boundaries. Indeed, taking into account that the samples are air sensitive, it may happen that the grain surface partly reoxidizes during the handling and, thus, the measured slight

temperature dependence of the conductivity originates from the grain boundaries influence. The measured Seebeck values suggest that the synthesized samples are metallic-like.

5.1.4. Low temperature physical properties

Figure 5.10A shows temperature dependence of resistivity measured for SrMoO₃ and SrMoO_{1.95(5)}N_{1.05(5)} (further denoted to as SrMoO₂N). The measured resistivity of SrMoO₃ is significantly lower than the literature reported value (~5 μΩ cm) measured on the single crystal [121]. This implies an importance of the grain-boundary scattering processes during electrical transport of charge carriers of SrMoO₃. However, the measured sample shows metallic-like behavior of resistivity with temperature. Metallic nature of SrMoO₃ is also corroborated by its close to zero Seebeck coefficient (Figure 5.10B) value, which unlike the resistivity is related to the bulk property of the material. The Seebeck coefficient decreases continuously with temperature, which confirms holes to be the main charge carriers for SrMoO₃. The measured Seebeck values are close to the literature values [86, 120]. Figure 5.10C shows the variation of thermal conductivity with temperature. The values of thermal conductivity are about 3 times lower than those reported in reference [120], which is attributed to the lower density of our sample. As shown in Figure 5.11 the material exhibits a temperature independent paramagnetism ($\chi \sim 1.8 \cdot 10^{-4} \text{ emu mol}^{-1} \text{ K}^{-1}$) between T = 100-300 K. This is consistent with the absolute value of the magnetic susceptibility reported previously and explained as enhanced Pauli paramagnetism [49]. Below 100 K the magnetic susceptibility slightly increases, adopting the Curie behaviour superposed on the temperature independent background. Finally at T ~ 54 K a monotonous hyperbolic increase is interrupted by a weak anomaly.

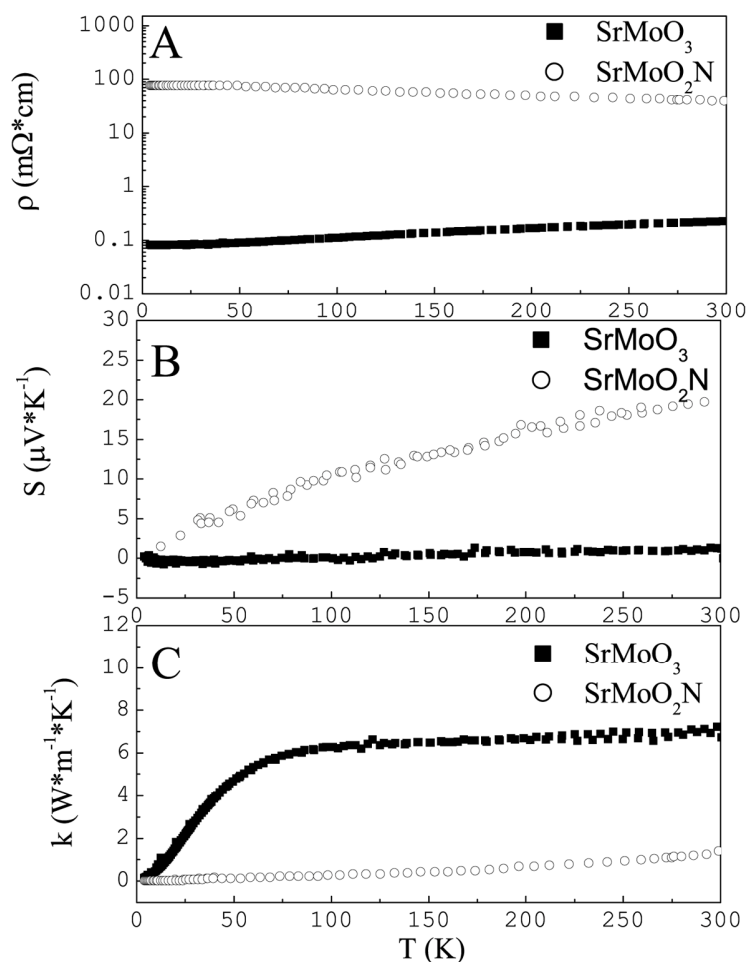


Figure 5.10. Temperature dependences of: A. Resistivity; B. Seebeck coefficient; C. Heat conductivity of SrMoO₃ and SrMoO₂N.

Unlike SrMoO₃, the measured SrMoO₂N shows semiconducting-like behaviour of its resistivity with temperature (Fig. 5.10A). Moreover, the absolute resistivity of SrMoO₃ is higher than that of SrMoO₂N. Based on the measured absolute Seebeck values it can be deduced that holes are predominating charge carriers of SrMoO₂N (Fig. 5.10B). The Seebeck values of SrMoO₂N are higher than those of SrMoO₃.

The measured thermal conductivity value of SrMoO₂N is one order of magnitude smaller than that of SrMoO₃ and it resembles the thermal conductivity of glass (Fig. 5.10C).

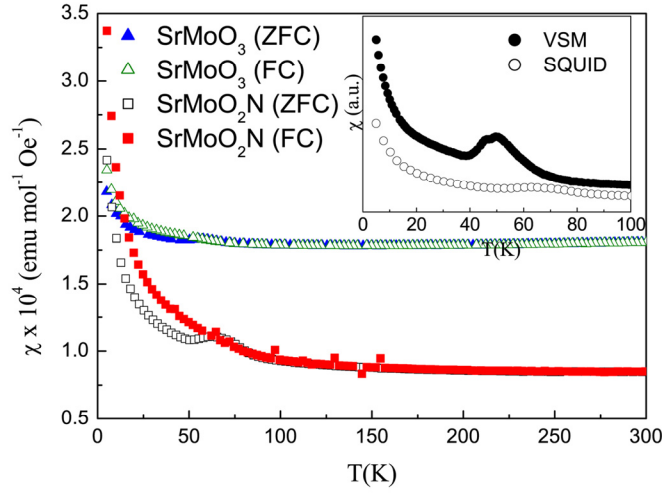


Figure 5.11. Molar magnetic susceptibility of SrMoO₃ and SrMoO₂N measured with SQUID. The inset shows expansion of the magnetic anomaly for SrMoO₃ when changing the magnetometer type from SQUID to VSM.

Similarly to SrMoO₃, SrMoO₂N oxynitride shows a temperature independent paramagnetism, low temperature upturn and anomaly at $T \sim 54$ K. The temperature independent component is, however, smaller than that of SrMoO₃ and the low temperature upturn and anomaly are enhanced. The magnetic data of SrMoO₂N can be fitted with the equation:

$$\chi = \chi_{P+L} + \frac{C}{T - \Theta}, \quad (5.1)$$

where

χ is the measured value of magnetic susceptibility (corrected for the sample holder, the varnish and diamagnetic contributions),

χ_{P+L} is the sum of the Pauli and Landau paramagnetic terms,

C is the Curie constant,

T is temperature,

Θ is the Weiss constant.

The fit gives $\chi_{P+L} = 8.5 \cdot 10^{-5} \text{ emu mol}^{-1} \text{ K}^{-1}$, $C = 3.3 \cdot 10^{-5}$ and $\Theta = -63 \text{ K}$. The obtained C value corresponds to the anti-ferromagnetic component with the effective magnetic moment of $\mu_{eff} = 0.05 \mu_B$, which is strongly reduced with respect to the expected spin-only value of 1.73 ($S = 1/2$). This suggests high level of electron delocalization in the system. Lower magnetic susceptibility confirms that the density of states at E_f is lowered in SrMoO_2N as compared to SrMoO_3 while the more pronounced low temperature features indicate (in coherence with difficult synthesis of SrMoO_2N) the higher contamination by paramagnetic impurities. The paramagnetic term χ_{P+L} can be expressed as:

$$\chi_{P+L} = \mu_B N D_F \left(1 - \frac{1}{3} \left(\frac{m}{m^*} \right)^2 \right), \quad (5.2)$$

where

D_F is density of states (DOS) at the Fermi level,

N is the number of itinerant electrons per one mole of unit formula,

m is the electron mass and

m^* is the effective electron mass.

Within the free electron approximation $m = m^*$ Hence:

$$\chi_{P+L} \approx 0.7 \mu_B N D_F \quad (5.3)$$

From this equation the susceptibility related DOS at the Fermi level can be obtained. Its value for SrMoO_2N is equal to $D_F = 25 \text{ Ry}^{-1}/\text{formula unit}$.

Alternatively, the DOS at the Fermi level can be calculated from the Sommerfeld parameter (γ), which is derived from the bulk-related heat capacity data.

The specific heat data for polycrystalline SrMoO_2N plotted as C_p / T versus T^2 follows a straight line below 10 K as it was reported before for SrMoO_3 [121]. Therefore, at this

region the data can be expressed by the sum of a linear term for the electronic (γT) and the lattice (βT^3) contributions:

$$C_p = \gamma T + \beta T^3, \quad (5.4)$$

where

$$\gamma = \frac{\pi^2}{3} k_B^2 N D_F \quad (5.5)$$

$$\beta = 12\pi^4 N k_B / 5\Theta_D^3, \quad (5.6)$$

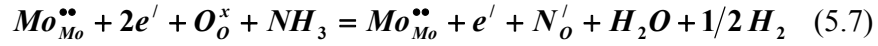
where

k_B is the Boltzmann constant,

Θ_D is the Debye temperature.

The fitting of the Equation 5.4 results in $\gamma = 3.86 \text{ mJ mol}^{-1} \text{ K}^2$ and $\Theta_D = 318.9 \text{ K}$. The value of γ corresponds to the DOS of $D_F = 22.3 \text{ Ry}^{-1}/\text{formula unit}$. This close to the χ_{P+L} -derived DOS value evidences on the absence of strong electronic correlations in the system (Wilson ratio $R_W \approx 1$). The literature value of γ for SrMoO_3 ($7.9 \text{ mJ mol}^{-1} \text{ K}^2$) [121] is higher than that of SrMoO_2N , hence the DOS at the Fermi level of SrMoO_3 (D_F of $45.0 \text{ Ry}^{-1}/\text{formula unit}$) is higher than that of SrMoO_2N . Besides, to conclude about the influence of the anionic substitution on the magnetic correlations of the $\text{SrMoO}_{3-x}\text{N}_x$ system, the Wilson ratio of SrMoO_2N should be compared with that of SrMoO_3 . From Equation 5.3 we obtain the DOS of $53.0 \text{ Ry}^{-1}/\text{formula unit}$ for SrMoO_3 . Thus, the Wilson ratio of SrMoO_3 $R_W \approx 1.1$. Hence, this material is essentially free from magnetic correlations.

Lower density of states at E_f for SrMoO_2N is consistent with an expected increase in the formal Mo oxidation state, *e.g.* the removal of electrons from the itinerant t_{2g} states of Mo-ions, when part of O^{2-} in SrMoO_3 is replaced with N^{3-} :



Together with the anionic composition refined from the neutron diffraction data this points to the fact that an increase of the molybdenum oxidation state is the main charge compensating mechanism for partial substitution of O^{2-} with N^{3-} .

The evaluation of the influence of the anionic substitution of SrMoO_3 on the charge carrier mobility has to be related to the electrical resistivity and thermal conductivity data. Semiconducting-like behaviour with low electrical resistivity reveal a low charge carriers mobility for SrMoO_2N . It can be caused by one or the combination of the following factors:

1. Creation of charge carrier traps due to the occupation of the same crystallographic site by atoms with different charge and electronic level positions or Mo-(O,N)₆ octahedra distortion as revealed by XANES;
2. Dominating role of the charge carriers scattering at grain boundaries in the electronic and heat transport processes.

From lower thermal conductivity and higher electrical conductivity values of SrMoO_2N compared to those of SrMoO_3 it follows that the mobility decrease has a dominating influence over the charge carrier concentration on the charge-carrier transport as compared to the influence of the charge carriers concentration.

The anomaly measured at $T \sim 54$ K apparently, can not be associated with partial substitution of O^{2-} with N^{3-} . The same magnetic feature can be noted on the magnetic susceptibility curves of SrMoO_3 and Sr_2MoO_4 published previously [122, 123]. Although, no explanations is given in [122], the authors of [123] has attributed the feature to molecular oxygen.

It is known that oxygen can significantly influence magnetic susceptibility data [124]. Bulk oxygen melts at $T = 54.4$ K and a paramagnetic γ -phase transforms into the

antiferromagnetic β -phase at $T = 43.8$ K. Residual oxygen in the measurement chamber or in the sample can give a signal on the susceptibility curves. Here, a comparative magnetic measurement performed with another instrument is used to establish the presence of molecular oxygen.

Magnetic susceptibility of the same samples was measured under the same magnetic field additionally with a VSM PPMS option. From Figure 5.11 (inset) it is clearly seen that the measurement with VSM gives a sufficiently expanded magnetic signal with 2 maxima at $T \sim 47$ K and 54 K respectively. Thus, the maximum at $T \sim 54$ K corresponds to the melting point of oxygen and the maximum at 47 K to the β - γ – transformation of solid oxygen. The measurement of an empty sample holder did not reveal any anomalies. Thus, the measured signals result from molecular oxygen in the samples and not in the holder. At present, it is difficult to conclude where molecular oxygen is located: on the measured samples surface, in pores between grains or within grains.

Physical properties of the oxygen confined in pores or adsorbed by the sample surface dramatically differ from those measured on bulk oxygen samples. For example, physical properties of the oxygen confined in pores depend upon the pores size distribution, filling and internal pressure [125-128].

Finally, three possible explanations can be given for Curie paramagnetism measured below 50 K:

1. It is related to intrinsic property of the material and can be concerned with the presence of electronic defects (like Mo'_{Mo}) as it was found before for $SrVO_3$;
2. Presence of a x-ray amorphous paramagnetic impurity phase;
3. Paramagnetism of γ -oxygen, confined in pores of the measured material.

5.1.5. Conclusions

Solid solutions of the general composition $SrMoO_{3-x}N_x$ with $x > 1$ were successfully synthesized by thermal ammonolysis of $SrMoO_4$. The nitrogen content of our samples is more than twice higher than previously reported and is confirmed by both ND and hotgas extraction measurements. XANES study reveals a lower oxidation state of Mo with respect to the value calculated from the nitrogen content, originating from a higher covalency of

the Mo-N bond compared to the Mo-O bond ("chemical shift"). Both XRPD and ND reveal no deviations from the cubic perovskite structure for the synthesized compounds, whereas local distortions of the Mo(O,N)₆ octahedra are detected with XANES. These distortions may arise due to the different polarizabilities of O²⁻ and N³⁻ and anionic disorder. Seebeck values of the oxynitrides are similar to those of metals. Smaller values of electrical conductivity of our samples compared to those of SrMoO₃ are measured.

Low temperature physical properties of cubic perovskite phases, SrMoO₂N and SrMoO₃, have been investigated in the temperature range of 5 K < T < 300 K on the polycrystalline samples. These materials are *p*-type conductors as deduced from the Seebeck coefficient measurements. Both compounds show paramagnetism dominated by the Pauli term. Lower magnetic susceptibility and gamma-coefficient γ of the oxynitride confirm simultaneously lower density of states near the Fermi level of SrMoO₂N as compared to that of SrMoO₃ according to the higher valence of Mo in SrMoO₂N. Together with the anionic composition refined from the neutron diffraction data and obtained by hotgas extraction, this points to the fact that an increase of the molybdenum oxidation state is the main charge compensating mechanism for partial substitution of O²⁻ with N³⁻. Comparison of the DOS values derived from the magnetic susceptibility and heat capacity measurements confirms the absence of electronic correlations in the SrMoO₂N material.

In contrast to the corresponding oxides the oxynitride samples reveal low thermal conductivity and semiconducting-like electrical resistivity. This can be attributed to the frustrated electronic structure of SrMoO₂N (*e.g.* due to the Mo-(O,N)₆ octahedra distortion).

The presence of molecular oxygen in the measured materials is responsible for the magnetic anomaly observed at T ~ 54 K, contrary to previously suggested antiferromagnetic or spin-glass transitions. It is also assumed that paramagnetic oxygen contributes to the observed increase of the magnetic susceptibility at low temperatures.

5.2. CaMo(O,N)₃ and BaMo(O,N)₃. Phase formation, structural and microstructural characterization of novel oxynitride-perovskites.

5.2.1. Synthesis of starting oxides

BaMoO₄ was prepared according to the procedure described in [129]. A 0.1 M solution of Ba(NO₃)₂ (Merck, purity > 99.0 %) was poured slowly with constant stirring into a 0.1 M solution of Na₂MoO₄ (Riedel-de Haän, purity > 99.5 %). The formed precipitate was washed several times with deionized water and calcined at 1073 K during 4 hours.

BaMoO₃ was obtained by reduction of BaMoO₄ (1 g) with a forming gas (5% of H₂ in N₂) flow of 300 mL min⁻¹. The reduction was carried out at T = 1473 K during 15 hours in a tubular quartz reactor with an internal diameter of 30 mm.

CaMoO₄ was synthesized by the citrate method [90]. Stoichiometric amounts of H₂₄Mo₇N₆O₂₄*4H₂O (Fluka, > 99.0 %) and CaCO₃ (Alfa Aesar, > 99.5 %) were dissolved in an aqueous 0.1 M citric acid C₆H₈O₇ (Riedel-de Haän, > 99.5 %) solution. The amount of citric acid was 3 times higher than the total molar amount of Mo and Ca. The obtained solution was predried at 393 K overnight and heated up to 873 K within 12 hours. The final product was then heated from 873 K to 1073 K with a heating rate of 5 K min⁻¹, calcined at that temperature during 2 hours and cooled down to room temperature.

CaMoO₃ was synthesized by reduction of CaMoO₄ produced by the citrate method with forming gas (5% of H₂ in N₂) [90]. The reduction of 1 g of CaMoO₄ was carried out at 1173 K during 12 hours (with an intermediate regrinding after 4 h and 8 h of the reaction) under a forming gas flow of 100-300 mL min⁻¹ in a quartz reactor with an internal diameter of 30 mm [95]. Forming gas was supplied through a quartz tube with a diameter of 5.8 mm placed above the sample and about 2 mm from the reactor end. After the reaction, the sample was quenched down to room temperature within 1 minute.

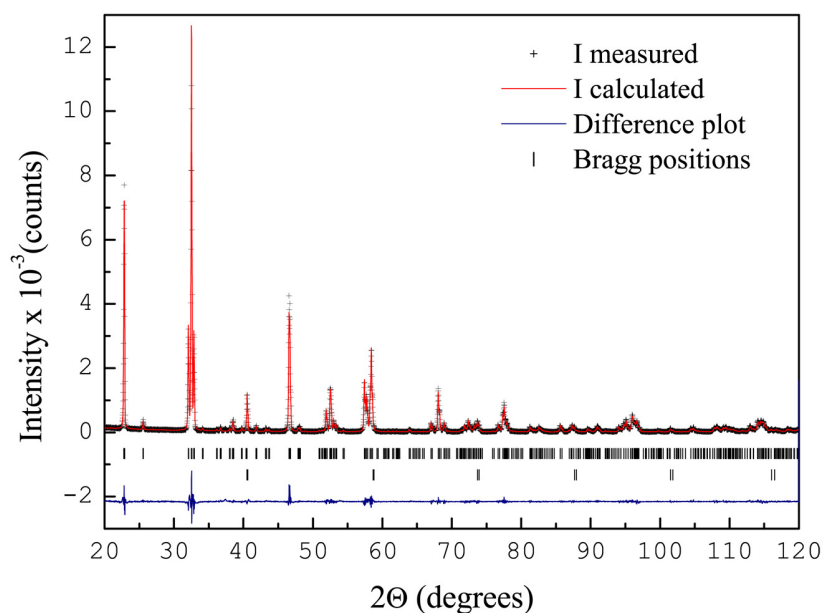


Figure 5.12. Rietveld refinement plot of the x-ray powder diffraction data for CaMoO_3 . Space group: $Pbnm$. The observed intensities, calculated profile, difference curve and Bragg positions are shown. Mo has been included as a minor impurity phase in the refinement

XRPD confirmed phase purity of all the synthesized oxides, except of CaMoO_3 , for which a Mo impurity of 2.3 weight % was refined. Crystallographic parameters of CaMoO_3 as obtained by refinement of the XRPD data (Figure 5.12) in space group $Pbnm$ are summarized in Tables 5.2 and 5.3 and are in a good agreement with a previous neutron diffraction study of this compound [90]. The observed isotropic line broadening was accounted for by refining isotropic size-strain components (in Fullprof referred to as U and Y) of the sample intrinsic profile. Their refined values correspond to an apparent size value of 0.13 μm and an apparent strain value of 0.31 %.

The refined lattice parameter of BaMoO_3 is equal to 4.0409(1) \AA , which is close to the value of 4.0404(3) \AA reported in reference [86]. No line broadening was found for this oxide with respect to the used standard LaB_6 .

Both CaMoO_3 and BaMoO_3 are of a purple-red color. In contact with moisture they oxidize into corresponding CaMoO_4 and BaMoO_4 . Therefore they were stored under dry nitrogen atmosphere.

5.2.2. General procedure for the ammonolysis of molybdates

All the synthesized oxides were reacted with ammonia gas (PanGas, 99.999 %, 100 mL min^{-1}) at $873 \text{ K} < T < 1123 \text{ K}$. The reactions were carried out each 25 K in an Al_2O_3 reactor with an internal diameter of 30 mm. Each sample load was 0.1 g. The reaction time was 20 h. Ammonia was supplied by means of a quartz tube with a diameter 5.8 mm placed above the sample. Heating and cooling rates were 10 K min^{-1} .

5.2.3. Thermal ammonolysis study of AMoO_4 ($A = \text{Ca}^{2+}, \text{Ba}^{2+}$)

X-ray powder diffraction patterns of BaMoO_4 reacted with ammonia at different temperatures can be seen in Fig. 5.13. Reflections corresponding to $\text{Ba}_3\text{Mo}_2\text{O}_6\text{N}_2$ [62, 130] and BaMoO_4 are identified for the sample reacted at 898 K for 24 hours (Fig. 5.13B). The BaMoO_4 main reflections disappear upon heating the sample up to 973 K. XRPD confirms $\text{Ba}_3\text{Mo}_2\text{O}_6\text{N}_2$ to be the main phase formed after the ammonolysis at $T = 973 \text{ K}$.

Some additional reflections belonging to a phase, indexed as a cubic perovskite with the lattice parameter larger than that of BaMoO_3 are also resolved (Fig. 5.13C). Those reflections are attributed to a nitrated BaMoO_3 (further referred to as $\text{BaMo}(\text{O},\text{N})_3$). The reflections of this phase disappear after 48 h of the ammonolysis at $T = 973 \text{ K}$ and only reflections of $\text{Ba}_3\text{Mo}_2\text{O}_6\text{N}_2$ can be resolved. On the XRPD pattern of the sample, which was reacted with ammonia at 1023 K, Mo_2N and $\text{Ba}_3\text{Mo}_2\text{O}_6\text{N}_2$ are the main identified phases. Two weak reflections, which belong to an unidentifiable phase, appear between the (015) and (110) reflections of $\text{Ba}_3\text{Mo}_2\text{O}_6\text{N}_2$ (Fig. 5.13D). Thus, $\text{BaMo}(\text{O},\text{N})_3$ is not formed as a main phase from BaMoO_4 under the chosen reaction conditions.

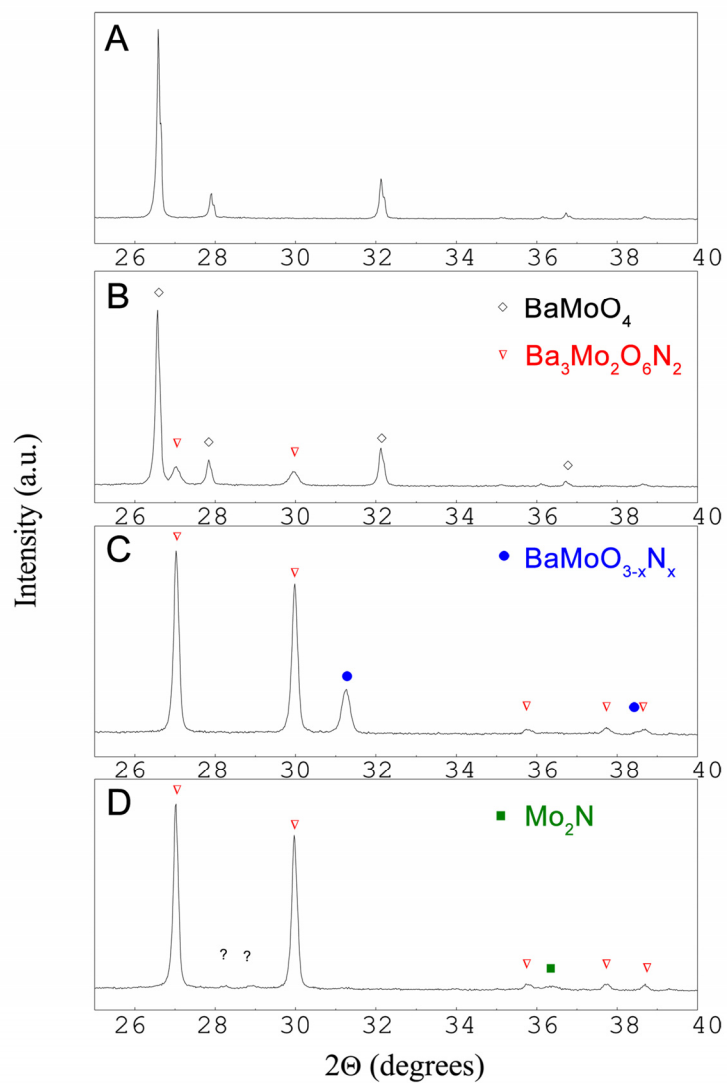


Figure 5.13. XRPD: A. Pure BaMoO_4 ; B. After the 20 h reaction with NH_3 at $T = 898\text{ K}$; C. After the 20 h reaction with NH_3 at $T = 973\text{ K}$; D. After the 20 h reaction with NH_3 at $T = 1023\text{ K}$

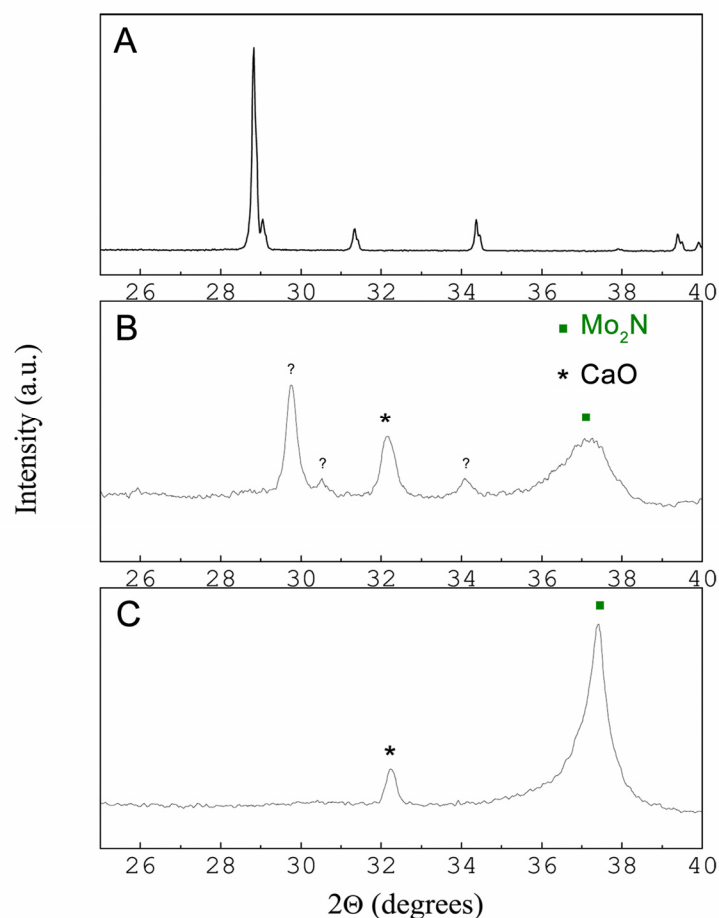


Figure 5.14. XRPD: A. Pure CaMoO_4 ; B. After the 20 h reaction with NH_3 at $T = 898 \text{ K}$; C. After the 20 h reaction with NH_3 at $T = 973 \text{ K}$

The reaction between CaMoO_4 (Fig. 5.14A) and ammonia starts at 873 K. The XRPD patterns reveal the appearance of broad features coincident with the main reflections of Mo_2N [131]. At 898 K CaO and Mo_2N can be identified. Some additional reflections that could not be assigned to any known phase appear at that temperature (Fig. 5.14B). The XRPD pattern of the sample reacted with NH_3 at higher temperatures reveals the presence of the CaO and Mo_2N (Fig. 5.14C). Thus, $\text{CaMo}(\text{O},\text{N})_3$ can not be prepared directly from CaMoO_4 under the chosen reaction conditions.

5.2.4. Thermal ammonolysis study of $A\text{MoO}_3$ ($A = \text{Ca}^{2+}, \text{Ba}^{2+}$)

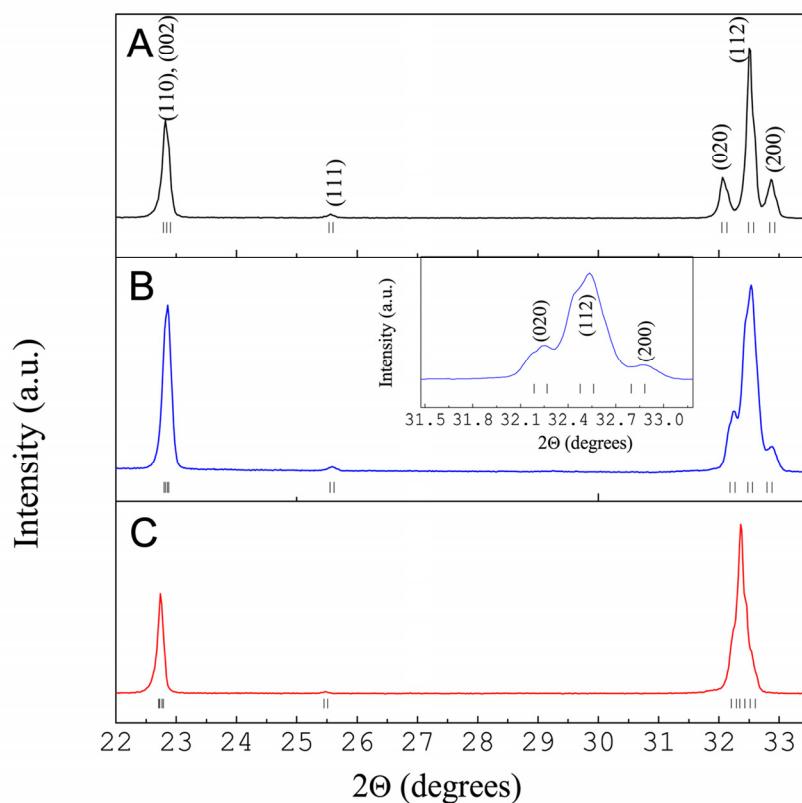


Figure 5.15. Evolution of the XRPD profile with time measured during the ammonolysis of CaMoO_3 at $T = 898 \text{ K}$: A. Non-reacted sample; B. The sample after the 50 h reaction (the inset shows the splitting of the main reflections due to the non-uniform O/N distribution through the particles depth); C. The sample after the 100 h reaction

A noticeable interaction between CaMoO_3 (Fig. 5.15A) and NH_3 starts at 898 K. The ammonolysis results in a perovskite-type phase with cell parameters deviating from the ones of the starting oxide. Its formation can best be monitored by inspection of the (200), (020) and (002) located roughly between 32 and 33° 2θ. During the reaction the (002) and (200) reflections are shifted to lower angles, whereas the (020) reflection is shifted to higher angles. This indicates an increase in a and c , but a decrease in the b parameter of the

unit cell. As can be seen from Figure 5.15B a broadening of the diffraction peaks occurs at the early stages of the ammonolysis. A closer examination reveals the splitting of the reflections (see the inset of Fig. 5.15B). At that stage the pattern can be fitted assuming two perovskite type phases (*Pbnm*) of different lattice parameters and atomic coordinates, corresponding to $\text{CaMo}(\text{O,N})_3$ samples with different anionic composition. The kinetics of oxygen exchange with nitrogen is slow due to the low synthesis temperature.

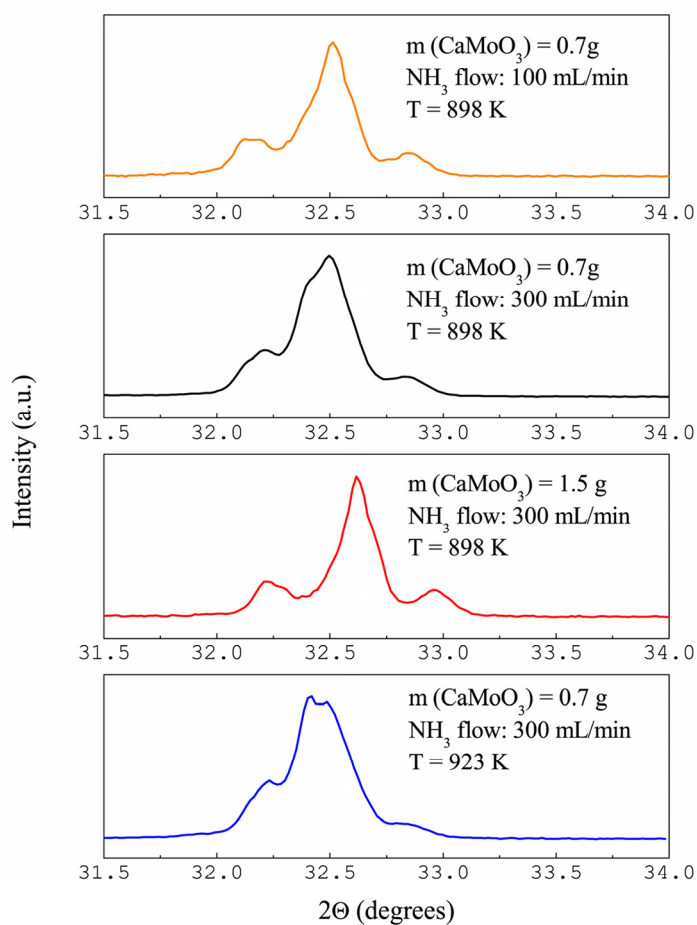


Figure 5.16. XRPD study on the influence of the sample mass, ammonia flow and temperature on the kinetics of the $\text{CaMo}(\text{O,N})_3$ phase formation. Smaller sample mass, increasing temperature and/or ammonia flow promotes faster formation of the oxynitride phase

The reaction rate of the oxynitride phase formation enhances with increasing temperature, increasing ammonia flow and/or decreasing sample mass (Fig. 5.16). The formed oxynitride phase (Fig. 5.15C) is stable under ammonia up to $T = 923$ K. A further increase of temperature leads to the formation of Mo_2N and CaO impurities.

The sample batch used for the crystallographic investigation by Rietveld refinements was obtained by ammonolyzing 0.7 g of CaMoO_3 at $T = 898$ K during 100 hours (when the main reflections splitting disappeared and no further change in the lattice parameters was detected by XRPD) under an ammonia flow of 300 mL min^{-1} . After the reaction the sample was quenched to room temperature within one minute. Increasing the synthesis temperature $T > 898$ K led to the oxynitride phase with lower nitrogen content as deduced from the Bragg reflection positions measured by XRPD. The explanation for this is given further in the text.

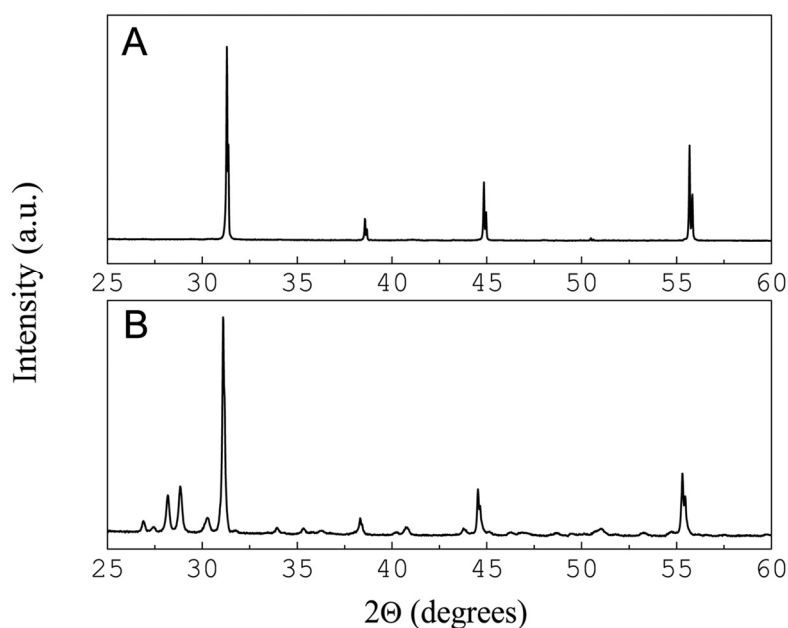


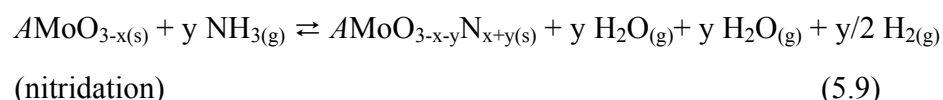
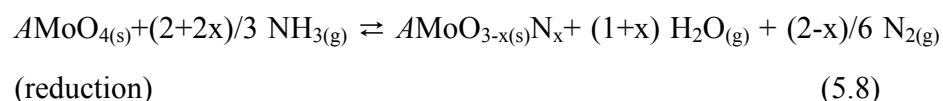
Figure 5.17. Thermal ammonolysis study of BaMoO_3 : A. Pure BaMoO_3 ; B. The sample reacted with NH_3 at $T = 998$ K during 85 h (the shift of the perovskite phase reflections to lower angles can be seen)

The ammonolysis of BaMoO₃ (Fig. 5.17A) proceeds similar to that of CaMoO₃. The temperature had to be raised up to 998 K and the sample mass had to be decreased down to 0.25 g in order to promote a faster formation of the oxynitride phase. As in case of the CaMoO₃ ammonolysis a broadening of the perovskite-phase reflections and their shift to lower angles is observed. This indicates the formation of the oxynitride-perovskite phase BaMo(O,N)₃ with a larger lattice constant compared to BaMoO₃. However, the formation of the secondary phase is simultaneously observed (Fig. 5.17B). Some of the reflections were assigned to Mo, BaO and Ba₃Mo₂O₆N₂ phases. However, we could not attribute the main impurity phase reflections, which are coincident with those of the phase formed during the ammonolysis of BaMoO₄ at 1023 K (Fig. 5.13D), to any phase of the Ba-Mo-O-N system found in ICSD (inorganic crystal structure database) and Pdf-2 (powder diffraction files) databases. Therefore, we conclude, that they belong to a previously undiscovered phase of the Ba-Mo-O-N system. The broadening of BaMo(O,N)₃ reflections decreases with time. It has to be noted that while the ammonolysis of BaMoO₄ leads to the minor amount of the BaMo(O,N)₃ phase, the ammonolysis of BaMoO₃ leads to a considerable BaMo(O,N)₃ yield.

Both CaMo(O,N)₃ and BaMo(O,N)₃ possess a dark blue color. The materials are moisture sensitive. Therefore, they were stored under the same conditions as CaMoO₃ and BaMoO₃.

5.2.5. Discussion of the thermal ammonolysis results

During its reactions with *AMoO*₃ and *AMoO*₄ oxides NH₃ can act as a nitriding and a reducing agent:



At $T > 573$ K ammonia undergoes considerable dissociation:



The formed hydrogen can also further reduce $\text{AMoO}_4/\text{AMoO}_3$ oxides. Depending on the relative rates of the processes described above a more nitrated or more reduced product will be formed. As it is mentioned in [40] to achieve effective nitridation the dissociation of ammonia should be minimized before it reaches the sample's surface. Otherwise, reduction may dominate over nitridation. That is why it is important to increase the ammonia flow with temperature [40]. Additionally, increasing ammonia flow promotes faster water removal [44, 45] and the renewal of active nitriding species over the sample. These factors can account for the enhanced kinetics of the oxynitride phase formation observed during the ammonolysis of AMoO_3 when increasing the ammonia flow. Partial dissociation of ammonia away from the sample's surface, when increasing temperature explains the formation of the $\text{CaMo}(\text{O},\text{N})_3$ oxynitride phase with lower nitrogen content as was found during the present study.

Besides the ammonia flow rate, the structure of the starting precursor and the ionic radius of the A -site cation and the covalence of the Mo-(O/N) bonding influence the oxynitride phase formation.

A detailed study on the Mo – oxidation state stability of AMoO_4 and AMoO_3 ($A = \text{Ca}^{2+}$, Sr^{2+} , Ba^{2+}) against reduction is available from the work of Kamata *et al.* [89, 91]. The authors reported that the alkaline-earth cation with a larger ionic radius provides better stabilization of the Mo - oxidation state in AMoO_3 and AMoO_4 . The influence of the A -site cation ionic radius on the Mo-oxidation state stability was discussed in terms of the positive inductive effect. The strength of the positive inductive effect of a cation is related with its polarizing power [6]. The latter is inversely proportional to the ionic radius of the cation. Hence, within one group of the Periodic Table the strength of the positive inductive effect decreases with decreasing the ionic radius of the element. Thus, for Ca^{2+} , Sr^{2+} and Ba^{2+} the strength of the positive inductive effect decreases with the sequence $\text{Ba}^{2+} > \text{Sr}^{2+} > \text{Ca}^{2+}$. In the same sequence the ability of the alkaline-earth to retain the Mo-ion oxidation state

decreases. Indeed, during the ammonolysis of $AMoO_4$ the increase of the Mo-oxidation state in the main product phase with the increase of the A -site cation ionic radius is observed.

Apart from the ammonia flow and the positive inductive effect, the influence of the lattice energy and structure distortion energy on the phase formation during the ammonolysis has to be considered.

Apparently, $AMoO_3$ undergoes fewer structural changes during the ammonolysis than $AMoO_4$. The lattice stability of $AMoO_3$ is higher than of $AMoO_4$. This is the most probable explanation for the differences in the phase formation observed during the ammonolysis of $AMoO_4$ and $AMoO_3$ (with the equal A - site cation).

The tolerance factor (t) expresses the degree of distortion of the perovskite structure (ABX_3). It is calculated by dividing the $A - X$ distance by the $M - X$ distance times square root of two:

$$t = \frac{\langle A-X \rangle}{\sqrt{2} \langle B-X \rangle} \quad (5.11)$$

The deviation of t from 1 is proportional to the structure distortion energy, which is a part of the total energy of a compound. The higher the distortion energy, the less favored is the formation of the perovskite structure. Thus, different tolerance factors of $AMoO_3$ compared to those of the corresponding oxynitrides can explain whether substitution of oxygen with nitrogen leads to the less distorted and thus, more stable structure. Tolerance factors of $CaMo^{4+}O_3$, $SrMo^{4+}O_3$ and $BaMo^{4+}O_3$ calculated from ionic radii of the constituent ions [35, 36] are 0.95, 0.98 and 1.03 correspondingly, whereas for the corresponding oxynitrides, for example, $CaMo^{6+}ON_2$, $SrMo^{6+}ON_2$ and $BaMo^{6+}ON_2$ they are equal to 0.97, 1.01 and 1.05. According to these values the substitution of O^{2-} with N^{3-} in $CaMoO_3$ and $SrMoO_3$ reduces the structure distortion energy. Thus, the substitution is favorable for the perovskite structure formation. On the other hand, for $BaMoO_3$ partial substitution of O^{2-} with N^{3-} would lead to a more distorted structure. Therefore, it can be expected that formation of the phase pure $BaMo(O,N)_3$ at ambient pressure will be difficult, which is in an accordance with our experiments.

It has to be noted, that only the tolerance factor consideration, which in many cases is sufficient to compare crystal structures stability of perovskite-type oxides or fluorides (e.g. materials with predominantly ionic type of bonding) may not be enough to compare crystal structure stability of an oxide with that of the corresponding oxynitride. Indeed, higher covalence of the Mo-N bonding as compared to that of the Mo-O bonding makes the Mo-(O,N)₆ octahedra more flexible to distort. Even, if this type of distortion occurs only locally, it may sufficiently reduce the structure distortion energy.

It is worthy to compare our results on the ammonolysis of BaMoO₄ and BaMoO₃ with those reported by Liu *et al* [48]. Here the formation of the perovskite-oxynitride phase BaMo(O,N)₃ during the ammonolysis of both BaMoO₃ and BaMoO₄ can be observed, while the authors of ref. [48] reported that they were not able to convert BaMoO₃ and BaMoO₄ into BaMo(O,N)₃. This can be explained by the difference in the ammonia chemical potential which originates from the different ammonia flow used during the studies as discussed above.

5.2.6. Crystal structures of CaMoO₃, CaMo(O,N)₃ and BaMo(O,N)₃

So far, only little information on the crystal structure of the perovskite-type CaMoO₃ is available in literature. Based on XRPD data a monoclinic symmetry was proposed for that material [89]. In contrast, de la Calle *et. al* [90] suggested an orthorhombic symmetry with the space group ***Pbnm*** based on the results of neutron diffraction data refinement. An alternative monoclinic symmetry was not yet tested. Most of both CaMoO₃ and CaMo(O,N)₃ crystallites analyzed by means of selected area electron diffraction (SAED) exhibit complicated electron diffraction (ED) pattern due to the presence of twin-domains. In such a case, different twin orientations superposed by double diffraction make the observation of the extinctions discarding glide planes and screw axis difficult. Here, to choose between the possible space groups x-ray diffraction was used additionally.

We consider two space groups, which were found to fit the XRPD data of CaMoO₃ and CaMo(O,N)₃ with close values of the fit quality indicators: orthorhombic ***Pbnm***, and monoclinic ***P2₁/n***, based on the unit cells $\sqrt{2}a_p \times \sqrt{2}a_p \times 2a_p$ and $\sqrt{2}a_p \times 2a_p \times \sqrt{2}a_p$ (a_p = cubic perovskite lattice parameter), respectively.

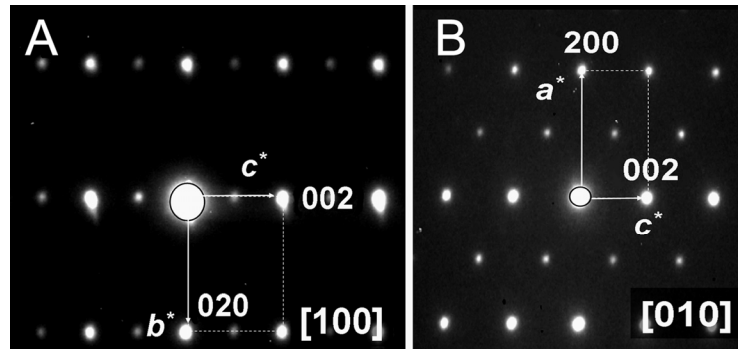


Figure 5.18. Electron diffraction patterns for $\text{CaMo}(\text{O},\text{N})_3$ taken along the A. $[100]$ and B. $[010]$ orthorhombic zone axis

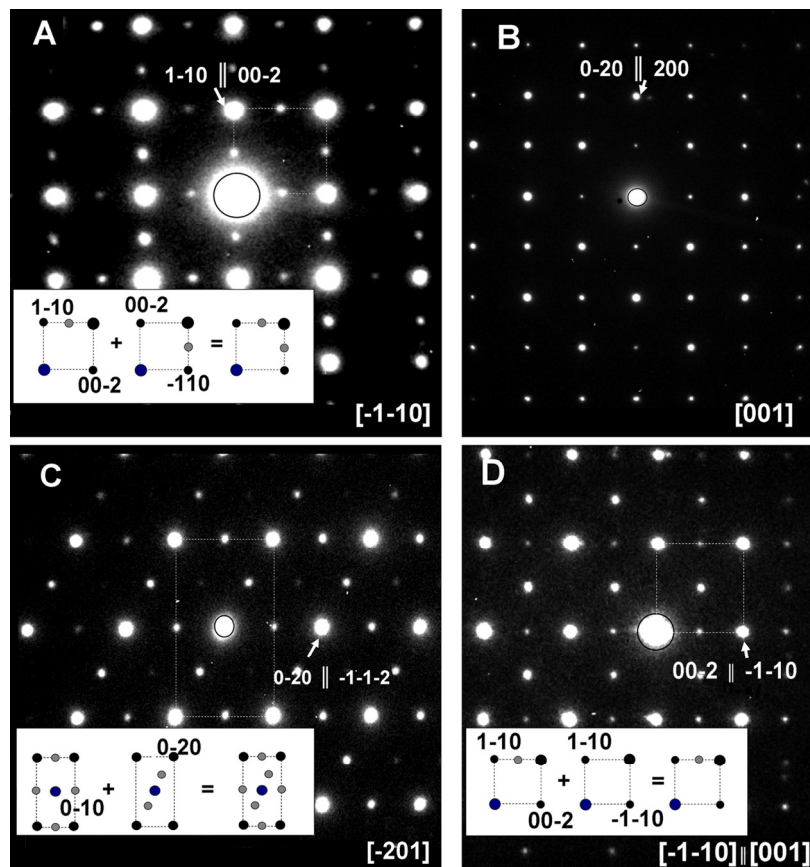


Figure 5.19. Examples of ED patterns resulting from the superposition of different twin domains in $\text{CaMo}(\text{O},\text{N})_3$: A. 90° oriented $[-1-10]$ domains; B. 90° oriented $[001]$ domains; C. 60° oriented $[-201]$ domains; D. 45° oriented $[-1-10]$ and $[001]$ domains

ED pattern (Fig. 5.18, 5.19) exhibits reflections with indices $(h00)$, $(0k0)$ and $(00l)$: $h = 2n+1$, $k = 2n+1$, $l = 2n+1$. But these reflections are less intense compared to $(h00)$, $(0k0)$ and $(00l)$: $h = 2n$, $k = 2n$, $l = 2n$, and disappear upon sample rotation. They are therefore to be attributed to double diffraction. This conclusion is also confirmed by the absence of any forbidden diffraction in the $[010]$ zone. On both our XRPD and ED (Fig. 5.18A) patterns we do not observe $(0kl)$ reflections (with $k = 2n+1$), which are allowed in the $P2_1/n$ space group and are not allowed in the space group $Pbnm$. From that we conclude that the true space group for both CaMoO_3 and $\text{CaMo}(\text{O,N})_3$ is $Pbnm$.

Mainly two types of twin-domains were found for CaMoO_3 : A) 45° oriented $[-1-10]$ and $[001]$ domains; B) Domains formed by the superposition of $[010]$ and $[100]$ zone axes.

For $\text{CaMo}(\text{O,N})_3$ more twin-domain types have been found: A) 90° oriented $[-1-10]$ domains (Fig. 5.19A); B) 90° oriented $[001]$ domains (Fig. 5.19B); C) 60° oriented $[-201]$ domains (Fig. 5.19C) D) 45° oriented $[-1-10]$ and $[001]$ domains (Fig. 5.19D).

Formation of twin domains of these types were reported earlier for a number of distorted perovskite-type oxides with similar lattice parameters (in our case the mismatch for CaMoO_3 between a and b is 2.3 %, whereas for $\text{CaMo}(\text{O,N})_3$ the mismatch is 0.9 %) [132-135].

Rietveld refinements of $\text{CaMo}(\text{O,N})_3$ from both neutron and x-ray data were carried out in space group $Pbnm$. In the starting structural model the Ca:Mo ratio was set to 1:1, whereas the O:N ratio was set to 2:1. The background was determined manually, refined at the initial stages and fixed during the further refinement. Thermal displacement factors were refined isotropically for all the atoms. Since x-rays are not able to distinguish between O^{2-} and N^{3-} we did not attempt to refine the anionic composition from the x-ray data. During the neutron data refinement the occupancy factors for oxygen and nitrogen were refined with the anionic site constrained to be fully occupied. Finally, the lattice and the profile parameters, $2\Theta_0$, the background coefficients, the thermal displacement factors and the anionic occupancies (neutron data) were refined together. To improve the fit, $\delta\text{-MoN}$ ($P\bar{6}m2$) [136], $\gamma\text{-Mo}_2\text{N}$ ($Fm\bar{3}m$) [137], and CaO ($Fm\bar{3}m$) were included in the refinements. Amounts of these secondary phases were determined from the XRPD data

(Fig. 5.20) refinement (the refinement resulted in ~1 wt % of CaO and ~2 wt % of each MoN and Mo₂N phases) and were kept fixed during the neutron data refinement. Further inspection of the neutron diffraction profiles and difference graphs revealed weak features attributed to the presence of some not identified impurity phase. Therefore, the regions containing main reflections of that phase were excluded from the refinement.

The statistics of the refinements, the visual inspection of the fit (Fig. 5.20-5.21) and the refined values of the thermal displacement factors indicate that the chosen model was correct.

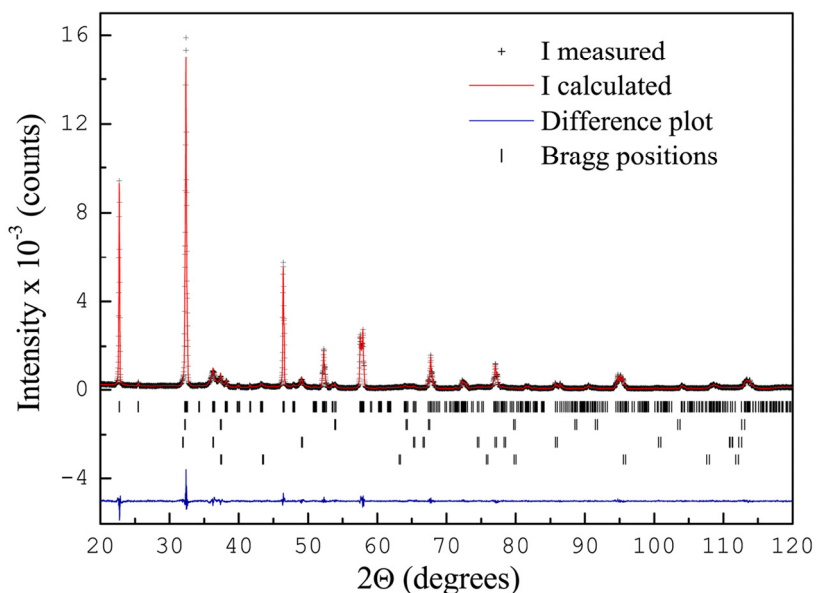


Figure 5.20. Rietveld refinement plot of the x-ray powder diffraction data for CaMoO_{1.7(1)}N_{1.3(1)}. Space group: *Pbnm*. The observed intensities, calculated profile, difference curve and Bragg positions are shown. CaO, δ -MoN and γ -Mo₂N have been included as a minor impurity phases in the refinement

The refined O/N content and the anionic distribution correspond to the composition CaMoO_{1.7(1)}N_{1.3(1)} with a totally disordered O/N arrangement. The result is in a reasonable agreement with the hotgas extraction analysis, which yielded in the composition of CaMoO_{1.79(5)}N_{1.25(2)} obtained after subtracting the secondary phases contribution (taken

from the refinement). The neutron data derived O/N content corresponds to the formal oxidation state of Mo +5.3. Higher nitrogen content of this phase as compared to that of $\text{SrMo}(\text{O,N})_3$ phase [88] can be explained by higher ammonia flow and lower synthesis temperature employed during the present investigation.

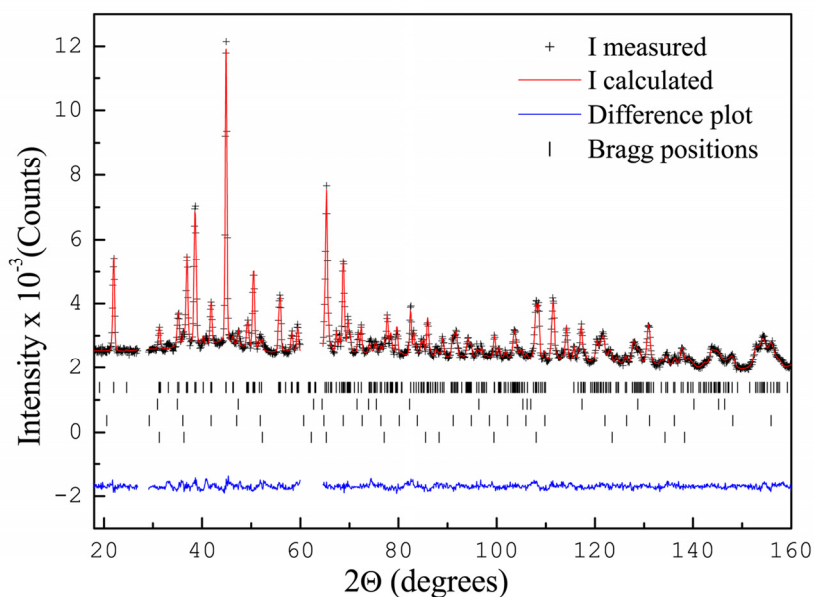


Figure 5.21. Rietveld refinement plot of the neutron powder diffraction data for $\text{CaMoO}_{1.7(1)}\text{N}_{1.3(1)}$. Space group: *Pbnm*. The observed intensities, calculated profile, difference curve and Bragg positions are shown. CaO , $\delta\text{-MoN}$ and $\gamma\text{-Mo}_2\text{N}$ have been included as a minor impurity phases in the refinement.

As a summary of the refinements, the obtained structural parameters bond lengths and angles are displayed in Tables 5.2, 5.3.

Table 5.2. Refinement results for CaMoO_3 and $\text{CaMoO}_{1.7(1)}\text{N}_{1.3(1)}$

Name	CaMoO_3	$\text{CaMoO}_{1.7(1)}\text{N}_{1.3(1)}$	$\text{CaMoO}_{1.7(1)}\text{N}_{1.3(1)}$
radiation	x-ray $\text{CuK}_{\alpha 1/2}$	x-ray $\text{CuK}_{\alpha 1/2}$	neutron (HRPT, PSI)
λ , Å	1.5406/1.5444	1.5406/1.5444	1.494
T, K	298	298	298
S.G.	<i>Pbnm</i>	<i>Pbnm</i>	<i>Pbnm</i>

a , Å		5.4499(1)	5.5029(1)	5.5068(1)
b , Å		5.5811(1)	5.5546(1)	5.5593(1)
c , Å		7.7791(1)	7.8248(1)	7.8317(2)
V , Å ³		236.62(1)	239.19(1)	239.76(1)
Z		4	4	4
Ca	x	0.9894(7)	0.9970(10)	0.9941(13)
	y	0.0461(3)	0.0294(5)	0.0334(9)
	z	¼	¼	¼
	B_{iso} , Å ²	0.46(4)	1.13(3)	1.05(7)
	site	4c	4c	4c
	occ.	1	1	1
Mo	x	½	½	½
	y	0	0	0
	z	0	0	0
	B_{iso} , Å ²	0.11(2)	0.901(13)	0.74(5)
	site	4b	4b	4b
	occ.	1	1	1
O/N(1)	x	0.081(1)	0.0717(15)	0.0642(6)
	y	0.4750(10)	0.4731(17)	0.4872(7)
	z	¼	¼	¼
	B_{iso} , Å ²	0.92(7)	1.13(9)	0.90(8)
	site	4c	4c	4c
	occ.	1/0	0.56/0.44 ^a	0.56(4)/0.44(4)
O/N(2)	x	0.7055(8)	0.7034(11)	0.7113(5)
	y	0.2921(8)	0.2897(12)	0.2885(5)
	z	0.0453(6)	0.0329(9)	0.0329(3)
	B_{iso} , Å ²	0.92(7)	1.13(9)	0.90(6)
	site	8d	8d	8d
	occ.	1/0	0.57/0.43 ^a	0.57(3)/0.43(3)
χ^2		2.13	1.71	1.97
wR_p^b		0.135	0.136	0.128
R_p^b		0.102	0.128	0.149

^a Not refined.

Table 5.3. Selected bond distances in Å and angles in degrees calculated for CaMoO₃ and CaMoO_{1.7(1)}N_{1.3(1)}^a

		CaMoO ₃	CaMoO _{1.7(1)} N _{1.3(1)}
Mo-O/N(1)	x2	2.000(1)	1.9909(6)
Mo-O/N(2)	x2	2.009(4)	1.997(3)
Mo-O/N(2)	x2	2.012(4)	1.995(3)
<Mo-O/N>		2.007(3)	1.994(2)
Ca-O/N(1)		3.228(6)	3.061(6)
Ca-O/N(1)		2.445(6)	2.552(6)
Ca-O/N(1)		3.138(7)	3.085(8)
Ca-O/N(1)		2.371(7)	2.446(8)
Ca-O/N(2)	x2	2.610(5)	2.708(6)
Ca-O/N(2)	x2	2.735(5)	2.705(5)
Ca-O/N(2)	x2	2.382(5)	2.454(5)
Ca-O/N(2)	x2	3.407(5)	3.278(5)
<Ca-O/N> _(8 short) ^b		2.520(6)	2.592(6)
Mo-O/N(1)-Mo	x2	153.00(6)	159.13(3)
Mo-O/N(2)-Mo	x4	151.9(2)	157.01(11)
<Mo-O/N-Mo>		152.267(15)	157.72(8)

^a Derived from the neutron data.

^b The average, calculated from the 8 shortest distances.

According to the refinements, the average Ca–O/N distance increases upon the substitution of oxygen with nitrogen, which is consistent with a larger ionic radius of N³⁻ (1.48 Å) compared to that of O²⁻ (1.38 Å). The average Mo–O/N distance value of CaMoO_{1.7(1)}N_{1.3(1)} (1.994(2) Å) resembles the one determined for SrMoO_{1.89(2)}N_{1.11(2)} by neutron diffraction (1.999(5) Å) [88]. However, partial substitution of O²⁻ in SrMoO₃ by N³⁻ leads to an increase of the average Mo–O/N distance, which is not the case for CaMoO₃ (Table 5.3), where the mean Mo–O/N distance is not significantly affected by the substitution. Moreover, the smaller average Mo–O/N distance of CaMoO_{1.7(1)}N_{1.3(1)} than that of SrMoO_{1.89(2)}N_{1.11(2)} does not agree with the O/N composition of these phases. This indicates that CaMoO_{1.7(1)}N_{1.3(1)} may contain anionic/cationic vacancies. Thermal displacement parameters values of Ca and Mo in CaMoO_{1.7(1)}N_{1.3(1)} are higher than those in CaMoO₃,

which gives hint for the presence of the cationic vacancies in the former compound. Hence, true formal oxidation state of Mo in this compound must be lower than that calculated from the O/N content.

Based on the refined Mo–O/N–Mo angle values for CaMoO_3 and $\text{CaMoO}_{1.7(1)}\text{N}_{1.3(1)}$ it can be concluded that the crystal structure of the latter compound is less distorted. This is in accordance with higher ionic radius of N^{3-} compared to that of O^{2-} .

Similar to CaMoO_3 the reflections of $\text{CaMoO}_{1.7(1)}\text{N}_{1.3(1)}$ are broadened isotropically (Fig. 5.22). The refined apparent size is 0.14 μm , the strain is 0.29 % . Both values are close to those obtained for CaMoO_3 .

SEM reveals a particle size of about 0.2 μm for both CaMoO_3 and $\text{CaMoO}_{1.7(1)}\text{N}_{1.3(1)}$ (Fig. 5.23). Thus, size broadening on the diffractograms arises from both the crystallites size and the presence of twin domains. Small apparent strain values obtained for both CaMoO_3 and $\text{CaMoO}_{1.7(1)}\text{N}_{1.3(1)}$ confirm that both materials are chemically homogeneous. The larger apparent size and the smaller apparent strain values obtained for $\text{CaMoO}_{1.7(1)}\text{N}_{1.3(1)}$ compared to CaMoO_3 can arise either from the smaller mismatch between a and c lattice constants for the former compound or from the different thermal history of the samples, which would also explain the multiplicity of different twin types observed for $\text{CaMoO}_{1.7(1)}\text{N}_{1.3(1)}$ by TEM.

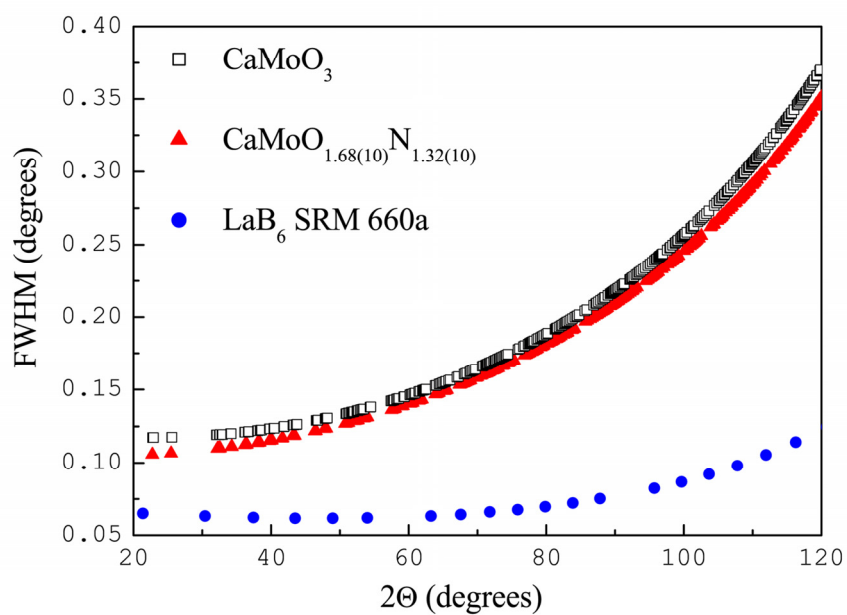


Figure 5.22. Angular variation of the total full width at half maximum (FWHM) determined from whole profile Rietveld refinements of the XRPD data for CaMoO_3 , $\text{CaMoO}_{1.7(1)}\text{N}_{1.3(1)}$ and the standard LaB_6 SRM 660a

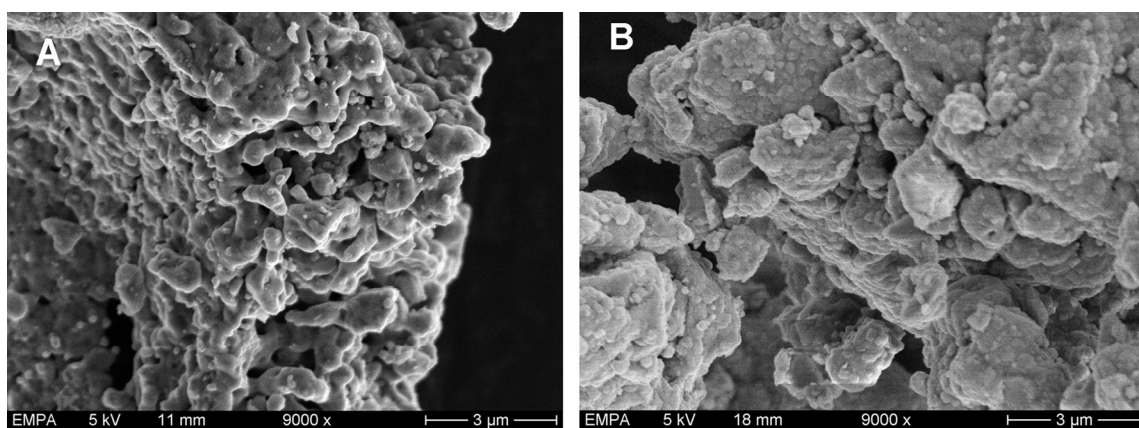


Figure 5.23. SEM micrographs (taken with the magnification of 9000 x) of powders with composition A. CaMoO_3 , B. $\text{CaMoO}_{1.7(1)}\text{N}_{1.3(1)}$

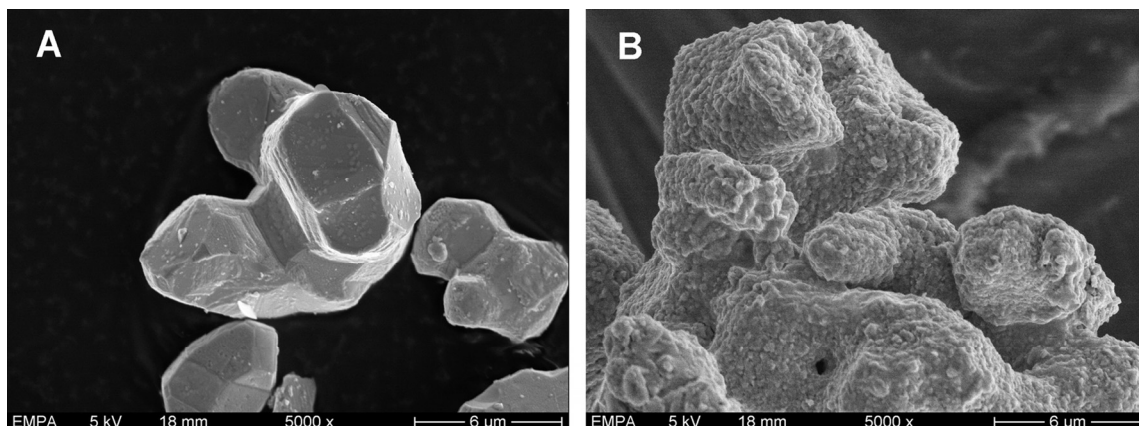


Figure 5.24. SEM micrographs (taken with the magnification of 5000 x) of powders with composition A. BaMoO_3 , B. $\text{BaMo}(\text{O},\text{N})_3$ (the XRPD refined apparent particle size is 0.12 μm)

SEM together with XRPD reveal a particle size of $\text{BaMo}(\text{O},\text{N})_3$ similar to that of $\text{CaMo}(\text{O},\text{N})_3$ (Fig. 5.24). Because of the unknown impurity composition and structure we did not attempt a whole pattern refinement of XRPD data of $\text{BaMo}(\text{O},\text{N})_3$, but rather estimate the lattice constant and line broadening of $\text{BaMo}(\text{O},\text{N})_3$. The obtained lattice constant (4.0657(1) Å) is larger than the one refined from the XRPD data for BaMoO_3 (4.0409(1) Å). Contrary to the partial oxidation of Mo^{4+} to smaller Mo^{5+} and Mo^{6+} , a partial replacement of O^{2-} with larger N^{3-} will lead to the increase of the lattice constant. From the comparison of the lattice constant values for BaMoO_3 and $\text{BaMo}(\text{O},\text{N})_3$ follows that it is the difference in the ionic radii of O^{2-} and N^{3-} , which has a major influence on the lattice constant. The larger lattice constant of $\text{BaMo}(\text{O},\text{N})_3$ indicates that both Mo–O/N and Ba–O/N distances increase upon partial substitution of O^{2-} with N^{3-} in BaMoO_3 .

5.2.7. Conclusions

The possibility to prepare previously unreported oxynitride-perovskite $A\text{Mo}(\text{O},\text{N})_3$ ($A = \text{Ca}, \text{Ba}$) phases by thermal ammonolysis of $A\text{MoO}_4$ and $A\text{MoO}_3$ oxide precursors was investigated.

Only the ammonolysis of CaMoO_3 and BaMoO_3 is leading to a considerable yield of the desired phases. CaMoO_4 reacted with ammonia decomposes to CaO and Mo_2N .

BaMo(O,N)₃ is formed as a minor phase during the ammonolysis of BaMoO₄, which yields mainly in Ba₃Mo₂O₆N₂. Thus, the crystal structure of the starting precursor is crucial for the desired phase formation. Among the other factors influencing the phase formation during the ammonolysis of *AMoO*₃ and *AMoO*₄ we considered the gas to solid ratio, positive inductive effect of the *A*-site cation, the lattice energy, the structure distortion energy and Mo-N bonding covalence.

CaMo(O,N)₃ crystallizes in space group *Pbnm* and possesses a less distorted crystal structure than CaMoO₃. Neutron diffraction reveals a statistical distribution of O²⁻ and N³⁻ among the available anionic sites and an anionic content corresponding to the composition CaMoO_{1.7(1)}N_{1.3(1)}.

TEM shows evidence for twin-domains in both CaMoO₃ and CaMoO_{1.7(1)}N_{1.3(1)}, which together with the average crystallite size may be responsible for the line profile broadening in the XRPD patterns. The multiplicity of different twin types measured for CaMoO_{1.7(1)}N_{1.3(1)} compared to CaMoO₃ can be explained either by the smaller mismatch between *a* and *c* lattice constants in the former compound or by the different thermal history of the compounds.

BaMo(O,N)₃ adopts the space group *Pm* $\bar{3}$ *m*. This indicates a totally disordered O/N arrangement as found for CaMoO_{1.7(1)}N_{1.3(1)}. Its determined lattice parameter and consequently both Mo–O/N and Ba–O/N distances are larger than of the corresponding BaMoO₃ as revealed by x-ray diffraction, which is attributed to the larger ionic radius of N³⁻ compared to that of O²⁻.

Summary

This thesis is dedicated to the synthesis and characterization of novel perovskite-type oxynitrides.

The study yielded in several novel and previously uncharacterized oxynitride phases with d^{0-2} electronic configurations of the constituent transition elements, *e.g.* LaNbON₂, SrMoO_{3-x}N_x ($x > 1$), CaMo(O,N)₃, BaMo(O,N)₃, Ca_{1-x}La_xTiO_{3-x}N_x ($x = 0-0.7$). Anionic composition of the synthesized phases was evaluated by a variety of methods: thermal gravimetric analysis, hotgas extraction, neutron diffraction. Crystal structure and anionic distribution of the synthesized materials were investigated by x-ray-, neutron powder diffraction and transmission electron microscopy. Optical band gaps of the synthesized d^0 -oxynitrides were determined from UV-Vis diffuse-reflectance spectroscopic measurements. Electronic conductivity, heat transport and magnetic susceptibility of the mixed-valent (d^{0-2}) oxynitrides were studied.

The main achievements of the present study and suggestions for further research are summarized as follows:

1. **Ca_{1-x}La_xTiO_{3-x}N_x ($x = 0-0.7$).** Novel solid solutions of general composition Ca_{1-x}La_xTiO_{3-x}N_x ($x = 0-0.7$), which show linear response between optical band gap value and chemical composition, bright colors and good thermal stability essential for the pigment application. A further investigation of photocatalytic activity of these materials as a function of their composition would be of interest.
2. **LaNbON₂.** A perovskite-type oxynitride LaNbON₂ was synthesized. This material possesses the smallest optical band gap (1.7 eV) among the known oxynitride-type perovskites. Moreover, it catalyzes H₂ production from the water-methanol mixtures. The photocatalytic performance of a material depends on the position of its conduction band relative to the electrode potential for the H₂-evolution. The latter is a function of the pH of a solution. Therefore, the further study of the photocatalytic performance of LaNbON₂ as a function of the pH is of interest. Moreover, it is useful to develop a method, which allows impregnating the powder

of LaNbON_2 with noble metals (such as Pt, Au) without causing the powder surface reduction. This would be extremely useful to improve its photocatalytic performance.

3. **$\text{SrMoO}_{3-x}\text{N}_x$ ($x > 1$).** Novel mixed-valent oxynitrides of general composition $\text{SrMoO}_{3-x}\text{N}_x$ ($x > 1$) were synthesized. Their crystal structure, Mo-oxidation state and physical properties were investigated.
4. **$\text{CaMoO}_{1.7(1)}\text{N}_{1.3(1)}$, $\text{BaMo}(\text{O},\text{N})_3$.** Phase formation and crystal structure of two novel oxynitrides $\text{CaMoO}_{1.7(1)}\text{N}_{1.3(1)}$, $\text{BaMo}(\text{O},\text{N})_3$ were studied. The interest to the N^{3-} - and N_2 -containing inorganic and metal-organic Mo-derivatives is driven by the ability of these compounds to catalyze molecular nitrogen reduction into ammonia. Therefore, as further work, catalytic study on the synthesized oxynitride-perovskites and intermediate products of their thermal reoxidation is proposed.

List of publications

1. D. Logvinovich, A. Borger, M. Doebeli, S. G. Ebbinghaus, A. Reller and A. Weidenkaff, Synthesis and physical chemical properties of Ca substituted LaTiO_2N , *Progress in Solid State Chemistry*, 35 (2007), pp. 281-290.
2. D. Logvinovich, R. Aguiar, R. Robert, M. Trottmann, S. G. Ebbinghaus, A. Reller and A. Weidenkaff, Synthesis, Mo-valence state, thermal stability and thermoelectric properties of $\text{SrMoO}_{3-x}\text{N}_x$ ($x>1$) oxynitride perovskites, *Journal of Solid State Chemistry*, 180 (2007), pp. 2649-2654.
3. D. Logvinovich, J. Hejtmánek, R. Aguiar, M. Trottmann, S.G. Ebbinghaus, A. Reller and A. Weidenkaff, Phase formation, structural and microstructural characterization of novel oxynitride-perovskites synthesized by thermal ammonolysis of $(\text{Ca,Ba})\text{MoO}_4$ and $(\text{Ca,Ba})\text{MoO}_3$, *Journal of Solid State Chemistry*, 181 (2008), pp. 2243-2249.
4. D. Logvinovich, L.Bocher, D. Sheptyakov, R. Figi, S.G. Ebbinghaus, R Aguiar, M. Aguirre, A. Reller and A. Weidenkaff, Microstructure, surface composition and chemical stability of partly ordered LaTiO_2N , *Solid State Sciences*, submitted.
5. D. Logvinovich, J. Hejtmanek, K. Knižek, M. Maryško, N. Homazava, P. Tomeš, S.G. Ebbinghaus, A. Reller and A. Weidenkaff, On the magnetism, thermal and electronic transport of SrMoO_2N , *Journal of Applied Physics*, accepted.
6. M. H. Aguirre, S. Canulescu, R. Robert, N. Homazava, D. Logvinovich, L. Bocher, Th. Lippert, M. Dobeli, and A. Weidenkaff, Structure, microstructure, and high-temperature transport properties of $\text{La}_{1-x}\text{Ca}_x\text{MnO}_{3-\delta}$ thin films and polycrystalline bulk materials, *Journal of Applied Physics*, 103 (2008), p. 013703.
7. R.Aguiar, D. Logvinovich, A. Weidenkaff, A. Rachel, A. Reller, S.G. Ebbinghaus, The vast colour spectrum of ternary metal oxynitride pigments, *Dyes and Pigments*, 76 (2008), pp. 70-75.
8. R. Aguiar, Y. Lee, K. Domen, A. Kalytta, D. Logvinovich, A. Weidenkaff, A. Reller and S. G. Ebbinghaus, Advances in Oxynitride Perovskites: Synthesis and Photocatalytic Applications, Book chapter in *Ceramic Materials Research Trends*, (2007) pp. 107-133
9. I. Marozau, M. Dobeli, T. Lippert, D. Logvinovich, M. Mallepell, A. Shkabko, A. Weidenkaff, A. Wokaun, One-step preparation of N-doped strontium titanate films by pulsed laser deposition, *Applied Physics A* 89 (2007), pp. 933-940.

10. M. H. Aguirre, R. Robert, D. Logvinovich, A. Weidenkaff, Synthesis, crystal structure and microstructure analysis of perovskite-type compounds $\text{LnCo}_{0.95}\text{Ni}_{0.05}\text{O}_3$ (Ln = La, Pr, Nd, Sm, Gd, Dy), *Inorganic Chemistry*, 46 (2007), pp. 2744-2750.
11. L. Bocher, M.H. Aguirre, R.Robert, M.Trottmann, D. Logvinovich, P. Hug, A. Weidenkaff, Chemie douce synthesis and thermochemical characterization of mesoporous perovskite type titanate phases, *Thermochimica Acta*, 457 (2007), pp. 11-19.
12. S. Canulescu, Th. Lippert, A. Wokaun, M. Doebeli, A. Weidenkaff, R. Robert and D. Logvinovich, The effect of the fluence on the properties of La- Ca- Mn- O thin films prepared by pulsed laser deposition, *Applied Surface Science*, 253 (2007), pp. 8174-8178.
13. R. Aguiar, D. Logvinovich, A. Weidenkaff, H. Karl, C.W. Schneider, A. Reller and S.G. Ebbinghaus, Physical Properties of (La, Sr)Ti(O, N)₃ Thin Films Grown by Pulsed Laser Deposition, *Materials research bulletin* (2007), In press, Corrected proof.
14. S. Canulescu, Th. Lippert, A. Wokaun, R. Robert, D. Logvinovich, A. Weidenkaff, M. Doebeli and M. Schneider, Preparation of epitaxial $\text{La}_{0.6}\text{Ca}_{0.4}\text{Mn}_{1-x}\text{Fe}_x\text{O}_3$ ($x = 0, 0.2$) thin films: Variation of the oxygen content, *Progress in Solid State Chemistry*, 35 (2007), pp. 241-248.
15. B. Louis-Schmid, P. Rais, D. Logvinovich, S.M. Bernasconi and H. Weissert, Impact of methane seeps on the local carbon-sotope record: a case study from a Late Jurassic hemipelagic section, *Terra Nova*, 19 (2007), pp. 259-265.
16. E.N. Naumovich, V.V. Kharton, A.A. Yaremchenko, M.V. Patrakeev, D.G.Kellerman, D.I. Logvinovich and V.L. Kozhevnikov, Defect formation in $\text{LaGa}(\text{Mg},\text{Ni})\text{O}_{3-\delta}$: A statistical thermodynamic analysis validated by mixed conductivity and magnetic susceptibility measurements, *Physical Review B* 74, (2006), p. 064105.
17. S. Canulescu, Th. Lippert, H. Grimmer, A. Wokaun, R. Robert, D. Logvinovich, A. Weidenkaff, M. Doebeli, Structural characterization and magnetoresistance of manganates thin films and Fe-doped manganates thin films, *Applied Surface Science* (2006), 252, pp.4599-4603.
18. E. N. Naumovich, M. V. Patrakeev, V. V. Kharton, A. A. Yaremchenko, D. I. Logvinovich, F. M. B. Marques, Oxygen nonstoichiometry in $\text{La}_2\text{Ni}(\text{M})\text{O}_{4+\delta}$ (M = Cu,Co) under oxidizing conditions, *Solid State Sciences*, 7 (2005), pp. 1353-1362.
19. V. V. Kharton, A. A. Yaremchenko, A. L. Shaula, M. V. Patrakeev, E. N. Naumovich, D. I. Logvinovich, J. R. Frade and F. M. B. Marques, Transport

properties and stability of Ni-containing mixed conductors with perovskite- and K_2NiF_4 -type structure, *Journal of Solid State Chemistry*, 177 (2004), vol. 177, pp.26-37.

20. A. L. Shaula, A. A. Yaremchenko, V. V. Kharton, D. I. Logvinovich, E. N. Naumovich, A. V. Kovalevsky, J. R. Frade and F. M. B. Marques, Oxygen permeability of LaGaO₃-based ceramic membranes, *Journal of Membrane Science*, 221 (2003), pp. 69-77.
21. A. A. Yaremchenko, A. L. Shaula, D. I. Logvinovich, V. V. Kharton, A. V. Kovalevsky, E.N. Naumovich, J. R. Frade, F. M. B. Marques, Oxygen-ionic conductivity of perovskite-type La_{1-x}Sr_xGa_{1-y}Mg_yM_{0.20}O_{3-δ} (M=Fe, Co, Ni), *Materials Chemistry and Physics*, 82 (2003), pp. 684-690.
22. V. N. Tikhonovich, E. N. Naumovich, D. I. Logvinovich, V. V. Kharton, A. A. Veher, Oxygen deficiency and phase transitions in SrCo_{1-x-y}Fe_xCr_y O_{3-δ} (x=0.10-0.40, y = 0-0.05), *Journal of Solid State Electrochemistry*, 7 (2003), pp. 77-82.
23. A. L. Shaula, A. P. Viskup, V. V. Kharton, D. I. Logvinovich, E. N. Naumovich, J. R. Frade, F. M. B. Marques, Oxygen permeability of LaGa_{0.65}Ni_{0.2}Mg_{0.15}O_{3-δ} ceramics: effect of synthesis method, *Materials research bulletin*, 38 (2003), pp. 353-362.
24. M. Kopcewicz, D. D. Khalyavin, I. O. Troyanchuk, H. Szymczak, R. Szymczak, D. J. Logvinovich, and E. N. Naumovich, Effect of iron doping on the properties of TbBaCo₂O_{5.5} layered perovskite, *Journal of Applied Physics*, 93 (2003), pp 479 –486.

References

- [1] L. Katz and R. Ward, *Inorg. Chem.* 3 (1964) 205-211.
- [2] J.B. Goodenough and J.A. Kafalas, *J. Solid State Chem.* 6 (1973) 493-501.
- [3] J.B. Goodenough, *Rep. Prog. Phys.* 67 (2004) 1915-1993.
- [4] C.J. Howard and H.T. Stokes, *Acta Crystallogr., Sect. B* 54 (1998) 782-789.
- [5] H.W. Eng, P.W. Barnes, B.M. Auer, and P.M. Woodward, *J. Solid State Chem.* 175 (2003) 94-109.
- [6] J. Etourneau, J. Portier, and F. Menil, *J. Alloys Compd.* 188 (1992) 1-7.
- [7] A. Fujishima and K. Honda, *Nature* 238 (1972) 37-38.
- [8] H.J.A. Koopmans, G.M.H. van de Velde, and P.J. Gellings, *Acta Crystallogr., Sect. C* 39 (1983) 1323-1325.
- [9] R.D. Nasby and R.K. Quinn, *Mater. Res. Bull.* 11 (1976) 985-992.
- [10] G.H. Kwei, A.C. Lawson, S.J.L. Billinge, and S.W. Cheong, *J. Phys. Chem.* 97 (1993) 2368-2377.
- [11] A. Kasahara, K. Nukumizu, T. Takata, J.N. Kondo, M. Hara, H. Kobayashi, and K. Domen, *J. Phys. Chem. B* 107 (2003) 791-797.
- [12] M. Hara, T. Takata, J.N. Kondo, and K. Domen, *Catal. Today* 90 (2004) 313-317.
- [13] H. Kato and A. Kudo, *Chem. Phys. Lett.* 295 (1998) 487-492.
- [14] R. Hsu, E.N. Maslen, D. du Boulay, and N. Ishizawa, *Acta Crystallogr., Sect. B* 53 (1997) 420-428.
- [15] B.J. Kennedy, A.K. Prodjosantoso, and C.J. Howard, *J. Phys.: Condens. Matter* 11 (1999) 6319-6327.
- [16] M. Machida, S. Murakami, T. Kijima, S. Matsushima, and M. Arai, *J. Phys. Chem. B* 105 (2001) 3289-3294.
- [17] I. Hartenbach, F. Lissner, T. Nikelski, S.F. Meier, H. Müller-Bunz, and T. Schleid, *Z. Anorg. Allg. Chem.* 631 (2005) 2377-2382.
- [18] K. Kato, *Acta Cryst. B* 32 (1976) 764-767.
- [19] J. Xing, Z. Shan, K. Li, J. Bian, X. Lin, W. Wang, and F. Huang, *J. Phys. Chem. Solids* 69 (2008) 23-28.
- [20] D.P.N. Made, M.R. Sahar, and M.R. Sudin, *J. Nonlinear. Opt. Phys.* 14 (2005) 237-243.
- [21] J.W. Liu, G. Chen, Z.H. Li, and Z.G. Zhang, *Int. J. Hydrogen Energy* 32 (2007) 2269-2272.
- [22] A.C. Sakowski-Cowley, K. Lukaszewicz, and H.D. Megaw, *Acta Cryst. B* 25 (1969) 851-865.
- [23] A.W. Hewat, *J. Phys. C Solid. State* 6 (1973) 2559-2572.
- [24] C.J. Howard, V. Luca, and K.S. Knight, *Journal of Physics: Condensed Matter* 14 (2002) 377-387.
- [25] K. Sayama and H. Arakawa, *J. Phys. Chem.* 97 (1993) 531-533.
- [26] F.J. Torres, J.M. Amigo, and J. Alarcon, *J. Solid State Chem.* 173 (2003) 40-44.
- [27] M. Jansen and H.P. Letschert, *Nature* 404 (2000) 980-982.

- [28] A.J. Nozik, *Appl. Phys. Lett.* 30 (1977) 567-569.
- [29] F.E. Osterloh, *Chem. Mater.* 20 (2008) 35-54.
- [30] K. Domen, S. Naito, T. Onishi, and K. Tamaru, *Chem. Phys. Lett.* 92 (1982) 433-434.
- [31] J. Kim, D. Hwang, H. Kim, S. Bae, J. Lee, W. Li, and S. Oh, *Top. Catal.* 35 (2005) 295-303.
- [32] H.G. Kim, D.W. Hwang, J. Kim, Y.G. Kim, and J.S. Lee, *Chem. Commun.* 12 (1999) 1077-1078.
- [33] H. Kato, K. Asakura, and A. Kudo, *J. Am. Chem. Soc.* 125 (2003) 3082-3089.
- [34] J.B. Goodenough, *Czechoslovak journal of physics* 17 (1967) 304-336.
- [35] R. Shannon, *Acta Crystallogr., Sect. A* 32 (1976) 751-767.
- [36] R.D. Shannon and C.T. Prewitt, *Acta Crystallogr., Sect. B* 25 (1969) 925-946.
- [37] R. Marchand, F. Tessier, A. Le Sauze, and N. Diot, *Int. J. Inorg. Mater.* 3 (2001) 1143-1146.
- [38] Y.-I. Kim, P.M. Woodward, K.Z. Baba-Kishi, and C.W. Tai, *Chem. Mater.* 16 (2004) 1267-1276.
- [39] P. Antoine, R. Assabaa, P. L'Haridon, R. Marchand, Y. Laurent, C. Michel, and B. Raveau, *Mater. Sci. Eng., B* 5 (1989) 43-46.
- [40] R. Marchand, Y. Laurent, J. Guyader, P. L'Haridon, and P. Verdier, *J. Eur. Ceram. Soc.* 8 (1991) 197-213.
- [41] F. Tessier and R. Marchand, *J. Solid State Chem.* 171 (2000) 143-151.
- [42] I. Elphinstone and A. Hendry, *Fabrication Technology British Ceramic Proceedings, No.45* (1989) 15-22.
- [43] A. Hellwig and A. Hendry, *J. Mater. Sci.* 29 (1994) 4686-4693.
- [44] S.H. Elder, F.J. DiSalvo, L. Topor, and A. Navrotsky, *Chem. Mater.* 5 (1993) 1545-1553.
- [45] S.J. Clarke, K.A. Hardstone, C.W. Michie, and M.J. Rosseinsky, *Chem. Mater.* 14 (2002) 2664-2669.
- [46] S.J. Clarke, B.P. Guinot, C.W. Michie, M.J.C. Calmont, and M.J. Rosseinsky, *Chem. Mater.* 14 (2002) 288-294.
- [47] P. Antoine, R. Marchand, Y. Laurent, C. Michel, and B. Raveau, *Mater. Res. Bull.* 23 (1988) 953-957.
- [48] G. Liu, X. Zhao, and H.A. Eick, *J. Alloys Compd.* 187 (1992) 145-156.
- [49] I.D. Fawcett, K.V. Ramanujachary, and M. Greenblatt, *Mater. Res. Bull.* 32 (1997) 1565-1570.
- [50] A. Rachel, S.G. Ebbinghaus, M. Gungerich, P.J. Klar, J. Hanss, A. Weidenkaff, and A. Reller, *Thermochim. Acta* 438 (2005) 134-143.
- [51] F. Pors, P. Bacher, R. Marchand, Y. Laurent, and G. Roult, *Revue internationale des hautes températures et des réfractaires* 24 (1987-1988) 239-246.
- [52] S.G. Ebbinghaus, A. Weidenkaff, A. Rachel, and A. Reller, *Acta Crystallogr., Sect. C* 60 (2004) i91-i93.
- [53] R. Marchand, F. Pors, and Y. Laurent, *Ann. Chim. Fr.* 16 (1991) 553-560.
- [54] F.T. François Cheviré, Roger Marchand, *Eur. J. Inorg. Chem.* 2006 (2006) 1223-1230.

- [55] G. Tobias, D. Beltran-Porter, O.I. Lebedev, G. VanTendeloo, J. Rodriguez-Carvajal, and A. Fuertes, *Inorg. Chem.* 43 (2004) 8010-8017.
- [56] F. Pors, R. Marchand, Y. Laurent, P. Bacher, and G. Roult, *Mater. Res. Bull.* 23 (1988) 1447-1450.
- [57] P. Maillard, F. Tessier, E. Orhan, F. Chevire, and R. Marchand, *Chem. Mater.* 17 (2005) 152-156.
- [58] R.H. E. Günther, M. Jansen, *Z. Anorg. Allg. Chem.* 626 (2000) 1519-1525.
- [59] N. Diot, R. Marchand, J. Haines, J.M. Leger, P. Macaudiere, and S. Hull, *J. Solid State Chem.* 146 (1999) 390-393.
- [60] P. Bacher, P. Antoine, R. Marchand, P. L'Haridon, Y. Laurent, and G. Roult, *J. Solid State Chem.* 77 (1988) 67-71.
- [61] R. Pastrana-Fabregas, J. Isasi-Marin, C. Cascales, and R. Saez-Puche, *J. Solid State Chem.* 180 (2007) 92-97.
- [62] M.T. Weller and S.J. Skinner, *Int. J. Inorg. Mater.* 2 (2000) 463-467.
- [63] J. Grins and G. Svensson, *Mater. Res. Bull.* 29 (1994) 801-809.
- [64] J. Rooke and M. Weller, *Diffusion and Defect Data Pt.B: Solid State Phenomena* 90-91 (2003) 417-422.
- [65] Y.-I. Kim and P.M. Woodward, *J. Solid State Chem.* 180 (2007) 3224-3233.
- [66] R. Marchand, R. Pastuszak, Y. Laurent, and G. and Roult, *Rev. Chim. Miner.* 19 (1982) 684-689.
- [67] Z.K. Huang, D.S. Yan, T.S. Yen, and T.Y. Tien, *J. Solid State Chem.* 85 (1990) 51-55.
- [68] L. Le Gendre, R. Marchand, and Y. Laurent, *J. Eur. Ceram. Soc.* 17 (1997) 1813-1818.
- [69] L. Le Gendre, R. Marchand, and B. Piriou, *Eur. J. Solid State Inorg. Chem.* 34 (1997) 973-982.
- [70] E. Orhan, F. Tessier, and R. Marchand, *Solid State Sci.* 4 (2002) 1071-1076.
- [71] S.J. Clarke, C.W. Michie, and M.J. Rosseinsky, *J. Solid State Chem.* 146 (1999) 399-405.
- [72] G. Tobias, J. Oro-Sole, D. Beltran-Porter, and A. Fuertes, *Cryst. Eng.* 5 (2002) 479-485.
- [73] F. Tessier, L. LeGendre, F. Chevire, R. Marchand, and A. Navrotsky, *Chem. Mater.* 17 (2005) 3570-3574.
- [74] J.W.H. van Krevel, H.T. Hintzen, R. Metselaar, L. Le Gendre, and R. Marchand, *Solid State Sci.* 3 (2001) 49-56.
- [75] J.-B. Veyret, M. Voorde, and M. Billy, *J. Am. Ceram. Soc.* 75 (1992) 3289-3292.
- [76] R. Aguiar, D. Logvinovich, A. Weidenkaff, A. Reller, and S.G. Ebbinghaus, *Thermochim. Acta* (2007) doi:10.1016/j.tca.2008.02.021.
- [77] A. Kasahara, K. Nukumizu, G. Hitoki, T. Takata, J.N. Kondo, M. Hara, H. Kobayashi, and K. Domen, *J. Phys. Chem. A* 106 (2002) 6750-6753.
- [78] D.A. Toshihiro Moriga, Yasuhiro Nishida, Kazuya Kitaji, Keiko Takahara, Kei-ichiro Murai, Ichiro Nakabayashi, *Phys. Status Solidi A* 203 (2006) 2818-2822.
- [79] M. Liu, W. You, Z. Lei, T. Takata, K. Domen, and C. Li, *Chinese J Catal.* 27 (2006) 556-558.

- [80] R. Asahi, T. Morikawa, T. Ohwaki, K. Aoki, and Y. Taga, *Science* 293 (2001) 269-271.
- [81] D. Yamasita, T. Takata, M. Hara, J.N. Kondo, and K. Domen, *Solid State Ionics* 172 (2004) 591-595.
- [82] R. Aguiar, Y. Lee, K. Domen, A. Kalytta, D. Logvinovich, A. Weidenkaff, A. Reller, and S.G. Ebbinghaus, Book chapter in *Ceramic Materials Research Trends* (Nova Science Publishers, Inc. ISBN: 978-1-60021-769-2) (2007) 107-133.
- [83] J.A. Schottenfeld, A.J. Benesi, P.W. Stephens, G. Chen, P.C. Eklund, and T.E. Mallouk, *J. Solid State Chem.* 178 (2005) 2313-2321.
- [84] P. Dougier and A. Casalot, *J. Solid State Chem.* 2 (1970) 396-403.
- [85] P. Dougier and P. Hagenmuller, *J. Solid State Chem.* 15 (1975) 158-166.
- [86] L.H. Brixner, *J. Inorg. Nucl. Chem.* 14 (1960) 225-230.
- [87] Y.-I. Kim, The Ohio State University, PhD Thesis, USA (2005).
- [88] D. Logvinovich, R. Aguiar, R. Robert, M. Trottmann, S.G. Ebbinghaus, A. Reller, and A. Weidenkaff, *J. Solid State Chem.* 180 (2007) 2649-2654.
- [89] K. Kamata, T. Nakamura, and T. Sata, *Chem. Lett.* 4 (1975) 81-86.
- [90] C. de la Calle, J.A. Alonso, M. Garcia-Hernandez, and V. Pomjakushin, *J. Solid State Chem.* 179 (2006) 1636-1641.
- [91] K. Kamata, T. Nakamura, and T. Sata, *Mater. Res. Bull.* 10 (1975) 373-378.
- [92] A. Weidenkaff, *Adv. Eng. Mater.* 6 (2004) 709-714.
- [93] C.N.R. Rao, *Materials Science and Engineering B* 18 (1993) 1-21.
- [94] L. Bocher, M.H. Aguirre, R. Robert, M. Trottmann, D. Logvinovich, P. Hug, and A. Weidenkaff, *Thermochim. Acta* 457 (2007) 11-19.
- [95] D. Logvinovich, A. Borger, M. Dobeli, S.G. Ebbinghaus, A. Reller, and A. Weidenkaff, *Prog. Solid State Chem.* 35 (2007) 281-290.
- [96] D. Logvinovich, M.H. Aguirre, J. Hejtmanek, R. Aguiar, S.G. Ebbinghaus, A. Reller, and A. Weidenkaff, submitted to *J. Solid State Chem.* (2008).
- [97] P. Fischer, G. Frey, M. Koch, M. Konnecke, V. Pomjakushin, J. Schefer, R. Thut, N. Schlumpf, R. Burge, and U. Greuter, *Physica B* 276-278 (2000) 146-147.
- [98] R.J. Hill and R.X. Fischer, *J. Appl. Crystallogr.* 23 (1990) 462-468.
- [99] E. Jansen, W. Schäfer, and G. Will, *J. Appl. Crystallogr.* 27 (1994) 492-496.
- [100] D.E. Cox and R.J. Papoular, *Mater. Sci. Forum* (1996) 228-231.
- [101] P. Thompson, D.E. Cox, and J.B. Hastings, *J. Appl. Crystallogr.* 20 (1987) 79-83.
- [102] J. Rodriguez-Carvajal, *Physica B* 192 (1993) 55-69.
- [103] P.A. Stadelmann, *Ultramicroscopy* 21 (1987) 131-145.
- [104] E.A. Davis and N.F. Mott, *Phil. Mag.* 22 (1970) 903.
- [105] I.P. Shapiro, *Opt. Spektrosk.* 4 (1958) 256.
- [106] T. Ressler, *Journal of Synchrotron Radiation* 5 (1998) 118-122.
- [107] P. Jeevanandam, Y. Koltypin, O. Palchik, and A. Gedanken, *J. Mater. Chem.* 11 (2001) 869-873.
- [108] K.S. Osamu Yamaguchi, Kiyoshi Shimizu, *Z. Anorg. Allg. Chem.* 514 (1984) 205-212.
- [109] L. Paama, I. Pitkanen, H. Halttunen, and P. Peramaki, *Thermochim. Acta* 403 (2003) 197-206.

- [110] F. Lichtenberg, A. Herrnberger, K. Wiedenmann, and J. Mannhart, *Prog. Solid State Chem.* 29 (2001) 1-70.
- [111] V. Vashook, L. Vasylechko, M. Knapp, H. Ullmann, and U. Guth, *J. Alloys Compd.* 354 (2003) 13-23.
- [112] C.J. Howard, B.J. Kennedy, and P.M. Woodward, *Acta Crystallogr., Sect. B* 59 (2003) 463-471.
- [113] W.R. Entley, C.R. Treadway, S.R. Wilson, and G.S. Girolami, *J. Am. Chem. Soc.* 119 (1997) 6251-6258.
- [114] J.A. Bearden and A.F. Burr, *Reviews of Modern Physics* 39 (1967) 125-142.
- [115] T. Ressler, O. Timpe, T. Neisius, J. Find, G. Mestl, M. Dieterle, and R. Schlogl, *J. Catal.* 191 (2000) 75-85.
- [116] F.W. Kutzler, C.R. Natoli, D.K. Misemer, S. Doniach, and K.O. Hodgson, *J. Chem. Phys.* 73 (1980) 3274-3288.
- [117] B. Ravel, Y.-I. Kim, P.M. Woodward, and C.M. Fang, *Phys. Rev. B: Condens. Matter* 73 (2006) 184121-7.
- [118] S.G. Ebbinghaus, A. Weidenkaff, and R.J. Cava, *J. Solid State Chem.* 167 (2002) 126-136.
- [119] S. Ebbinghaus, Z. Hu, and A. Reller, *Journal of Solid State Chemistry* 156 (2001) 194-202.
- [120] T. Maekawa, K. Kurosaki, H. Muta, M. Uno, and S. Yamanaka, *J. Alloys Compd.* 390 (2005) 314-317.
- [121] I. Nagai, N. Shirakawa, S.-i. Ikeda, R. Iwasaki, H. Nishimura, and M. Kosaka, *Appl. Phys. Lett.* 87 (2005) 024105.
- [122] S.I. Ikeda and N. Shirakawa, *Physica C* 341-348 (2000) 785-786.
- [123] N. Shirakawa and S.I. Ikeda, *Physica C* 364-365 (2001) 309-312.
- [124] F. Beuneu, P. Vajda, and O.J. Zogal, *Phys. Rev. Lett.* 83 (1999) 761-763.
- [125] D. Wallacher, R. Ackermann, P. Huber, M. Enderle, and K. Knorr, *Phys. Rev. B: Condens. Matter* 64 (2001) 184203.
- [126] R. Ackermann, T. Knoblauch, D. Kumar, K. Unger, and M. Enderle, *J. Low Temp. Phys.* 122 (2001) 143-146.
- [127] R. Ackermann and M. Enderle, *Eur. Phys. J. E* 12 (2003) 39-42.
- [128] R. Ackermann and M. Enderle, *Europhys. Lett.* 64 (2003) 260-266.
- [129] Z. Singh, S. Dash, R. Prasad, and D.D. Sood, *J. Alloys Compd.* 215 (1994) 303-307.
- [130] P. Subramanya Herle, M.S. Hegde, and G.N. Subbanna, *J. Mater. Chem.* 7 (1997) 2121-2125.
- [131] P. Ettmayer, *Monatshefte für Chemie / Chemical Monthly* 101 (1970) 127-140.
- [132] Y. Wang and R.C. Liebermann, *Phys. Chem. Miner.* 20 (1993) 147-158.
- [133] H. Nakano, M. Kobayashi, and N. Kamegashira, *J. Am. Ceram. Soc.* 90 (2007) 1276-1279.
- [134] A. Weidenkaff, M.H. Aguirre, T. Lippert, U. Falke, and U. Bangert, *Chimia* 60 (2006) 742-748.
- [135] M.H. Aguirre, R. Robert, D. Logvinovich, and A. Weidenkaff, *Inorg. Chem.* 46 (2007) 2744-2750.

- [136] C.L. Bull, P.F. McMillan, E. Soignard, and K. Leinenweber, *J. Solid State Chem.* 177 (2004) 1488-1492.
- [137] T. Kawashima, E. Takayama-Muromachi, and P.F. McMillan, *Physica C* 460-462 (2007) 651-652.

Acknowledgements

Herein I would like to acknowledge all the people who supported me during my PhD project.

First of all, I would like to thank Prof. Dr. Armin Reller, for agreeing to undertake the academic supervision of my work and for his help and support. Prof. Dr. Anke Weidenkaff for scientific supervision and productive discussions, which, I believe, improved my work and working discipline. I would also like to thank her for the truly great support to my work, patience to my personality and creating really nice working atmosphere in the Solid State Chemistry Group.

Prof. Dr. Stefan G. Ebbinghaus for discussing my scientific results and giving helpful advices to improve them and my scientific publications, for teaching Rietveld method and EXAFS data treatment and for assisting during the measurement campaigns at HRPT (SINQ). Dr. Denis Sheptyakov for improving my refinements, advising neutron experiments and publications input. Dr. Myriam Aguirre for TEM hardware and software training. Dr. Jiri Hejtmánek, Dr. Karel Knizek, Dr. Mirek Maryško and Dr. Alexander Börger for their scientific collaboration. Renato Figi for training hotgas-extraction. My bachelor student, Pedro Neves. My office mate and friend Rosa Robert for nice office atmosphere, patience and experimental assistance. Matthias Trottmann for many things, actually. As a colleague, for the realization of my ideas, *e.g.* for building ammonolysis reactors and sample holders and in general, for quick and efficient response which was always just in time. As a friend, for being always open and supportive, for organizing climbing events and for introducing me to Swiss climbing community. Dr. Paul Hug, for TGA experimental assistance. And all the present and the former Solid State Chemistry group members, Empa, Uni. Augsburg and PSI colleagues: Laura Bocher, Andrey Shkabko, Petr Tomeš, Sophie Wenger, Andreas Maccaignan, Claudia Schreiner, Rosiana Aguiar, Ivan Marozau, Dr. Heinz Vonmont, Dr. Peter Lienemann, Adrian Wichser, Dr. Andrea Ulrich, Dr. Gregor Müller, Dr. Davide Bleiner, Urs Gfeller, Dr. Marianne Senn, Karin Hanselmann, Renate Diessenbacher for nice inspiring atmosphere and help.

My parents, sister Tatsiana, my grandma and my muse Nadja (лапуся-Енот) for being always supportive and patient. Спасибо вам огромное за вашу поддержку, любовь и понимание. I can not express with words my gratitude for them.

Curriculum vitae

Name: Dmirty Logvinovich

Date of birth: 04.04.1982

Nationality: Belarus

09/1988-05/1993: Middle school N25, Brest, Belarus

09/1993-06/1999: Gymnasium N1, Brest, Belarus

09/1999-07/2004: Faculty of chemistry, Belarusian State University, Minsk, Belarus.

Diploma degree in chemistry. Specialization: Physical chemistry

10/2004-10/2008: Empa (Swiss Federal Laboratories of Materials Testing and Research).

University of Augsburg. PhD student